

DYNAMICALLY REFOCUSED
RAYLEIGH BEACONS FOR ADAPTIVE OPTICS

by

James Augustus Georges III

Copyright © James Augustus Georges III 2003

A Dissertation Submitted to the Faculty of the
COMMITTEE ON OPTICAL SCIENCES (GRADUATE)

In Partial Fulfillment of the Requirements
For the Degree of

DOCTOR OF PHILOSOPHY

In the Graduate College

THE UNIVERSITY OF ARIZONA

2003

UMI Number: 3119947

Copyright 2003 by
Georges, James Augustus, III

All rights reserved.

INFORMATION TO USERS

The quality of this reproduction is dependent upon the quality of the copy submitted. Broken or indistinct print, colored or poor quality illustrations and photographs, print bleed-through, substandard margins, and improper alignment can adversely affect reproduction.

In the unlikely event that the author did not send a complete manuscript and there are missing pages, these will be noted. Also, if unauthorized copyright material had to be removed, a note will indicate the deletion.

UMI[®]

UMI Microform 3119947

Copyright 2004 by ProQuest Information and Learning Company.

All rights reserved. This microform edition is protected against unauthorized copying under Title 17, United States Code.

ProQuest Information and Learning Company
300 North Zeeb Road
P.O. Box 1346
Ann Arbor, MI 48106-1346

THE UNIVERSITY OF ARIZONA ©
GRADUATE COLLEGE

As members of the Final Examination Committee, we certify that we have read the dissertation prepared by James Augustus Georges III entitled Dynamically Refocused Raleigh Beacons for Adaptive Optics

and recommend that it be accepted as fulfilling the dissertation requirement for the Degree of Doctor of Philosophy

J. Roger P. Angel
J. Roger P. Angel

12/19/03
Date

Michael Lloyd-Hart
Michael Lloyd-Hart

12/19/03
Date

James C. Wyant
James C. Wyant

19-Dec. 2003
Date

Date

Date

Final approval and acceptance of this dissertation is contingent upon the candidate's submission of the final copy of the dissertation to the Graduate College.

I hereby certify that I have read this dissertation prepared under my direction and recommend that it be accepted as fulfilling the dissertation requirement.

J. Roger P. Angel
Dissertation Director, J. Roger P. Angel

12/19/03
Date

STATEMENT BY AUTHOR

This dissertation has been submitted in partial fulfillment of the requirements for an advanced degree at The University of Arizona and is deposited in the University Library to be made available to borrowers under the rules of the Library.

Brief quotations from this dissertation are allowable without special permission, provided an accurate acknowledgement of source is made. Requests for permission for extended quotation from or reproduction of this manuscript in whole or in part may be granted by the copyright holder.

SIGNED :

A handwritten signature in black ink, appearing to be 'J. A. ...', written over a horizontal line.

ACKNOWLEDGEMENTS

I would like to acknowledge all of those who made this work possible.

My advisors. Roger Angel, without his vision, the pages of this and many other dissertations would be blank. Michael Lloyd-Hart, who as helped me through this work as well as my graduate process.

My colleagues. Without Tom Stalcup -- whose experience and knowledge helped with much more than just the “electronics” -- I may still be on Mt. Bigelow. Proteep Mallik, Christoph Baranec, Miguel Snyder, Kenneth Shirley and Matt Rademacher whose long and late hours are so very greatly appreciated.

My fellow Opt-Sci students. Ann, in more ways than I can write, I would have never made it without all of your help. Christian and Lenny, you got me past prelims. Also, Ann, Nick, J.D., Christian, Lenny, Sam, Chad, Tom, Proteep, Christoph, Brian, Brian, and Brian you all helped make this experience worth much more than a degree.

To all, sincerely and deeply, Thanks.

DEDICATION

This work is dedicated to those who have stood by me, supported me, taught me, let me walk my own path and let me come back home; my family. With love, respect and awe, I thank you.

TABLE OF CONTENTS

LIST OF FIGURES.....	9
ABSTRACT	11
CHAPTER 1 INTRODUCTION	12
1.1 NGS AO.....	14
1.1.1 ATMOSPHERE	15
1.1.2 OPTICAL PHASE.....	17
1.1.3 OPTIMAL SUBAPERTURE SIZE	20
1.1.4 SHACK HARTMANN WAVEFRONT SENSOR.....	21
1.1.5 BRIGHTNESS	23
1.1.5.1 TIME	23
1.1.5.2 SHOT NOISE	24
1.1.6 SKY COVERAGE.....	26
1.2 LGS AO.....	28
1.2.1 PROJECTION OPTICS	31
1.2.2 AUXILIARY BEAM PROJECTOR.....	33
1.2.3 IMAGE ELONGATION.....	34
1.2.4 FOCAL ANISOPLANATISM.....	37
1.2.5 SODIUM BEACONS.....	39
1.2.5.1 RETURN MECHANISM	39
1.2.5.2 ESTIMATED RETURN	40
1.2.6 RAYLEIGH BEACONS	42
1.2.6.1 RETURN MECHANISM	42
1.2.6.2 ESTIMATED RETURN.....	44
1.2.6.3 PHOTON RETURN AS A FUNCTION OF WAVELENGTH.....	47
1.2.7 DYNAMICALLY REFOCUSED RAYLEIGH BEACONS	49
1.3 LGS EFFORTS AND RESULTS.....	52
1.4 STATEMENT OF WORK	54
CHAPTER 2 MODELING OF DYNAMIC REFOCUS	55
2.1 INTRODUCTION.....	55
2.2 FIRST ORDER OPTICAL MODELS.....	56
2.2.1 SAGITTAL DEPTH AND Δ SAG.....	56
2.2.2 BLUR DUE TO A RISING LASER PULSE	61
2.2.2.1 A NOTE ABOUT BEAM TILT.....	65

TABLE OF CONTENTS - *Continued*

2.2.3 MODELING OF MMT DYNAMIC REFOCUS SYSTEM.....	66
2.2.4 PISTON MOTION OF THE CONCAVE MIRROR.....	73
2.2.5 IMAGE DUE TO DYNAMIC REFOCUS	78
2.3 OPTICAL MODEL ON THE 61”	80
2.3.1 EFFECT OF USING AN OFF-AXIS SUBAPERTURE	80
2.3.2 MODELING OFF-AXIS SUBAPERTURE	82
CHAPTER 3 MMT DYNAMIC REFOCUS SYSTEM.....	88
3.1 INTRODUCTION.....	88
3.2 MMT DYNAMIC REFOCUS OPTICS	89
3.2.1 MMT DR SYSTEM REQUIREMENTS.....	89
3.2.2 BASIC MODEL.....	90
3.2.2 FIELD LENS	92
3.2.3 OBJECTIVE	92
3.2.4 ABERRATIONS.....	94
3.2.5 MMT DR OPTICAL SYSTEM.....	94
3.2.6 FABRICATED SYSTEM	97
3.2.6.1 ALIGNMENT	99
3.2.6.2 TEST RESULTS	104
3.3 RESONATOR	105
3.3.1 DAMPED DRIVEN SIMPLE HARMONIC MOTION.....	105
3.3.2 MOTION OF AN ALUMINUM ROD	107
3.3.3 RESONATOR DRIVER	112
3.3.4 MMT DR RESONATOR AND DRIVER.....	113
CHAPTER 4 Mt. BIGELOW FIELD-TESTS.....	117
4.1 INTRODUCTION.....	117
4.2 SYSTEM ARCHITECTURE.....	118
4.3 61” TO MMT CONVERTER.....	120
4.3.1 DESIGN PHILOSOPHY.....	121
4.3.2 DESIGN AND EXPECTED RESULTS.....	125
4.3.3 CONVERTER BOX AND MMT DR SYSTEM ALIGNMENT.....	129
4.3.3.1 ALIGNMENT PHILOSOPHY.....	131
4.3.3.2 THE CAGE.....	132
4.3.3.3 ALIGNMENT PROCEDURE STEP 1: LASER AND MIRRORS	134
4.3.3.4 ALIGNMENT PROCEDURE STEP 2: MMT DR SYSTEM	139
4.3.3.5 PROCEDURE STEP 3:TILT OF FOLD MIRROR 4	142
4.3.3.6 ALIGNMENT PROCEDURE STEP 4: REMAINING REFRACTIVE ELEMENTS.....	143
4.3.3.7 ALIGNMENT PROCEDURE STEP 5: FINALIZING.....	147
4.3.4 CONTRIBUTION TO TOTAL ERROR	148
4.4 DEMAGNIFYING OPTICS AND GATED CAMERA, MMT TEST BED	151

TABLE OF CONTENTS - *Continued*

4.4.1 DESIGN PHILOSOPHY.....	153
4.4.2 DESIGN AND EXPECTED RESULTS.....	155
4.4.3 MMT TEST-BED ALIGNMENT.....	156
4.4.4 CONTRIBUTION TO TOTAL ERROR.....	160
4.5 BEAM PROJECTOR.....	160
4.5.1 DESIGN PHILOSOPHY.....	162
4.5.2 BEAM PROJECTOR DESIGN.....	164
4.5.3 BEAM PROJECTOR ALIGNMENT.....	166
4.5.3.1 IN THE LAB.....	167
4.5.3.2 ON THE MOUNTAIN.....	168
4.5.4 CONTRIBUTION TO TOTAL ERROR.....	172
4.6 CONTROL ELECTRONICS AND SOFTWARE.....	172
4.6.1 DESIGN PHILOSOPHY.....	173
4.6.2 DESIGN AND EXPECTED RESULTS.....	173
4.6.3 ALIGNMENT.....	178
4.6.4 CONTRIBUTION TO TOTAL ERROR.....	180
4.7 SUMMARY OF COMPONENT ERRORS.....	180
CHAPTER 5 RESULTS.....	182
5.1 EXPERIMENTAL OVERVIEW.....	182
5.2 DYNAMIC REFOCUS RESULTS.....	188
5.2.1 PLATE SCALE.....	188
5.2.2 DYNAMIC REFOCUS GUI.....	190
5.2.3 DYNAMIC REFOCUS RESULTS.....	192
5.2.3.1 RESULTS: 18 OCTOBER 2003, 4:27AM.....	193
5.2.3.2 RESULTS: 15 OCTOBER 2003, 2:46AM.....	198
5.2.3.3 RESULTS: 18 OCTOBER 2003, 4:13-4:30AM.....	198
5.3 ATMOSPHERIC MEASUREMENTS.....	203
5.3.1 TOTAL SEEING MEASURED BY BEACON IMAGE MOTION.....	203
5.3.2 DIFFERENTIAL MOTION.....	205
5.4 SUMMARY.....	209
REFERENCES.....	212

LIST OF FIGURES

Figure 1.1 The performance of a SHWFS with and without the atmosphere present.....	19
Figure 1.2 The blur due to the finite beacon over a range in the atmosphere.....	30
Figure 1.3 The sampling of the projected MMT pupil at different heights by multiple Rayleigh beacons.....	38
Table 1.1 Calculated photon return.....	45
Figure 1.4 The total transmission of the atmosphere as a function of wavelength and the photon return for a dynamically refocused Rayleigh beacon over the 20-30km range-gate as a function of wavelength.....	48
Figure 1.5 A black box definition of dynamic refocus.....	50
Table 1.2 A summary of LGS results.....	53
Figure 2.1 The change in sagittal depth of a pulse rising from height z_1 to z_2	58
Figure 2.2 The blur due to three discrete heights of a single rising pulse.....	63
Figure 2.3 Moving flat mirror.....	67
Figure 2.4 Moving curved mirror.....	70
Figure 2.5 The mathematical curve that is a result of equation (2.12).....	74
Figure 2.6 The mathematical curve of figure 2.5 fit to a sinusoid.....	76
Figure 2.7 Origin of the bowtie.....	81
Figure 2.8 An off-axis subaperture of the MMT geometry.....	84
Figure 2.9 Model output.....	87
Figure 3.1 The basic layout of the MMT DR optical system.....	91
Figure 3.2 The MMT DR optics are schematically shown.....	93
Figure 3.3 The Design of the MMT DR optical system and its prescription.....	95
Figure 3.4 The performance of the MMT DR optical system shown in figure 3.3 is shown above as a series of spot diagrams.....	98
Figure 3.5 Brian Ceurden's design for the stainless steel cell that supports the MMT DR objective optics.....	100
Figure 3.6 The layout for optically testing the MMT DR objective and cell and test results.....	102
Figure 3.7 The explanation of equations (3.7) and (3.17).....	109
Figure 3.8 Schematic of the ringer and driver.....	114
Figure 3.9 Test results of an earlier version of the MMT DR resonator/driver.....	116
Figure 4.1 The 61" DR experiment is schematically outlined.....	119
Figure 4.2 The full MMT cone of light is compared to the cone of light coming from an MMT 61" off-axis subaperture and the 61" to MMT converter box philosophy.....	122
Figure 4.3 A more complete schematic of the 61" to MMT converter box.....	124
Figure 4.4 The 61" to MMT converter optics are diagrammed.....	126
Figure 4.5 The geometry used for the 61"DR experiment of the five Rayleigh beacons.....	128
Figure 4.6 The configuration matrix produced by Zemax for the dynamically refocused images of the spots diagrammed in figure 4.5.....	130

LIST OF FIGURES - *Continued*

Figure 4.7 The steel cage that supports the 61" DR.....	133
Figure 4.8 The reflective surfaces in the converter optics, DR optics and alignment optics.	136
Figure 4.9 Field lens 1 and the magnifying lens placed of the converter optics placed in the system as well as the operation of the alignment optics.	144
Figure 4.10 The results of aligning the converter box on the 61" telescope..	150
Figure 4.11 The philosophy of the gated camera optical train is shown schematically ..	154
Figure 4.12 The receive optics for the 61" DR experiment are shown..	157
Figure 4.13 The ion events produced by the intensifier that are imaged on to the CCD by the transfer lens.	159
Figure 4.14 The result of imaging the IAL through the entire alignment optics, converter optics, DR optics and gated camera image train of the 61" DR experiment.....	161
Figure 4.15 The schematic design for the BP in the geometric limit.....	163
Figure 4.16 The 61" BP design is shown above with all of the optical components labeled.	165
Figure 4.17 The alignment of the Rayleigh beacons on the sky.....	171
Figure 4.18 The system architecture of the 61" experiment control electronics.	174
Figure 4.19 The prism epoxyed to the ringer that is used as a pick-up for the DMD..	176
Figure 4.20 Timing diagram of the control electronics.....	179
Table 4.1 The expected errors contributed by each component of the 61" DR experiment.	181
Figure 5.1 The 61" field test layout.....	183
Figure 5.2 The beam projector viewed on the sky.....	185
Figure 5.3 The five beacons viewed by the 61" experiment optics.	187
Figure 5.4 The image of a binary used to calibrate the experiment's plate scale.....	189
Figure 5.5 The LabVIEW GUI.	191
Figure 5.6 DR off and on results from 18 October 2003 at 4:27am.	194
Figure 5.7 Comparison of the model with 2.7arcsec FWHM blur and the 18 October 2003, 4:27am data..	195
Figure 5.8 Comparison of a long star exposure to the shorter exposure DR "on" case for 18 October 2003 at 4:27am.....	197
Figure 5.9 15 October 2003, 2:46am data.	199
Figure 5.10 15 October 2003, 2:46am data.	200
Figure 5.11 18 October 2003, 4:13-4:30am composite data.....	201
Figure 5.12 18 October 2003, 4:13-4:30am composite data.....	202
Figure 5.13 The North-South and East-West centroid data.....	206
Figure 5.14 Log-log plots of the North-South and East-West power spectra.....	208

ABSTRACT

Dynamic refocus, DR, for adaptive optics has been proposed as a process that, over a given range, will maintain a sharp image of the Rayleigh backscatter due to a laser pulse rising in the atmosphere. Sharp focus is important when the backscatter from an artificial star is used for wavefront sensing. The wavefront variance associated with a Shack Hartmann wavefront sensor is inversely related to the photon return (in the shot noise limited case) and is dependant on the square of the beacon image's angular size. For the same spot size the photon return of a dynamically refocused Rayleigh beacon is increased by a factor of twelve over a system without DR.

Here we present the implementation and results of the first operational Rayleigh beacon DR system. The DR system is designed for use on the MMT with five Rayleigh laser beacons projected on a 120arcsec regular pentagon. It was tested on the Mt. Bigelow 61" telescope, configured to act as an off-axis MMT subaperture. The results show the simultaneous DR of five Rayleigh beacons where a beacon image is dynamically refocused from 7arcsec FWHM to 2.7arcsecFWHM.

CHAPTER 1 INTRODUCTION

Adaptive optics, AO, is a maturing technology that greatly improves the imaging of an astronomical optical system by compensating for the phase aberrations created by a turbulent atmosphere. In order to compensate for these aberrations they must first be measured. The atmospheric probe for astronomical AO systems may be a bright, unresolved natural guide star, NGS. Absent of atmosphere, the wavefront due to the NGS arriving at the entrance aperture of an astronomical telescope is perfectly flat. In the presence turbulent atmosphere, the wavefront arriving at the telescope is randomly aberrated. This distorted wavefront is measured by dividing the entrance aperture of the telescope into subapertures and measuring the slope or curvature of the wavefront within each of these subapertures. The size of these subapertures is chosen relative to the statistical properties of atmospheric turbulence. In order to achieve a reasonable measurement, enough light must fall on each subaperture within an amount of time that the atmosphere may be considered frozen. These fundamental limitations drive the brightness requirement of the NGS.

A further requirement of the NGS is that it lies within close proximity to the scientific object to be imaged. Both the NGS probe of the atmosphere and the object of interest must fall within a measure called the isoplanatic angle. This is necessary so that the atmospheric measurement made by using the bright NGS probe is valid for both objects. The isoplanatic angle is also a result of the statistical nature of the turbulent atmosphere.

This proximity requirement is obviously a limiting case for astronomical applications; not every scientific object of interest has a bright, unresolved star nearby.

Based on the limitation of NGS's, the use of artificial probes are useful. Great benefit would be gained from a laser guide star, LGS, which could be placed relative to scientific objects of interest at the astronomer's discretion. The artificial star created by the laser beacon could be the result of molecular Rayleigh scattering that naturally occurs in the atmosphere [Fugate,1994]. This dissertation will encompass the benefit, philosophy, design, function, testing and results of the first operational Rayleigh beacon dynamic refocus system.

Dynamic refocus, DR, is a concept that increases the brightness of a Rayleigh LGS. This first chapter will serve to introduce the current state of astronomical AO with emphasis on LGS's. This chapter will compare and contrast current LGS efforts and follow a logical progression that will introduce dynamically refocused Rayleigh beacons as an immediate solution to the implementation of multi-conjugate adaptive optics, MCAO, on the MMT.

Chapter 2 will develop a paraxial model of a DR system for the full aperture of MMT as well as its smaller subapertures. This first order development will hint at design details of the actual MMT DR system that will be presented in Chapter 3. Chapter 4 describes

the system engineering for the field tests of MMT DR system on the Mt. Bigelow 61” telescope. Chapter 4 also describes the philosophy, design and alignment of the individual components used in the field tests. The results of the field tests are reported in Chapter 5.

1.1 NGS AO

The following section provides a brief overview of how the atmosphere is modeled in regards to AO, and how it may be measured. With knowledge of how the atmosphere is measured with a NGS, the brightness and proximity limits of such measurements are discussed. This is done specifically to understand the necessary requirements of a LGS AO system that uses a Shack Hartmann wavefront sensor.

This chapter will partly be concerned with the errors associated with AO measurements and correction and how they affect the resulting image. A commonly used metric for image quality is the Strehl ratio, SR, which is defined to be the ratio of the on axis irradiance of an AO corrected star to the on axis irradiance of the diffraction limited Airy disk. Small errors,

$$\sigma^2 < 1 \text{rad}^2 \quad (1.1)$$

in the wavefront may be used to approximate a the Strehl ratio by

$$SR = e^{-\sigma^2} \quad (1.2)$$

This approximation describes the relationship between wavefront error and image quality. The 1rad^2 metric is used to give a feel of the errors throughout the dissertation.

1.1.1 ATMOSPHERE

AO systems currently model the atmosphere as layers of phase screens. The turbulent mixing of the atmospheric content and density due to temperature and pressure fluctuations all affect the optical thickness, or equally, the index of refraction within a local region of the atmosphere. For the purpose of this dissertation, it will be assumed that the index variations of the atmosphere are independent of wavelength, i.e. that atmosphere exhibits no dispersion. The atmospheric index fluctuations are proportional to the atmospheric temperature fluctuations that are statistically described by the Kolmogorov-Obukhov turbulence model [Tatarski, 1961]. This model statistically describes the atmosphere by a structure function that displays a $5/3^{\text{rds}}$ power law dependence. A result of this atmospheric model is the error associated with averaging over an area of the wavefront [Fried, 1965 and Noll, 1976]

$$\sigma_1^2 = 1.03 \left(\frac{D}{r_o} \right)^{5/3} \quad (1.3)$$

where D is the diameter of the averaged circular area. The parameter r_o is operationally defined as the diameter of the area of an atmospherically aberrated wavefront over which the RMS phase difference is 1rad^2 .

From the Kolmogorov-Obukhov turbulence model, the measure r_o is found to display a $\lambda^{6/5}$ dependence [Fried, 1966]. If r_o is measured at a wavelength λ_o then the appropriate r_o for wavelength λ is

$$r_o(\lambda) = r_o(\lambda_o) \left(\frac{\lambda}{\lambda_o} \right)^{6/5} . \quad (1.4)$$

The parameter r_o is also referred to as the coherence length of the atmosphere. This length has an impact over the field of view, FOV, which may be corrected by AO. This field is referred to as the isoplanatic angle and is approximately [Fried, 1982],

$$\theta_o = \frac{r_o}{h} \quad (1.5)$$

where h is the height of the atmospheric turbulence, phase screen. The error associated with making an AO corrected image some angular distance θ from the NGS is given as [Fried, 1982 and Sandler et al., 1994]

$$\sigma_{iso}^2 = \left(\frac{\theta}{\theta_0} \right)^{5/3}. \quad (1.6)$$

Thus, the error associated with making an AO image at angle θ is 1 rad^2 .

1.1.2 OPTICAL PHASE

Optical phase is acquired as the wavefront, which may be viewed as a disk the size of the telescope's primary, travels downward through the atmosphere (figure 1.1). Prior to entering the atmosphere, the disk is perfectly flat. After entering the atmosphere, the disk passes through turbulence layers that contain atmospheric cells of different refractive index, Δn_i , and depth, d_i . The change in optical phase acquired by the wavefront after passing through the i^{th} cell is

$$\Delta\phi(x, y)_i = \frac{2\pi}{\lambda} \Delta n(x, y)_i d(x, y)_i \quad (1.7)$$

where λ is the wavelength of the light. The portions of the wavefront that pass through cells of high optical thickness are retarded more than those areas that pass through cells of lower optical thickness.

The change in phase that the wavefront acquires from each cell from each atmospheric layer is added in order to find the total change in phase of the wavefront falling on the telescope

$$\Delta\phi(x, y)_{total} = \sum_i \frac{2\pi}{\lambda} \Delta n(x, y)_i d(x, y)_i \quad (1.8)$$

It is assumed that $\Delta\phi(x, y)_{total}$ of the wavefront may be modeled as a single phase-screen conjugate to the primary (or secondary) mirror location. The wavefront incident on the telescope is distorted, with areas of the wavefront that have acquired less optical phase (less optical thickness) arriving before the areas that have acquired more phase (more optical thickness). This single, incident, total phase-screen may be reimaged to any other telescope pupil plane.

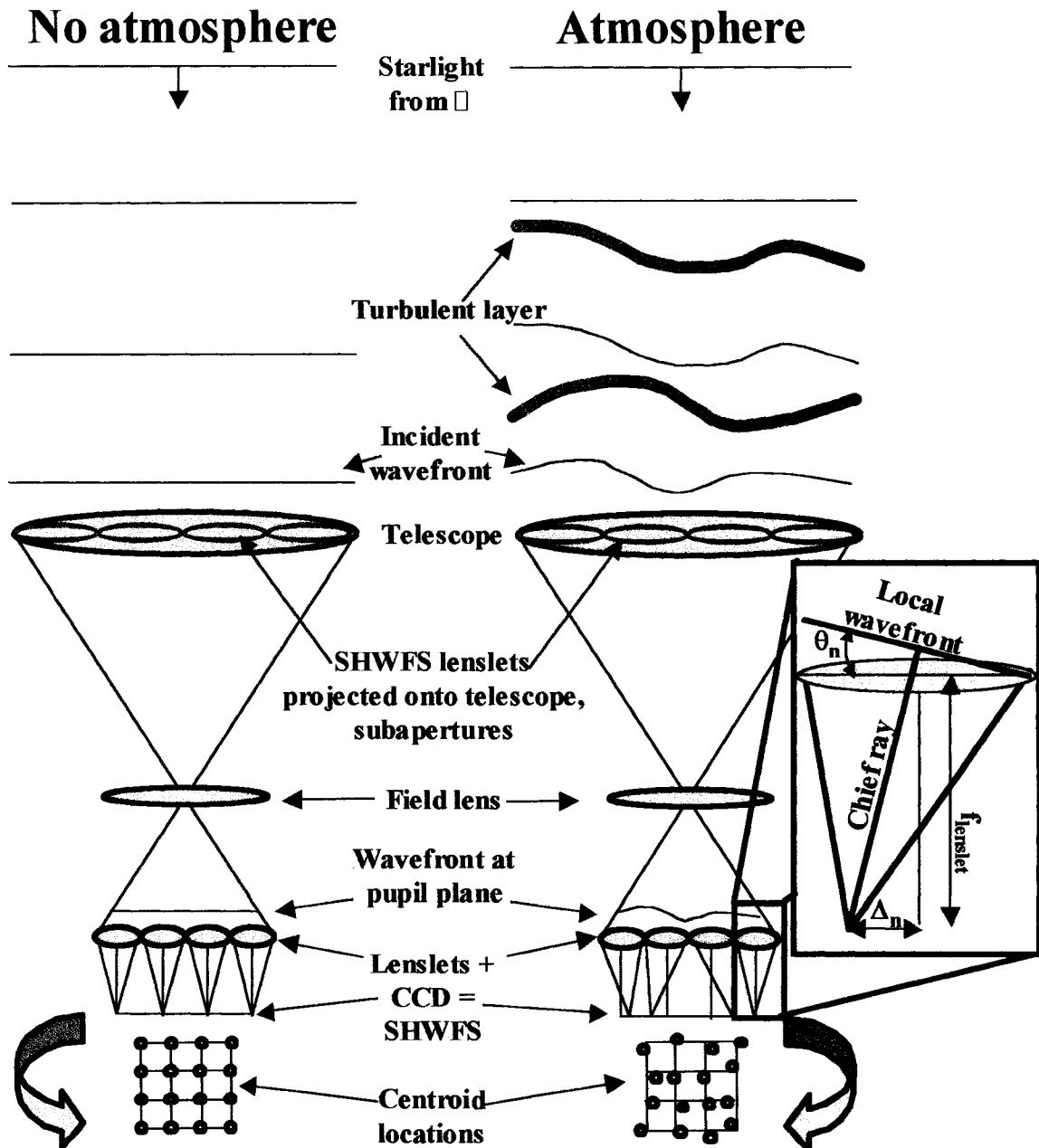


Figure 1.1 The performance of a SHWFS with and without the atmosphere present. The projection of the SHWFS lenslets onto the telescope primary breaks it up into subapertures. The grayed inset schematically shows how each a locally sloped wavefront causes the displacement of an image centroid when imaged through a lenslet.

1.1.3 OPTIMAL SUBAPERTURE SIZE

Given the statistical measure r_0 that results from assuming the Kolmogorov-Obukhov turbulence model and the total wavefront at the telescope, $\Delta\phi(x,y)_{total}$, one now seeks to determine the optimal size of a telescope or more significantly, of a subaperture to measure the wavefront. Noll [1976] presented the mean square residual wavefront error resulting from the perfect correction of the first j Zernike terms. The Zernike polynomials are functions that are orthogonal over the unit circle and are commonly used to model wavefront error at a circular aperture. The low order Zernike polynomials relate in a straightforward manner to the commonly discussed third order aberrations. If piston, tip and tilt are removed from the area that resulted in equation (1.3), the residual mean square error is given as

$$\sigma_3^2 = 0.134(D/r_0)^{5/3} \quad (1.9)$$

where D is the diameter of the (telescope or) subaperture and the subscript 3 is for consistency with the nomenclature of the reference. If one assumes a maximum residual error of 1rad^2 , then a guideline would be

$$D_{sub} = 3.33r_0. \quad (1.10)$$

It is important to note that the size of this subaperture was determined by the ability to correct piston, tip and tilt of an aberrated wavefront. The following section deals with the measurement of the wavefront.

1.1.4 SHACK HARTMANN WAVEFRONT SENSOR

A Shack Hartmann wavefront, SHWFS, is the combination of an array of lenslets and (usually) a CCD detector that operates in a pupil plane of a telescope (figure 1.1). The lenslets' size is related to the parameter r_0 and the result of equation (1.10). Because r_0 is a statistical measure, it may vary from night to night, even moment to moment. So more appropriately, the lenslets' size is determined by the nominal r_0 of a specific telescope site along with engineering issues related to the AO system installed on that telescope.

The SHWFS is located at a pupil of the telescope system. The projected image of the lenslets onto the telescope's primary (or secondary) mirror breaks that mirror up into subapertures. Each individual lenslet contributes a measurement of the wavefront over its corresponding subaperture.

In the absence of turbulence, the lenslets would each form an image of the star on their individual optical axis. In the presence of turbulence, the incident wavefront displays

some local slope, θ_n , in the n^{th} subaperture. The local, n^{th} chief ray passes through the n^{th} lenslet forming an image

$$\Delta_x = f_{\text{lenslet}} \theta_n \quad (1.11)$$

from the lenslets' optical axis. Equation (1.11) demonstrates how the image displacement, Δ_n , is actually a measure of the slope of the wavefront over the n^{th} subaperture. The local slope of the wavefront is related to the local change in phase in the x-direction of the wavefront through,

$$\Delta\phi(x)_n = \theta(x)_n \frac{2\pi d_{\text{lenslet}}}{\lambda} \quad (1.12)$$

where d_{lenslet} is the diameter of the lenslet projected on the primary. Using equation (1.11), equation (1.12) may be reduced to

$$\Delta\phi(x)_n = \Delta_{x,n} \frac{d_{\text{lenslet}}}{f_{\text{lenslet}}} \frac{2\pi}{\lambda} \quad (1.13)$$

where $\Delta_{x,n}$ is the centroid displacement in the x-direction relative to the n^{th} lenslet's optical axis. A similar process may be followed to find the phase in the y-direction of the incident wavefront.

1.1.5 BRIGHTNESS

The nature of dividing the full aperture by means of the lenslet array is a contributing factor to the brightness limitation placed on a NGS. The other factors that must be considered are the time in which the atmosphere may be considered frozen and the quantum nature of light.

1.1.5.1 TIME

The time in which the atmosphere may be considered frozen, Δt , is a parameter that is derived from the Kolmogorov-Obukhov turbulence model and may be described as [Sandler et al., 1994]

$$\Delta t < t_o = \frac{r_o}{< v_w >} \quad (1.14)$$

where $< v_w >$ is an averaged, turbulent weighted wind speed. The value t_o is operationally defined to be the time delay, from atmospheric measurement to AO correction that will

produce a 1rad^2 RMS phase error. The phase error is a result of the atmospheric phase layers moving across the telescope aperture in the time between measurement and correction.

Assuming values for the MMT of $r_o(2.2\mu\text{m})=79\text{cm}$ and $\langle v_w \rangle = 8\text{m/s}$, the result is $t_o=100\text{ms}$. Under these conditions the AO system should at the very least operate at 10Hz. The MMT AO system is designed to operate at 550Hz, further reducing the error due to time delay. This takes into account Nyquist sampling and servo theory as well as engineering issues related to delay from measurement to correction and actuator response time. What can be gleaned from this is the necessity for data collection to occur on the order of milliseconds. Therefore, the integration time for the wavefront sensor, WFS, must also be on the order of a millisecond.

1.1.5.2 SHOT NOISE

The quantum nature of light, specifically the shot noise associated with a high photon arrival rate is what may limit the ability of the SHWFS to determine the spot location and thus the wavefront slopes associated with each subaperture. If the signal arriving at a detector is N photons, the associated shot noise is proportional to $N^{1/2}$, giving a SNR of $N^{1/2}$. Hardy [1998] develops the standard deviation associated with the angular position (θ_x , from section 1.1.4) error when using a bi-cell detector in the one dimensional, shot noise limited case (neglecting read noise and background photons),

$$\sigma_{AngPos} = \frac{3\pi \lambda}{16 d \sqrt{N}} \quad (1.15)$$

where d is the diameter of the SHWFS subaperture.. Equation (1.15), which is a measure of the error in measuring the wavefront's local slope, is in close agreement to the results of other references [Tyler and Fried, 1982, Gardner et al., 1990 & Sandler et al. 1994]. To be consistent with the previous errors, it is desirable to relate the result of equation (1.11) to an RMS error of the wavefront. To accomplish this, the equation is multiplied by the proportionality factor of $2\pi d/\lambda$. This result is equivalent to integrating over the wavefront slopes in two-dimensions to give an error in phase,

$$\sigma_{SHWFS}^2 = \alpha \left(\frac{3\pi^2}{8} \right)^2 \frac{1}{N} \quad (1.16)$$

where α is a factor that may be varied based on observed conditions. Each of the above references estimates their own value of α . Assuming $\alpha=1$, in order to keep this error under the 1rad^2 RMS limit imposed in prior sections at least 14 photons must be collected per subaperture.

The NGS magnitude required for a SHWFS will be calculated using the information derived thus far. It will be assumed that the SHWFS will view a visible band star. For the case of $r_o(2.2\mu\text{m})=79\text{cm}$ yields an $r_o(550\text{nm})=15\text{cm}$. From equation (1.10), this allows for a subaperture diameter of 50cm. As a comparison, the MMT subapertures are 54.2cm on a side, the round number, 50, will be used in subsequent calculations.

The 1ms, 14photons and 50cm (assumed square subaperture) results found above yield a photon flux density of $56,000[\text{photons}/(\text{s m}^2)]$, which corresponds to an approximate magnitude of a V-band NGS of $m_v \sim 13$. This is magnitude assumes no losses. This limiting magnitude will limit the amount of the sky that may be probed with NGS AO. The limiting photon flux density must also hold for LGS's and immediately defines a necessary design performance for any such laser beacon.

1.1.6 SKY COVERAGE

The NGS brightness requirement was derived in the last section to be $m_v=13$. The drawback resulting from this calculation is that not every object of scientific interest will lie within the isoplanatic angle of such a star. The number of stars brighter than $m_v=13$ may be approximated by [Miller and Friedman, 1996]

$$\#S = 11.8 * 10^{(0.4204 m_v)} \quad (1.17)$$

yielding $\#S=3.4*10^6$.

The isoplanatic angle for an $r_o(2.2\mu\text{m})=79\text{cm}$ and an assumed turbulence height of 10km subtends a solid angle $\omega_o=6.2*10^{-9}\text{sr}$. (Note: this calculation was done for the solid angle of the science wavelength.) Now making the very broad assumptions that no $m_v=13$ or brighter stars lie within the same ω_o and that the sky is randomly and evenly distributed with such stars, the sky coverage, SC, is a result of

$$SC = \frac{\#S_{m_{13}} \omega_o}{4\pi} \quad (1.18)$$

yielding a probability of finding a brighter than $m_v=13$ star near the science object of interest of $SC\sim 0.17\%$. Even given the assumptions made above, this value (to the surprise of the author) agrees with those presented by other references [Hardy, 1998].

The above discussion has given the probability of finding a NGS within the isoplanatic patch of the science object. The discussion next leads to the impact of LGS's on sky coverage, a topic that is dealt with in the references [Sandler et al. 1994, Hardy, 1998 and Roddier 1999]. LGS's will sample high order atmospheric variations but not tip/tilt

because of the common path traveled by the up and down laser beam. As a result, a NGS is still required to sense these low order modes. Accordingly, its brightness requirement is lessened and the probability of finding a suitable NGS within the isoplanatic patch is increased. Furthermore, Sandler et al. [1994] state that because only low order correction required, the NGS may be a sharpened infrared source. Because of the larger population of infrared sources, the probability of finding a tip/tilt NGS to compliment the high order detection of the LGS is increased. The resulting LGS AO sky coverage quoted is dependant on the model, the relation to the galactic plane and the wavelength band of the quad cell detector. Regardless, orders of magnitude increase in probability is reported. This dramatic increase is the driving force to develop LGS's in general.

1.2 LGS AO

With the brightness requirement derived in section 1.1.5, attention is now turned to the character of the LGS itself. By definition, the LGS's are projected from a low altitude figure 1.2. There will be issues related to the projection of a laser beacon that produces a seeing limited guide star at some finite height in the atmosphere. Because of the finite height of this return illumination, the laser light is limited to how much of the atmosphere it may investigate. This is illustrated as the dashed cones compared to the thin solid cylinder of the left image of figure 1.2.

In order view the LGS, some mechanism must cause a portion of the laser light to be projected in the opposite direction of beacon propagation toward the telescope. The mechanism that causes this return illumination will not be instantaneously abrupt, so the

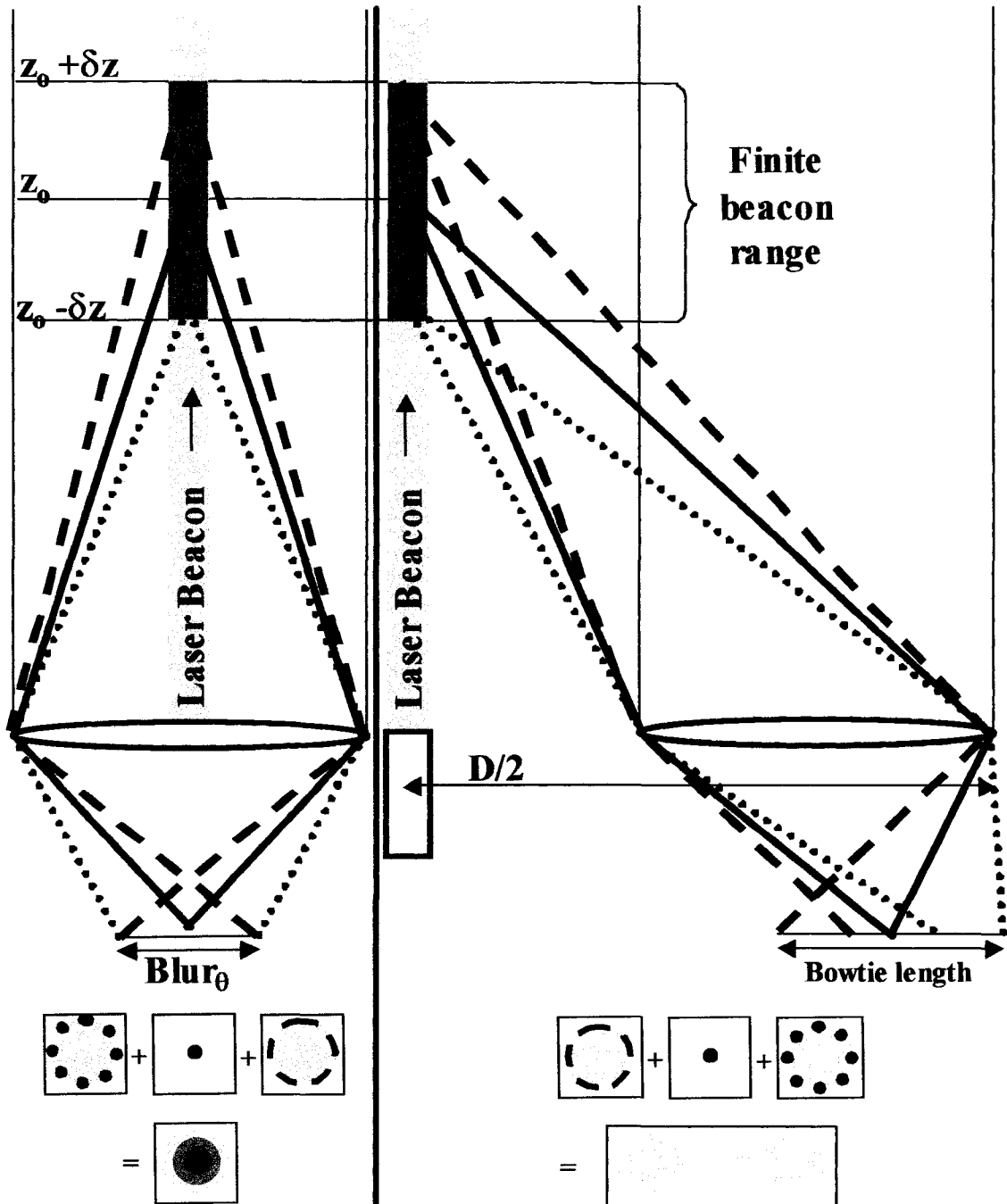


Figure 1.2 The blur due to the finite beacon over a range in the atmosphere is shown. For the case on the left, where the beacon is directly above the telescope, a circular symmetric blur is created. For the case on the right, the beacon is projected next to the telescope and a bowtie image is formed. The right hand case approximates a subaperture.

(somewhat) continuous nature of return over a finite beacon range must also be investigated.

The considerations outlined above will be discussed in general in sections 1.2.1-1.2.4. Specific types of return mechanisms, the resonant fluorescence of mesospheric sodium and Rayleigh scattering will be discussed in sections 1.2.5 and 1.2.6 respectively. The discussion of Rayleigh beacons will lead to the idea of dynamic refocus and multiple LGS's for MCAO, section 1.2.8. A summary of current LGS projects will then be presented in section 1.3.

1.2.1 PROJECTION OPTICS

To form a LGS, a laser must be projected into the atmosphere. The mechanisms that return light to the telescope will be discussed in sections 1.2.5.1 and 1.2.6.1. For now, it will be sufficient to realize that it is necessary to place a seeing limited laser spot somewhere in the atmosphere in order for a seeing limited spot to be detected. For resonant sodium, this spot must be placed at the mesospheric sodium layer, approximately 90km. For Rayleigh scatter, the spot may be placed anywhere with significant atmospheric density to allow for Rayleigh return, but, unless otherwise stated, this dissertation will be concerned with the range of 20-30km. The significance of this range will be outlined in section 1.2.7.

The propagation of a laser is readily described by Gaussian beams [Siegman, 1986]. A diffraction limited Gaussian beam operates in the TEM₀₀ mode and has an M² parameter of unity. An M² parameter greater than unity describes how many times diffraction limited a laser is. The literature suggests different definitions for M² as it relates to how many times diffraction limited, TDL, a laser beam is [Bollanti, 1997]. For this dissertation, the term TDL will be used to avoid discrepancies. For example, if a diffraction limited laser was used in a projection system to form a spot with a diameter=d₀, then a laser with an TDL parameter greater than unity projected through the same optics would form a spot with an approximate diameter of.

$$d_o' = TDL \cdot d_o \quad (1.19)$$

A focused Gaussian beam has a spot size of [Seigman, 1986]

$$d_o \approx \frac{2f\lambda}{D} \quad (1.20)$$

where D is the diameter of the focusing element and f is the distance to the focused spot of 1/e diameter d₀. Equation (1.20) may also be written as d₀~2λf/#.

If d_0 was restricted to subtend an angular size of 1 arcsecond ($5\mu\text{rad}$), then equations (1.19) and (1.20) could be combined to give the required optical element diameter

$$D = \frac{2TDL \cdot \lambda}{5 \cdot 10^{-6}} \quad (1.21)$$

Assuming visible wavelengths ($\lambda \approx 500\text{nm}$) equation (1.17) reduces to

$$D(\text{cm}) = 20 \cdot TDL \quad (1.22)$$

where D is given in centimeters. For example, a laser with $TDL=1.2$ would require a 24cm or approximately 10inch projection optic to produce a 1 arcsec laser beacon. The assumptions built into equation (1.20) are outlined in the reference.

1.2.2 AUXILIARY BEAM PROJECTOR

Based on equations (1.21) and (1.22) the quality of a laser, its TDL value, will dictate the size of the projection optics required to produce a seeing limited, ~ 1 arcsec, beam somewhere in the atmosphere. It is obvious that a poor quality laser with a large TDL value requires large projection optics. LGS programs that rely on lasers with high TDL

values solve this problem by projecting the laser beacon through the science telescope aperture [Fugate et al., 1982, Thompson & Castle, 1992, Thompson & Teare, 2002 and Clark et al., 2003]. This concept of full aperture sharing has problems associated with switching between the LGS and science light as well as fluorescence in the telescope and its optics (please refer to above references).

To alleviate the problems with full aperture sharing, it is desirable to project the beacon from an auxiliary beam projector. To reduce costs, it is further desirable for this projector to be small, which requires a well-corrected laser with a low TDL value.

1.2.3 IMAGE ELONGATION

Figure 1.2 shows the geometry of a projected laser beacon viewed directly below or from the side. The beacon is assumed to be from a laser with good beam quality and is projected from an auxiliary telescope. For the case that the telescope is directly below the beacon with a fixed image plane conjugate to a height z_0 , a laser beacon considered over a range $\pm\delta z$ about z_0 will produce an angular blur,

$$Blur_{\theta} = D\left(\frac{1}{z_0} - \frac{1}{z_0 + \delta z}\right). \quad (1.23)$$

where D is the diameter of the imaging telescope (refer to section 2.2.2 for a more in depth discussion). For the case of the telescope viewing the laser beacon from the side, the above equation will describe the length of the bowtie image formed if $D/2$ is the distance from the edge of the telescope aperture to the center of beam projector. The side-viewing case describes what a telescope subaperture would see. For example, the 6.5 MMT telescope viewing a 20-30km beacon ($z_0 = 25\text{km}$, $\delta z = \pm 5\text{km}$) results in angular $\text{Blur}_\theta = 13.4\text{arcsecs}$.

As an extension of geometry, future 30m telescope with sodium beacons scale almost four times larger than the MMT with Rayleigh beacons. Equation (1.23) may be approximated as

$$\text{Blur}_\theta = D \frac{\delta z}{z_0^2} \quad (1.24)$$

where z_0 is the average height of the beacon. It is seen that if the beacon range, δz stays the same, approximately 10km in both cases, then the blur is reduced approximately by the scaling factor between the MMT and a 30m telescope, resulting in a still significant $\text{Blur}_\theta = 3.6\text{arcsecs}$.

The significance of the size of the angular beacon blur is understood by further examination of the Section 1.1.5.2 results. This section discussed the photon return required for a SHWFS. A NGS, by definition is always seeing limited, however in accordance to equation (1.23) a LGS may be form a much larger than seeing limited image. This large image also has an effect on the ability of a SHWFS to measure a centroid position. Hardy [1998] gives an extension of equation (1.16), (where it is again assumed to be shot noise limited),

$$\sigma_{SHWFS}^2 = \left(\frac{K_g \pi^2}{4} \right)^2 \left(\left(\frac{3}{2} \right)^2 + \left(\frac{d\theta}{\lambda} \right)^2 \right) \frac{1}{N} \quad r_o > d \quad (1.25a)$$

$$\sigma_{SHWFS}^2 = \left(\frac{K_g \pi^2}{4} \right)^2 \left(\left(\frac{3d}{2r_o} \right)^2 + \left(\frac{d\theta}{\lambda} \right)^2 \right) \frac{1}{N} \quad r_o < d \quad (1.25b)$$

where θ is the angular extent of the reference beacon ($\theta \gg \lambda/d$) and K_g is an error term.

What is immediately noticed is that in both equations, the wavefront variance depends quadratically on the beacon size. This fact highlights the necessity to keep the beacon image as small as possible.

1.2.4 FOCAL ANISOPLANATISM

Because of the finite height of a LGS, it does not fully sample the cylinder of atmosphere that the starlight passes through (figure 1.2). This effect is referred to as the cone effect or focal anisoplanatism. Intuitively, the higher the LGS the lower the cone effect, a fact that has endeared many to sodium LGS's. An expression for focal anisoplanatism is given as [Fried, 1992 & Sandler et al., 1994]

$$\sigma_{cone}^2 = \left(\frac{D}{d_o} \right)^{5/3} \quad (1.22)$$

where d_o (which is not the same parameter used in 1.19 and 1.20) may be operationally defined as the effective diameter of a telescope that will produce a 1rad^2 error due to focal anisoplanatism. The parameter d_o is related to the science wavelength through a $\lambda^{6/5}$ dependence. Typical values for d_o are given by Sandler [1994 & 1999] for infrared ($2.2\mu\text{m}$, science) light as approximately 5m for Rayleigh beacons and approximately 20m for higher sodium LGS's. Using these values, the 6.5m MMT in the Rayleigh case displays an error of approximately 1.5rad^2 .

Lloyd-Hart [et. Al, 2001&2003] consider using multiple beacons to mitigate this effect (figure 1.3). The figure models the MMT with LGS's on a normal pentagon with a 120arcsec

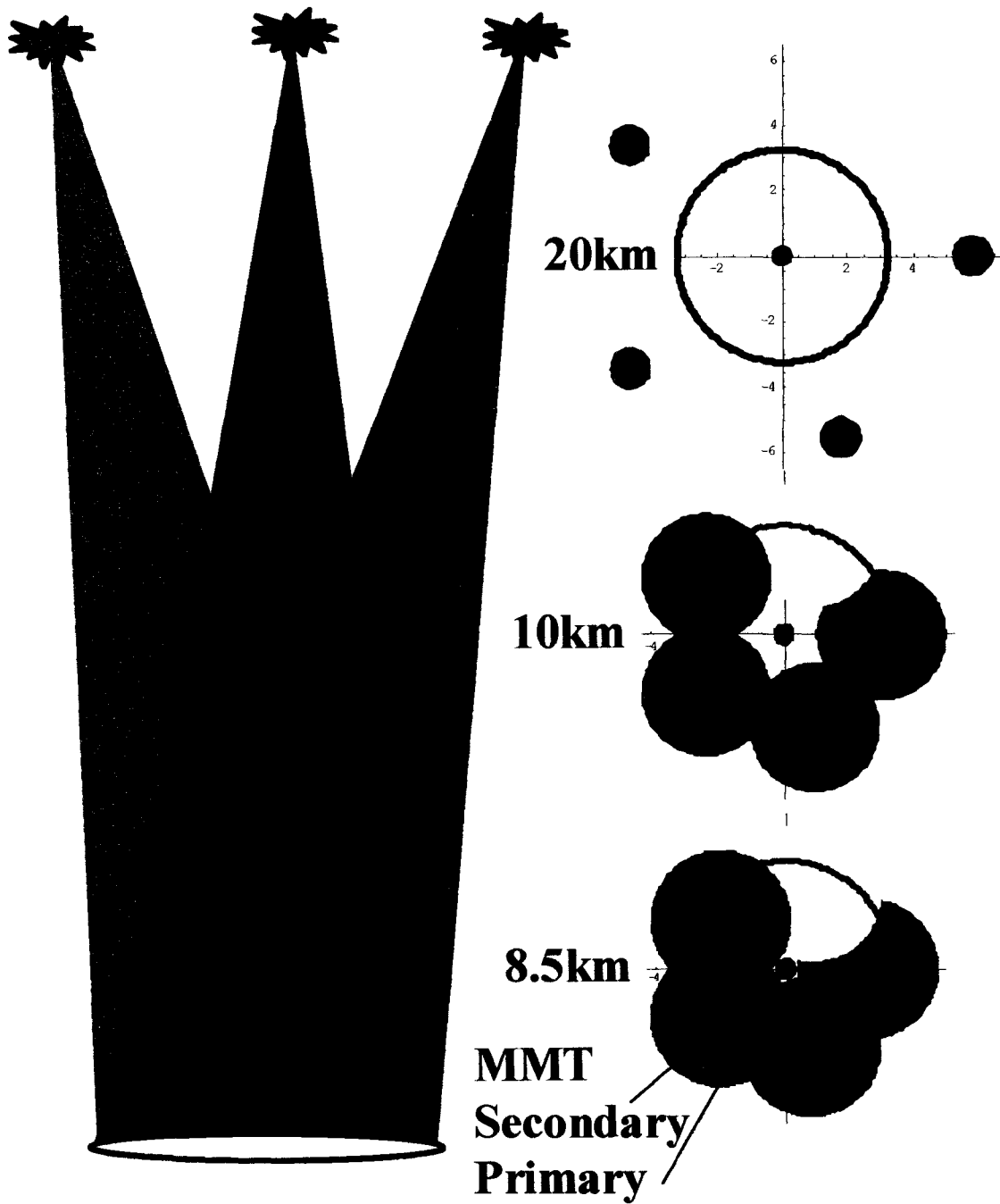


Figure 1.3 The sampling of the projected MMT pupil at different heights by multiple Rayleigh beacons. The beacons are modeled to lie on a regular pentagon inscribed on a 120arcsec diameter circle. The beacons are modeled at 25km.

diameter at 25km. The right side of the figure illustrates the increased sampling of the projected MMT pupil. The basic conclusion is that multiple beacons sample more of the atmosphere than a single beacon. This increased sampling mitigates the cone effect.

Section 1.2.7 will state references that describe a method for reducing the error due to focal anisoplanatism by utilizing geometry similar to that shown. To foreshadow, an analogy may be made between the information acquired from the multiple beacons to the information acquired from multiple images taken with a CAT scan. Both use multiple two dimensional views of the object of interest, the atmosphere in the former and a person in the latter, to create a three dimensional map of their respective subjects. This three dimensional map of the atmosphere allows for the idea of correcting at multiple conjugates in the atmosphere instead of assuming it is only present at the ground layer.

1.2.5 SODIUM BEACONS

It is beyond the scope of this dissertation to give a full discussion of sodium LGS's.

Therefore, the following sections will give only a very general description.

1.2.5.1 RETURN MECHANISM

Sodium LGS's take advantage of sodium resonant fluorescence that occurs at a mesospheric layer of approximate height of 90-100km. The density of this layer is

variable causing the photon return to be variable. The scattering mechanism may be thought of, but is actually much more complicated than, a two level system. The incident laser beacon is matched to the sodium absorption line. An incident beacon photon may be absorbed by a sodium atom exciting it to a higher level. In its higher level the atom may spontaneously decay, contributing to backscatter or another incident photon may cause spontaneous emission that does not contribute to the backscatter [Hardy, 1998].

1.2.5.2 ESTIMATED RETURN

Happer et al. [1994] and included references develop detailed theory concerning sodium beacons. One of his conclusions estimates that at least 4% of a properly tuned probe laser will be scattered. Sandler [1999] gives an argument based on a saturation irradiance, $I_{\text{sat}} = 1.9 \text{ W/cm}^2$, deriving a metric describing the sodium return per watt of CW laser to be

$$F_{CW} = 10^6 \frac{\text{photons}}{\text{s} \cdot \text{m}^2 \cdot [\text{W}]} \quad (1.27)$$

(The reference does not include the /W, which I believe is a typo). Equation (1.27) is stated to be linear and valid to the limit I_{sat} .

In order to convert this value of return, F , (in the units given above) into a value equivalent to visible band star brightness, m_v , it is placed into

$$m_v = -2.5 * \log\left(\frac{FW}{8.3 * 10^9}\right) \quad (1.24)$$

where W is the CW laser power in units of watts. The value $8.3 * 10^9$ comes from a zero magnitude star, $m_0 = 10^{11}$ [Photons/(m^2 s μm)] [Hynes, 2003] times a bandwidth of $0.083 \mu m$ in the visual band.

Following Sandler [1999] a 1arcsec, 45cm, spot at 90km will have a saturation laser power of 4kW, this will give the equivalent of $m_{v \text{ sat}} = 9.8$.

The sodium method of producing LGS's for AO holds significant promise.

Unfortunately, since the suggestion by the JASON group to use mesospheric sodium beacons in 1982 [Happer, 1994] very few AO groups have reported results, see table 1.2.

This fact is directly related to the complexity and cost of sodium systems.

This highlights the need for cheap reliable lasers of good quality to be used as LGS's in the present to investigate their impact on AO systems. AO sky surveys are used to

support the need for future large telescopes. Such surveys require AO correction over a large field of view, requiring multiple beacons (again foreshadowing to the references in section 1.2.7). For this case, as stated in section 1.2.3, Rayleigh beacons on the MMT approximately scale to sodium beacons on 30m telescopes, allowing lessons to be learned now while sodium LGS continue to develop.

1.2.6 RAYLEIGH BEACONS

The current complexity and cost associated with sodium beacons may be contrasted with Rayleigh beacons that may be produced with low cost, high quality, commercially available lasers.

1.2.6.1 RETURN MECHANISM

Unlike the single layer resonant fluorescence of sodium, the return mechanism for Rayleigh beacons is a continuous function within the atmosphere. Rayleigh beacons, although more efficient at shorter wavelengths, are not required to match a specific absorption line as are sodium beacons. As the name suggests, Rayleigh LGS's depend on the same mechanism that makes the sky blue in the daytime and red at sunset, Rayleigh scattering. This type of scattering is well understood and described by the Lidar equation [Hardy,1998],

$$N(z_o) = \left(\frac{E\lambda}{hc} \right) (\sigma_B n(z_o) \Delta z) \left(\frac{A_R}{4\pi z^2} \right) (T_o T_A^2 \eta) + N_B \quad (1.29)$$

where,

- $N(z_o)$ is the expected number of photons returned from a range Δz centered around z_o .
- E is the laser pulse energy, J
- λ is the beacon wavelength, m
- h is Plank's constant, $6.626 \cdot 10^{-34}$ J•s
- c is the speed of light, $3 \cdot 10^8$ m/s
- σ_B is the effective backscatter cross-section, m^2
- $n(z_o)$ is the number density of scatterers at a height z_o , m^{-3}
- Δz is the effective range of the beacon, the range gate, m
- A_R is the receive telescopes aperture area, m^2
- z_o is the height to the center of the range gate, m
- T_o is the transmission coefficient of the optics in both the send and receive paths, unit less.
- T_A is the one way transmission coefficient of the atmosphere between the beacon and the telescope, unit less and a function of wavelength

- η is the quantum efficiency of the photon detector, unit less and a function of wavelength
- N_B is the number of background and noise photoelectrons

1.2.6.2 ESTIMATED RETURN

In order to estimate the photon return the interdependencies of σ_B and $n(z_o)$ are explored.

The product of these quantities is given in [Gardner et al., 1986] as

$$\sigma_B n(z_o) = 3.6 * 10^{-31} \frac{P(z)}{T(z)} \lambda^{-4.0117} \quad (1.30)$$

where $P(z)$ is the pressure as a function of height in mbar and $T(z)$ is the temperature as a function of height in K. Equation (1.30) highlights the $1/\lambda^4$ dependence of Rayleigh scattering.

Pressure as a function of height may be modeled as

$$P(z) = P_o e^{-\frac{z}{H}} \quad (1.31)$$

where $P_0=1,013.25\text{mbar}$ is standard pressure and H is the e-folding height of the atmosphere [Schubert and Walterscheid, 2000] in which

$$H = 29.3 * T[m] \quad (1.32)$$

where T is the temperature in K, and H has the units of meters. So in effect, equation (1.29) is a function of height and temperature.

A polynomial is fit to the values in table 11.21 from Schubert and Walterscheid [2000] to give a continuous function of $T(z)$. Using this polynomial, the Lidar equation (1.29) may be numerically integrated over a range of heights to produce results agreeable to table 1 of [Angel, 2000]. Furthermore, it allows the calculation of table 1.1. In this table the “lossless” column assumes $T_0=\eta= T_A=1$, $\lambda=532\text{nm}$, $N_B=0$, $z_0=25\text{km}$. The “estimated” column assumes values that are reasonable with the experiments reported on in this dissertation, $T_0=0.25$, $\eta=0.5$, $\lambda=532\text{nm}$, $N_B=0$, $z_0=25\text{km}$, and $T_A=0.631$ (averaged value for 500 and 550nm in [Schubert and Walterscheid, 2000]).

Range, Δz [km]	Lossless Return $\left[\frac{\text{Photons}}{W \cdot s \cdot m^2} * 10^6 \right]$	Lossless m_v/W	Estimated Return $\left[\frac{\text{Photons}}{W \cdot s \cdot m^2} * 10^6 \right]$	Effective $m_v/WTOA$
20-30	2.2	9	0.11	9.4
24.5-25.5*	0.18	11.7	0.009	12.2

Table 1.1 The photon return of a Rayleigh beacon. Justification for the 20-30km range is given in section 2.2.2. Further explanation of the table is given in the text.

The m_v values are given per Watt of projected laser power. For the “effective” m_v column the F_{lossless} results are multiplied by a single value $T_A=0.631$ (loss due to upward propagation of laser beacon) before being placed into equation (1.24) to estimate the top of the atmosphere photons. This process is done to stay consistent to the meaning of star magnitude.

As a comparison of the effective m_v/W , Ge[1998] gives values for sodium beacons of about $m_v/W=10.5$.

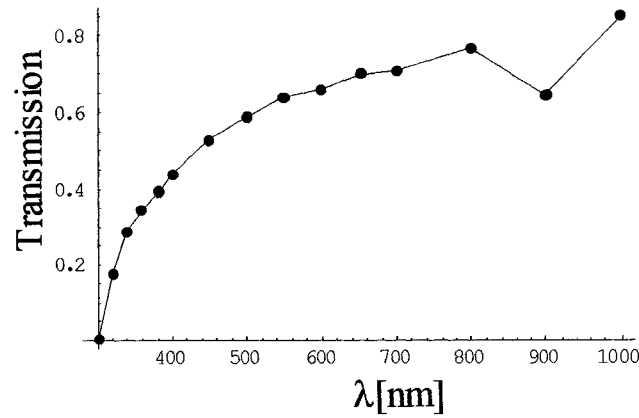
Section 2.2.2 describes why a Rayleigh beacon on the f/15 MMT is limited to the 24.5-25.5km range. Such a range restriction for a low power laser results in an effective

magnitude very near the limit stated in section 1.1.5. From the table, it is therefore seen that there is great photometric advantage of increasing the usable range of a Rayleigh beacon

1.2.6.3 PHOTON RETURN AS A FUNCTION OF WAVELENGTH

Equation 1.29 gives the estimated photon Rayleigh return. The reference [Schubert and Walterscheid, 2000] contains a table (11.25) in which the total atmospheric absorption as a function of wavelength is given. These values are plotted in figure 1.4. If it is assumed that these transmission values are constant as a function of height, the discrete wavelength dependence of the Lidar equation may be numerically integrated. This is also shown in figure 1.4. The graph represents a lossless optical system viewing the return from 20-30km and gives results in [Photons/(J m²)]. It is seen that for wavelengths greater than 400nm, the $1/\lambda^4$ nature of Rayleigh scattering dominates. For wavelengths shorter than 400nm where Rayleigh return is expected to be high, atmospheric transmission dominates.

Total Atmospheric Transmission as a Function of Wavelength



Rayleigh Return from 20-30km range gate as a function of wavelength

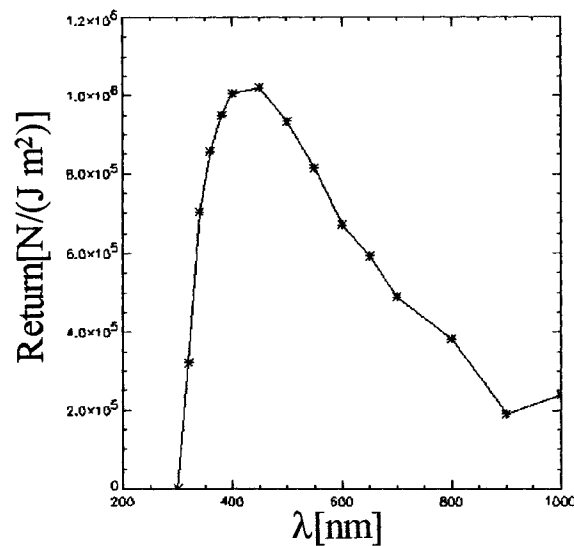


Figure 1.4 The total transmission of the atmosphere as a function of wavelength is shown in the top graph. The lower graph shows the photon return for a dynamically refocused Rayleigh beacon over the 20-30km range-gate as a function of wavelength. For wavelengths greater than 400nm, the $1/\lambda^4$ falloff is dominant. For wavelengths less than 400nm, where the Rayleigh return is expected to be high atmospheric absorption dominates.

1.2.7 DYNAMICALLY REFOCUSED RAYLEIGH BEACONS

Dynamic refocus, DR, is a concept that will extend the useful range of a Rayleigh beacon, allowing the photometric return alluded to in the first row of table 1.1. A schematic version of dynamic refocus is shown on the right side of figure 1.5. In this figure, a Rayleigh beacon projects a pulse into the atmosphere. The pulse rises as a function of time; the three pulses in each diagram (of figure 1.5) may be considered a snapshot of a single pulse as it rises. The left diagram produces schematic image of the beacon analogous to figure 1.2. The pulse begins out of focus on the image plane, rises into focus and continues out of focus. In the right diagram, the dynamic refocus black box keeps the rising pulse in sharp focus. The image of the pulse is now integrated into a seeing limited bright spot at all heights. Table 1.2 states that this image is approximately 12 times brighter than a beacon that is range gated from 26.5-25.5km (the range that limits the $Blur_{\theta}$ to seeing limited, 1arcsec, without DR; see section 2.2.2)

Section 1.2.4 discussed the gains in the sampling that could be made if multiple beacons were employed. Models of dynamically refocused Rayleigh beacons over the range 20-30km with the geometry described in figure 1.3 have been used to produce a three-dimensional, layered atmospheric model of the atmosphere [Lloyd-Hart et al. 2001, Lloyd-Hart and Milton, 2002a, Lloyd-Hart and Milton, 2002b& Milton et al., 2003]. The results of this tomographic model may be used to drive a single mirror AO system. The results may also be used to drive multiple deformable mirrors

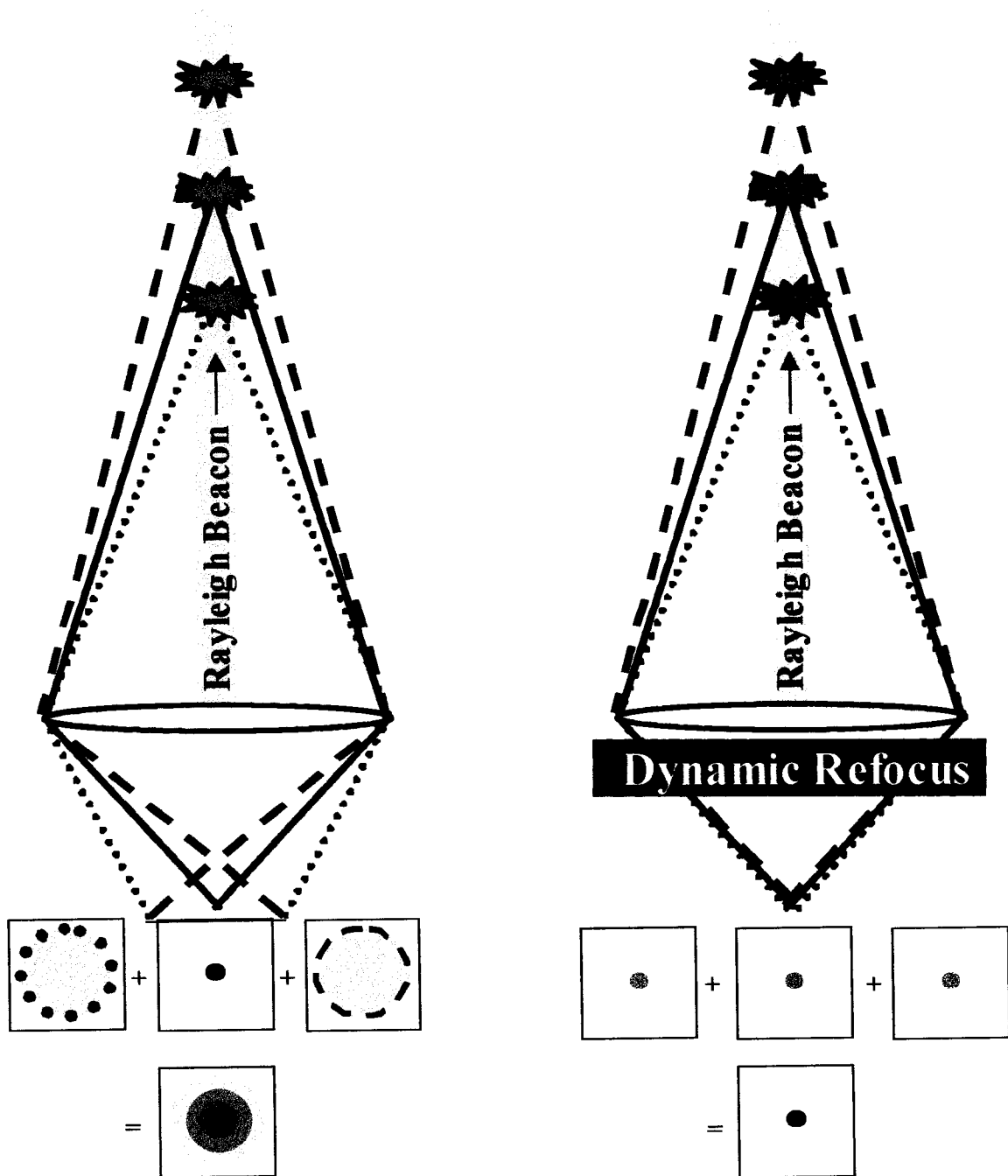


Figure 1.5 A black box definition of dynamic refocus. The left side of the figure shows a system without DR. The right side shows that DR causes the image of the rising pulse to be formed at the same image plane, integrating the rising pulse into one bright image.

that are placed conjugate to different levels of atmospheric turbulence. This is termed multi-conjugate adaptive optics, MCAO and serves to increase the corrected field of view of an AO system to a value greater than the isoplanatic angle.

In references to problems posed in this chapter, dynamically refocused Rayleigh beacons allow many answers. Relatively cheap off-the-shelf lasers are immediately available to project not only single but also multiple Rayleigh beacons. The lasers are of good enough beam quality that an auxiliary beam projector may be used. These beacons may be dynamically refocused to achieve the required photon return that equates each of the multiple LGS to the magnitude required for NGS AO. Dynamic refocus enables the opportunity to investigate MCAO on the MMT with current laser technology, greatly accelerating the timetable considered to implement such a project. Dynamically refocused multiple Rayleigh beacons are a lower cost and more immediate LGS solution than developing even a single sodium beacon.

The lessons learned from DR of Rayleigh beacons on the 6.5m MMT will be applicable to DR of sodium beacons on larger 30m telescopes; the geometries scale almost exactly by a factor of 4. During the time that MCAO is investigated on the MMT using Dynamically refocused Rayleigh beacons, sodium lasers will have time to mature and become viable for 30m-telescope use. It should be noted, that there are key components of DR that do not scale linearly, see equation (1.20). However, the difference is

manageable and 30m sodium DR systems have already been designed and studied [Lloyd-Hart & Milton, 2002].

The remaining chapters of this dissertation will discuss the modeling, design and proving of a DR system for the use on the MMT. The remainder of this chapter first gives a list of LGS efforts and their results and ends with a statement of work.

1.3 LGS EFFORTS AND RESULTS

Current LGS efforts are shown in table 1.2. It is immediately noticed the scarcity of the reported results. Again, this is an insight into the complexity of producing suitable LGS systems.

The last row of this table indicates the results of the dynamic refocus field tests reported on in the remainder of this dissertation as well as photometric results to be reported by Mallik [2004]. The m_v/W (projected Watt) values found in table 1.1 are consistent with the results presented in table 1.2 only if it is taken into account that there is a 60% reduction in photons if the range is not 20-30km but 22.5-32.5km (accounting for the telescope elevation) and a beam projector efficiency of only 30% (Mallik assumes 53%). Such discrepancies will be discussed in Mallik [2004]. Table 1.2 assumes that the beam projector used for the DR results has an efficiency of 50% and the hologram has an efficiency of 67%.

System	LGS	Power	Height	M ² /TDL	FWHM	Eq. m _v	Proj.	References
Thompson feasibility	Na	0.15	Na	NR	83x120	NR	0.6	Thompson & Gardner, 1987
SOR	511& 578	75-200	10	30TDL	2-4	NR	1.5	Fugate, 1994
Whitesands	Na	40mJ/ GHz	Na	4TDL	2.8	NR	1	Humphreys et al., 1991
FASTTRAC	Na	1	Na	NR	0.9x1.3	10.4	0.75	Lloyd-Hart et al., 1995 Ge et al., 1998
Lick	Na	18	Na	NR	2	7	0.3	Max, 1997
Subaru prototype	Na	0.5	Na	1.16	6	NR	0.2	Hayano, et al., 2000
ALFA	Na	5	Na	NR	1.4-3 TSL	NR	NR	Rabien et al 2000 Hippler et al 2000
CHAOS	Na	1.1	Na	NR	1-1.5	9.5	0.76	Shi,2001
UNISIS	351	30	20	1,000 TDL	~1	NR	2.5	Thompson & Teare, 2002
Herschel	523	5	2.6	NR	3.6	NR	0.3	Clark, 2003
Keck	Na	15	Na	NR	NR	9.5	NR	Web press release
61" DR	532	1x5	20-30	1.2	2.5	10.6x5	0.25	Mallik, 2004 & this dissertation

Table 1.2 A summary of LGS results. LGS: Na indicates a sodium beacon or if a Rayleigh beacon is used its wavelength is stated. Power is in watts unless otherwise stated. Height: Na= sodium layer or Rayleigh height is given. M²/TDL: number will correspond to laser's M² or how much it is times diffraction limited, TDL. FWHM: given in arcsec or times seeing limited, TSL. Eq m_v is the equivalent brightness of a visual magnitude star. Proj. is the diameter of the beacon projection aperture. All data that is not reported, NR, is stated.

Reference may be made between the work done at 20-30km presented in this dissertation compared to the 10km work by Fugate [1994].

1.4 STATEMENT OF WORK

It is necessary to state, before this dissertation is presented, the work in which I may and may not claim ownership. The work presented in this dissertation is, in every sense of the term, a team effort.

The idea of dynamic refocus is Roger Angel's. The design of the DR optics is a result of Roger Angel and Roland Sarlot. The development and model presented in chapter 2 is my own work. In chapter 3 the DR optics are presented and attributed to those above. Also in chapter 3 the ringer and driver are presented. Both of these are ideas of Roger Angel developed by Brian Cuerden and Matt Rademacher, respectively. In chapter 4 the experiment is outlined. My duties included the designing and building of the 61" to MMT converter optics, the alignment optics, the MMT test bed and earlier versions of the beam projector. Tom Stalcup is responsible for the beam projector used to collect the data presented as well as the governing electronics and software. Mat Rademacher designed the support structure for the 61" optics and the beam projector. Proteep Mallik investigated the photometric return of the beam projector.

My major contribution has been to understand DR and to bring this experiment to fruition. This includes working on earlier experiments that led to this work, the specific duties outlined above, the system engineering and the management of this experiment.

CHAPTER 2 MODELING OF DYNAMIC REFOCUS

The purpose of this chapter is to develop clear optical and mathematical models for topics necessary to the understanding of dynamic refocus on the MMT and then the 61”.

2.1 INTRODUCTION

As with any complicated and complex optical system a strong paraxial understanding greatly enhances the ability to engineer that system. The components that I felt necessary to gain this understanding of DR are presented in chapter 2. It is my further hope that this first-order development will allow for an almost intuitive feel for the final system. This chapter will begin with the concepts of change in sagittal depth and blur due to a rising laser pulse. This concept of change in sagittal depth, Δ_{sag} will be central to the engineering and understanding of the DR system.

If a rising laser pulse causes a certain amount of Δ_{sag} , then the purpose of DR will be to add an equal and opposite amount to the system. The concept of creating Δ_{sag} by moving an optical reference plane, $\delta z'$ will be presented. This concept will be extended to the idea of moving a mirror in piston. With a mathematical description of the mirror movement, it will be assumed that the mirror may be moved with axial sinusoidal motion. The inherent error in moving the mirror in this manner will be examined.

Up to this point, the description of the system will have been general. One of the main topics of this dissertation is the test of the MMT system on the smaller 61” telescope. An explanation will be made of why using an off-axis subaperture is a complete test. This section will also expand on the idea of the bowtie (figure 1.2).

Using the first order optical concepts presented in this chapter, along with the use of the Lidar equation, a mature model of the 61” return will be outlined and its results presented visually.

2.2 FIRST ORDER OPTICAL MODELS

Section 2.2 will concentrate on paraxial and first order optical definitions, terms and concepts important to understanding and engineering of dynamic refocus.

2.2.1 SAGITTAL DEPTH AND Δ SAG

The change in sagittal depth, Δ sag of the wavefront created by a rising pulse plays a principle role in the understanding and thus the engineering of any dynamic refocus system. The sagittal depth of a wavefront is defined as

$$sag = \frac{\rho^2}{2ROC} \quad (2.1)$$

where ρ is the axial extent (radius) of the wavefront, and ROC is the radius of curvature of the wavefront. Δsag is the difference in sagittal depth between two wavefronts,

$$\Delta sag = \frac{\rho^2}{2} \left(\frac{1}{ROC_1} - \frac{1}{ROC_2} \right) \quad (2.2)$$

where ROC_n is the radius of curvature of the n^{th} wavefront and it is assumed that ρ does not change per wavefront. The Δsag of a rising laser pulse may then be described as

$$\Delta sag = \frac{\rho_{EP}^2}{2} \left(\frac{1}{z_1} - \frac{1}{z_2} \right) \quad (2.3)$$

where ρ_{EP} is the radius of the entrance pupil and z_n is the height of the laser pulse at position n .

Δsag through an optical system with $\rho_{EP} = \rho_{XP}$ (exit pupil) is examined (figure 2.1). One may prime the quantities in equation (2.3) to understand the change in sagittal depth after the telescope.

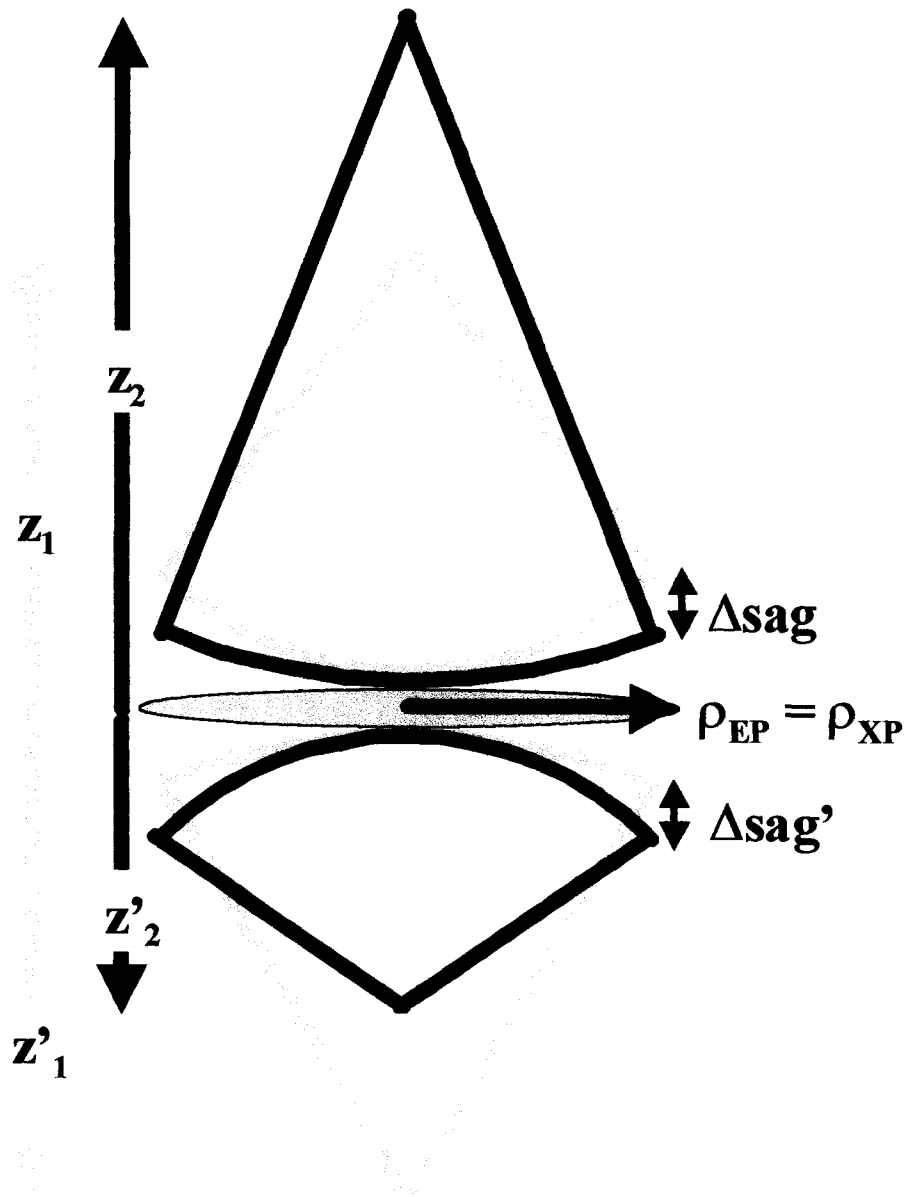


Figure 2.1 The change in sagittal depth of a pulse rising from height z_1 to z_2 is shown schematically above. The $\Delta\text{sag}'$ is also examined for the image conjugates. In this schematic example, it is assumed that the radii of the entrance and exit pupil are equal.

$$\Delta sag' = \frac{\rho_{EP}^2}{2} \left(\frac{1}{z'_1} - \frac{1}{z'_2} \right) \quad (2.4)$$

If substitutions for the $1/z'_n$ terms are made using the Gaussian image equation

$$\frac{1}{z'} = \frac{1}{z} + \frac{1}{f} \quad (2.5)$$

it is immediately seen that the $1/f$ (focal length) terms are canceled with the result $\Delta sag = \Delta sag'$. So as long as the temporal order of the pulses is maintained (z_1 and z'_1 always occur before the pulse rises to z_2 and z'_2) then it can be stated that Δsag is conserved. Upon closer examination, it is noted that Δsag is equivalent to the defocus aberration coefficient W_{020} , which is known to be conserved throughout optical systems.

A definition for W_{020} may be rewritten as

$$\delta z' = 8Fn^2 \Delta sag \quad (2.6)$$

where Fn is the $f/\#$ of the light exiting the optical system and $\delta z'$ is the image shift ($z'_1 - z'_2$) due to an amount of Δsag (W_{020}) present in the optical system. Equation (2.6) states a change in focal plane position is created when there is an amount of defocus in the

system, which is an intuitive definition of defocus. It may also be interpreted as: an amount of defocus is introduced when the conjugate focal plane is moved by an amount $\delta z'$. It is this latter interpretation that will allow for the first example of dynamic refocus to be made.

If a rising pulse introduces an amount of Δs_{ag} (W_{020}) and thus moves the conjugate image plane an amount $\delta z'$ then an equal and opposite amount of Δs_{ag} may be created by moving a focal plane (for example a CCD) the same amount $\delta z'$ in order to keep up with the image of the rising pulse. In other words, the CCD is kept conjugate to the rising laser pulse. This trivial solution of dynamic refocus may be calculated for the $f/15$ MMT case ($\rho_{EP} = 3.25\text{m}$, $f/\# = 15$). The Δs_{ag} term is most easily calculated by using the pulse heights on the sky, assuming $z_1 = 20\text{km}$, $z_2 = 30\text{km}$, then $\Delta s_{ag} = 88\mu\text{m}$. By equation (2.6) this yields a $\delta z' = 158\text{mm}$. The time it takes light to travel from 20 to 30km in double pass is $66\mu\text{s}$, giving the moving focal plane a speed of 2.4km/s or $5,316\text{mph}$ ($2,400\text{m/s}$). This is obviously not a practical speed to move anything physical like a CCD camera or any other wavefront sensing instrument.

In summary, Δs_{ag} (W_{020}) is the basic quantity induced by a rising laser pulse. Therefore any dynamic refocus system needs to introduce an equal and opposite amount of Δs_{ag} to the optical system to counteract the effect of the rising pulse. A relationship may be made between Δs_{ag} , which can easily be computed using the heights of the pulse in the

sky, and the movement of the conjugate image plane $\delta z'$. The trivial solution of moving an instrument to follow the image conjugate is not physically practical.

2.2.2 BLUR DUE TO A RISING LASER PULSE

In the introduction of DR contained in chapter 1, the idea of blur due to a rising laser pulse was presented. This topic is revisited here, with more mathematical intentions. Three discrete laser pulse heights (Height 1-3) are shown in figure 2.2. These discrete heights are considered to be for the same laser pulse as it rises through the atmosphere. The telescope imaging the pulses is schematically shown as a single positive lens. A fixed image plane is shown following the telescope, which is taken to be the conjugate image plane for the pulse when it is at Height 2.

For the MMT, the Rayleigh beacon is to be projected from behind the secondary, in the figure this is represented as the laser pulses leaving from the center of the telescope. By design of the MMT beam projector it is a fair assumption that the beacon is nearly collimated over the range of interest so the pulses do not change size. For the purpose of this discussion the pulses are assumed to be point sources.

When the pulse is at the lower position, Height 1, the marginal rays (dotted lines) come to a focus somewhere below the fixed image plane. The image size, or blur at the fixed

plane when the pulse is at Height 1 may be approximated by the diameter given by the marginal rays. At Height 2, the marginal rays (solid lines) come to a focus, so the image size is limited by the seeing conditions (or under exceptional cases, by diffraction). For Height 3, the pulse is rising toward infinity, thus the image is asymptotically approaching the focal plane of the telescope, which lies above the fixed plane. Again, the blur may be described by diameter of the marginal rays (dashed lines). In this contrived figure, the blur for Height 1 and Height 2 are drawn as equal, this of course is not true in general.

It is of interest to understand the angular size of this blur as it relates to the distance the pulse travels either to or from a nominal height z_0 , in this example Height 2. As stated in section 2.2.1, $\delta z'$ is the change in conjugate distance for a pulse traveling through the atmosphere. By the definition of $f/\#$

$$Blur = \frac{\delta z'}{Fn}. \quad (2.7)$$

An angular measure of the Blur is obtained by assuming $\delta z' \ll f$ (focal length of the telescope), then in radians

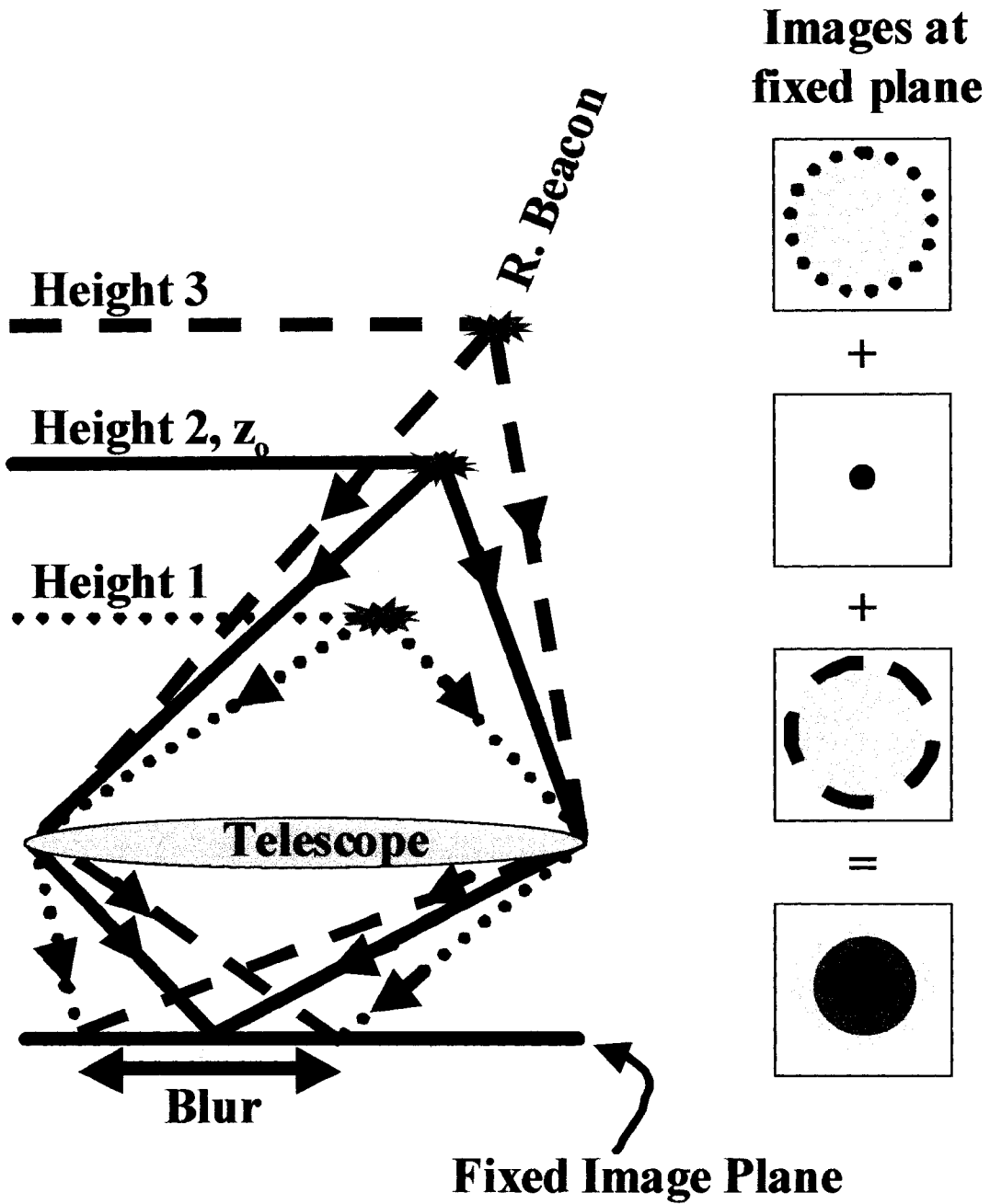


Figure 2.2 The blur due to three discrete heights of a single rising pulse is schematically shown. Height 2 comes to a focus at the fixed image plane. Height 1 and 3 come to a focus below and above the fixed plane. The images at the focal plane are schematically integrated on the right.

$$Blur_{\theta} = \frac{Blur}{f}. \quad (2.8)$$

Substituting equations (2.3) and (2.6) into (2.8) and using $z_1 = z_0$ and $z_2 = z_0 + \delta z$

$$Blur_{\theta} = D \left(\frac{1}{z_0} - \frac{1}{z_0 + \delta z} \right). \quad (2.9)$$

where D is the diameter of the telescope. This may be solved for δz in terms of $Blur_{\theta}$ in arcseconds, B_{arcsec}

$$\delta z = - \left(\frac{5 \cdot 10^{-6} B_{arcsec}}{D} - \frac{1}{z_0} \right)^{-1} - z_0. \quad (2.10)$$

Equation (2.10) yields an approximation of how far from z_0 a pulse may rise if the $Blur$ is constrained to a certain value. In the case of the MMT ($D = 6.5$, $z_0 = 25\text{km}$) where the $Blue_{arcsec}$ is constrained to 1 arcseconds, δz is then limited to $\pm \frac{1}{2}$ km.

The Lidar equation (1.29) gives the number of photons detected from a laser pulse at a given height over a particular range gate. If the center height is taken as 25km and the

range gate is taken as 1km (assuming perfect transmission of atmosphere and optics as well as 100% QE) then number of photons collected, $N_{\text{photons}} = 180,000[\text{photons}/(\text{Joule m}^2)]$.

The goal of DR is to allow a larger range gate in order to collect more photons which are to be concentrated in a nearly seeing limited spot at a fixed image plane. If the same conditions outlined above are kept but the range gate is extended from 1 to 10km, then $2.2 \cdot 10^6[\text{photons}/(\text{Joule m}^2)]$ are collected, 12 times more than the non dynamic refocused case. With this extended range gate ($\delta z = \pm 5\text{km}$ about 25km) equation (2.9) yields a $\text{Blur}_{\theta} = 13.4\text{arcsec}$. Reducing this Blur value to nearly seeing limited will be the purpose of the dynamic refocus system modeled in the next section.

2.2.2.1 A NOTE ABOUT BEAM TILT

As discussed in chapter 1 and shown in figure 2.1, the projected Rayleigh beacon will be off-axis. None of the discussion in this chapter makes any mention to this fact. The reason is that the tilt of the beacon is quite small, 60 arcsecs, so the $1/\text{Cos}(\theta)$ distortion of the image is negligible and maybe ignored. The term that may not be ignored is the distance away from the telescope axis the images are formed; in the case of the MMT, $97.5\text{m} \cdot \text{Tan}(60\text{arcsecs}) = 28.4\text{mm}$. This is a substantial distance can be seen in figure 2.1 as the longitudinal distance from the center of the telescope to the in focus image on the fixed image plane. However, most quantities in this chapter are delta (δ, Δ) quantities that

represent “change in” some measurement. So, for the case of actual position on the focal plane, one may simply add the delta quantities to a fixed offset, for example the result of equation (2.19) to the 28.4mm result (from above) to get an absolute number. However, for the rest of this chapter such details will be ignored for the sake of simplicity.

2.2.3 MODELING OF MMT DYNAMIC REFOCUS SYSTEM

This section will use the first order optical properties discussed thus far to produce a model of the MMT dynamic refocus system. A more reasonable yet still impractical system will be examined as the next step. The optical properties outlined in the last 2 sections will then be exploited to create a more practical system. A mathematical model for this system will be presented. In practice this DR method will have an inherent amount of error; this error will be considered resulting in a model that will predict the geometric performance of the MMT system.

Toward the end of section 2.2.1, a trivial version of a dynamic refocus system was discussed. This system had a movable image plane that simply followed the image conjugate as the pulse rose through the atmosphere. In practice one would never actually move a wavefront sensing system, but a system may be conceived of that uses a moving mirror to create a fixed image plane. This next iteration of understanding dynamic refocus will temporarily suspend the notion of anything at a speed of a few thousand mph.

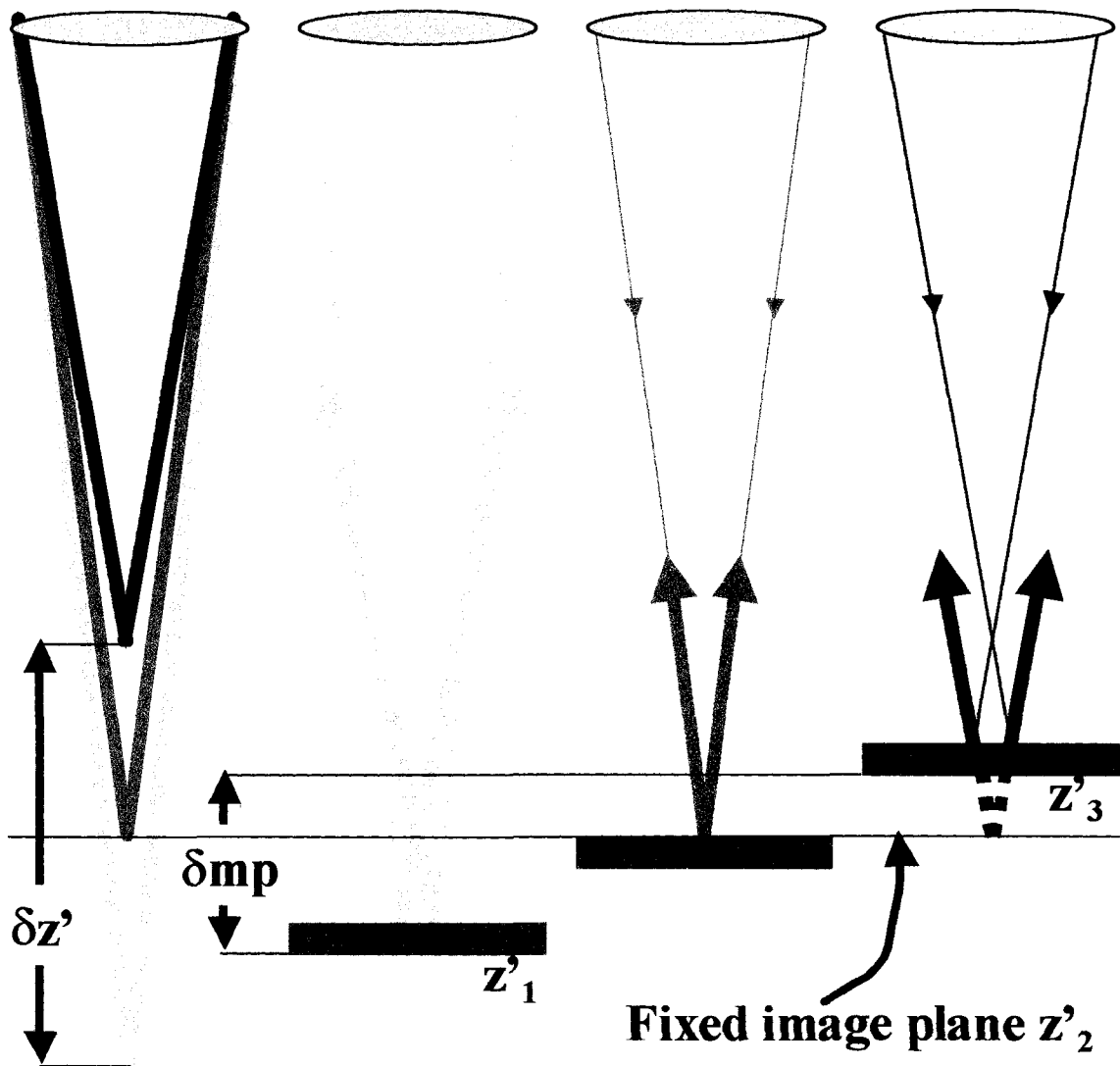


Figure 2.3 In this figure, a mirror is moved δmp in concert with a rising image $\delta z'$. The incoming light is drawn with thin lines and the reflected light is emphasized, being drawn with thick lines. As a result of the moving mirror, the reflected marginal rays drawn all seem to come from the fixed image plane. The virtual image created in the far right case is drawn with dashed lines. It is noted that the mirror need only to move half of the distance of the rising pulse.

In order to create a fixed image plane, something has to be done to counteract the Δs_{ag} introduced by the rising laser pulse. A moving mirror may be used in to create a fixed image plane. In figure 2.3 three discrete image conjugates of a rising laser pulse are examined. Incoming light is drawn as thin rays. The light reflected from the moving mirror is emphasized and drawn as thicker lines.

The conjugate plane z_2' will be taken as the fixed image plane. For all conjugates the mirror is to be positioned so that the reflected light appears to be coming from the z_2' plane. For the z_1' light (light gray tone) the mirror is placed halfway between the z_2' and z_1' planes. For the z_2' rays (middle gray tone) the mirror is situated at the z_2' plane as to retro-reflect the light. The mirror is again placed halfway between the z_3' and z_2' planes for the z_3' light (dark gray tone); in this case the mirror causes a virtual image to be formed at the z_2' plane (shown as the dotted rays). By positioning the mirror in this manner, any optical system following the mirror will see a fixed image plane at the z_2' location. Furthermore, it is noted that the mirror position movement δm_p is half of the conjugate plane movement,

$$\delta m_p = \frac{1}{2} \delta z'. \quad (2.11)$$

The velocity of the moving mirror has been reduced, by half, to 2,658mph so this model of dynamic refocus is more reasonable in the sense that it does not require moving a wavefront sensing instrument but it is still not practical due to the high velocities required.

For a practical dynamic refocus system $\delta z'$ needs to be drastically reduced. Through examination of equation (2.6) it is noted that Δs_{ag} is invariant through the system so $f/\#$ is left as the value to exploit. As an example, if the MMT system ($\Delta s_{ag} = 88\mu\text{m}$) could be changed $f/0.6$ then $\delta z'$ is drastically reduced to $253\mu\text{m}$, which results in a velocity of 8.5mph (which is a reduction of 625 from the former 5,316mph).

So for DR, a principle optical goal is to greatly reduce the $f/\#$ of the light exiting MMT. The specific engineering of such optics will be dealt with in Chapter 3, for now these optics will be treated as a black box objective that speeds up the MMT light to $f/0.6$. A diagram analogous to figure 2.3 may be created for the $f/0.6$ light (figure 2.4). Unlike figure 2.3, figure 2.4 shows a concave mirror instead of a plane mirror. It will be seen in Chapter 3 that the concave mirror allows for the dynamic refocus of off axis light which was a parameter mentioned in section 1.2.7.

Equation (2.11) states that the plane mirror moves half that of the image conjugate distance. In figure 2.4 a similar argument is made for the curved mirror. The DR

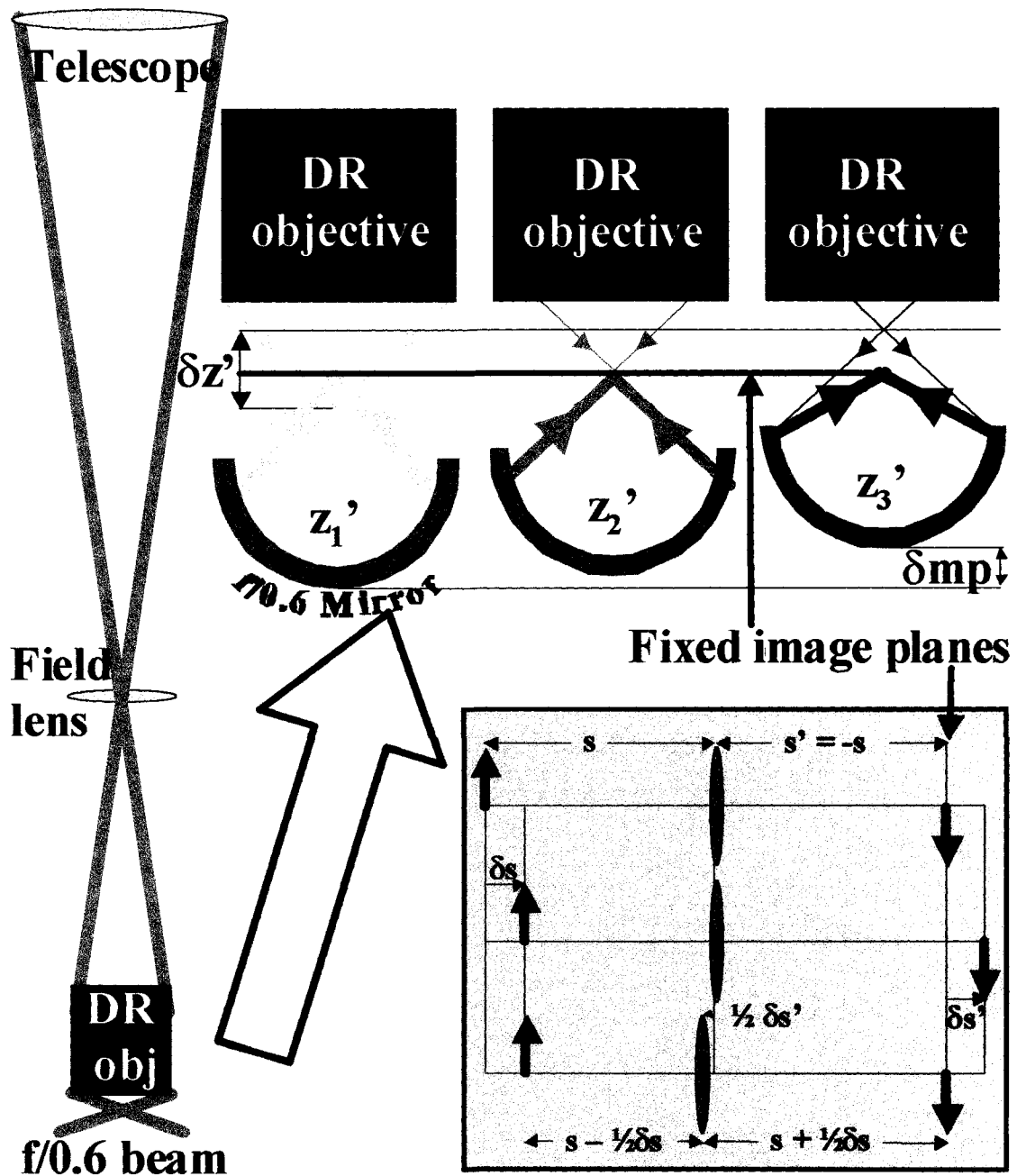


Figure 2.4 This figure is analogous to figure 2.3 in showing a mirror moving in concert with a rising laser pulse. In this figure the rising laser pulse is imaged through an optical system that speeds up the light to $f/0.6$. The concept of a powered element (in a $4f$ imaging system) moving half of the image motion is shown in the gray inset.

objective speeds up the light to $f/0.6$ (left side of figure 2.4). This $f/0.6$ light is matched by deeply curved mirror (top of figure). So if the incoming image conjugate (thin rays) is placed at the center of curvature, COC, of the mirror (z_2' case) then light is retro-reflected placing a return image (thick rays) back at the COC.

When an object and image are both at a concave mirror's COC the mirror is operating in the $4f$ or $M_{\text{transverse}} = -1$ condition and thus $M_{\text{axial}} = 1$. For visualization purposes this situation is shown with a refractive element in the grayed inset of figure 2.4. If an object is moved a small amount δs its image is also moved $\delta s' = \delta s$, since $M_{\text{axial}} = 1$. If the optical system is moved an amount $-\frac{1}{2}\delta s$ it can be considered to “split the difference” and place the image back at the original location. Therefore, if s is the radius of curvature of the mirror, and δs is small, then in the paraxial approximation equation (2.11) holds for a powered mirror as well.

The top of figure 2.4 shows the concave mirror moving in concert with the rising pulse (at three discrete heights) in order to keep a fixed image plane at the z_2' plane. This fixed image plane may then be re-imaged by any optical system following the moving mirror.

The last element in this drawing is the field lens shown on the left hand side. The field lens images the telescope pupil very near the entrance of the dynamic refocus objective.

This allows small diameter optics to be used in the objective, even if the beacon light is off axis (again, refer to Chapter 3).

At this point, all of the parameters for the MMT dynamic refocus system have been discussed. Attention will now be turned away from the physical elements in the system and toward the first order modeling. The fundamental aspects of the model have already been discussed. Equation (2.6) defines the image conjugate motion given an amount of Δs_{ag} in the optical system. In the previous examples, and in general, this value is most easily computed using the change in heights of the rising laser pulse; 20-30km on the 6.5m MMT yields $\Delta s_{ag} = 88\mu\text{m}$. If an objective is used to speed up the MMT's $f/15$ light to $f/0.6$ $\delta z'$ is reduced to $253\mu\text{m}$. As outlined in figure 2.4, a curved mirror travels half the distance as the image conjugate when the object and image are placed near the mirror's COC, equation (2.11). The result of combining equations (2.11) and (2.6) is the model for MMT's dynamic refocus system

$$\delta m_p = 4Fn^2 \Delta s_{ag}. \quad (2.12)$$

Utilizing the developing example, $\delta m_p = 126\mu\text{m}$ and the mirror's velocity is now only about 4mph, more than three orders of magnitude less than the speed of the rising image conjugates of the native MMT. With these parameters, equation (2.12) is plotted in

figure 2.5. The mirror position in microns is plotted against distance the laser pulse is from 25km conjugate (δz from $z_0 = 25\text{km}$ on the sky).

2.2.4 PISTON MOTION OF THE CONCAVE MIRROR

In the last section trade-offs were made between first order optics and practical optical considerations resulting in the simple model, equation (2.12) of the MMT DR system.

This section will also make a very practical decision about the mirror motion described in that model. This decision will lead to inherent errors. These errors will be considered in creating a more complete model of the system.

Figure 2.5 shows the travel of the $f/0.6$ mirror exactly following the rising laser pulse. Unfortunately this is not a nicely behaved path that can easily be fit to something simple, i.e. linear piston movement. The motion shown is for a single laser pulse rising in the sky. The DR system must seek to utilize all pulses possible, so consideration must be made of the repetition rate of the laser.

The pulse rate of the laser is determined by the particular lasing media used. The media is determined by the wavelength of light desired. The wavelength is usually determined by application. The Lidar equation (1.29) states that there will be some amount of return from any wavelength greater than zero so the choice of laser depends on

δ_{mp} as Function of Conjugate Height for MMT Light Sped Up to f/0.6

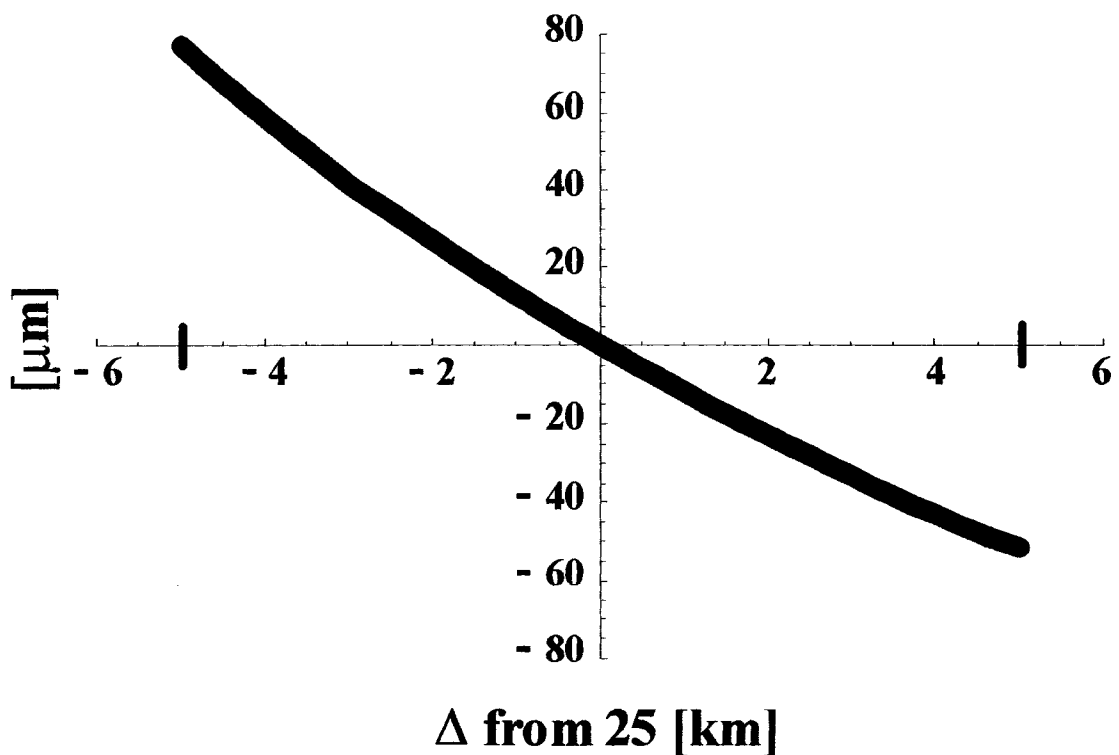


Figure 2.5 This mathematical curve is a result of equation (2.12) being used for the case of a laser pulse rising from 20 to 30km, imaged by the MMT and then reimaged through an f/0.6 DR objective. The change in mirror position is shown as a function of conjugate laser pulse height relative to 25km. The mirror motion is shown in microns.

some “other” multidimensional trade study. Such a study is beyond the scope of this section and even this dissertation. For now, an argument could be made for choosing a laser solely based on cost, availability and ease of use. These qualities fit very well into the maxim discussed in chapter 1 concerning the use of a Rayleigh LGS’s for an accelerating MCAO capabilities on the MMT. This being the case, a doubled Nd:YAG (532nm) off-the-shelf system was chosen. It is a Lightwave Electronics Q201-HD laser head. This laser will operate as low as 5kHz and emit an average power of 15W.

The result of choosing this laser is that the curve in figure 2.5 will need to be repeated 5,000 times a second. Again, it would be beyond the scope of this chapter and this dissertation to present a trade study into what instrument would allow such movements. This chapter is to develop a first order theory of DR and chapter 3 will discuss the engineering of our moving mechanism in more detail.

Examining figure 2.5, one may say it looks approximately linear with some positive concavity. Also knowing this curve must be repeated at 5kHz, sinusoidal mirror motion may be suggested. An RMS fitting routine is employed to fit the curve in figure 2.5 to a sinusoid. The resulting sinusoid will give the mirror position as a function of laser pulse height in the atmosphere or (dividing by $c/2$) time. This fit is shown in figure 2.6, and the resulting equation is

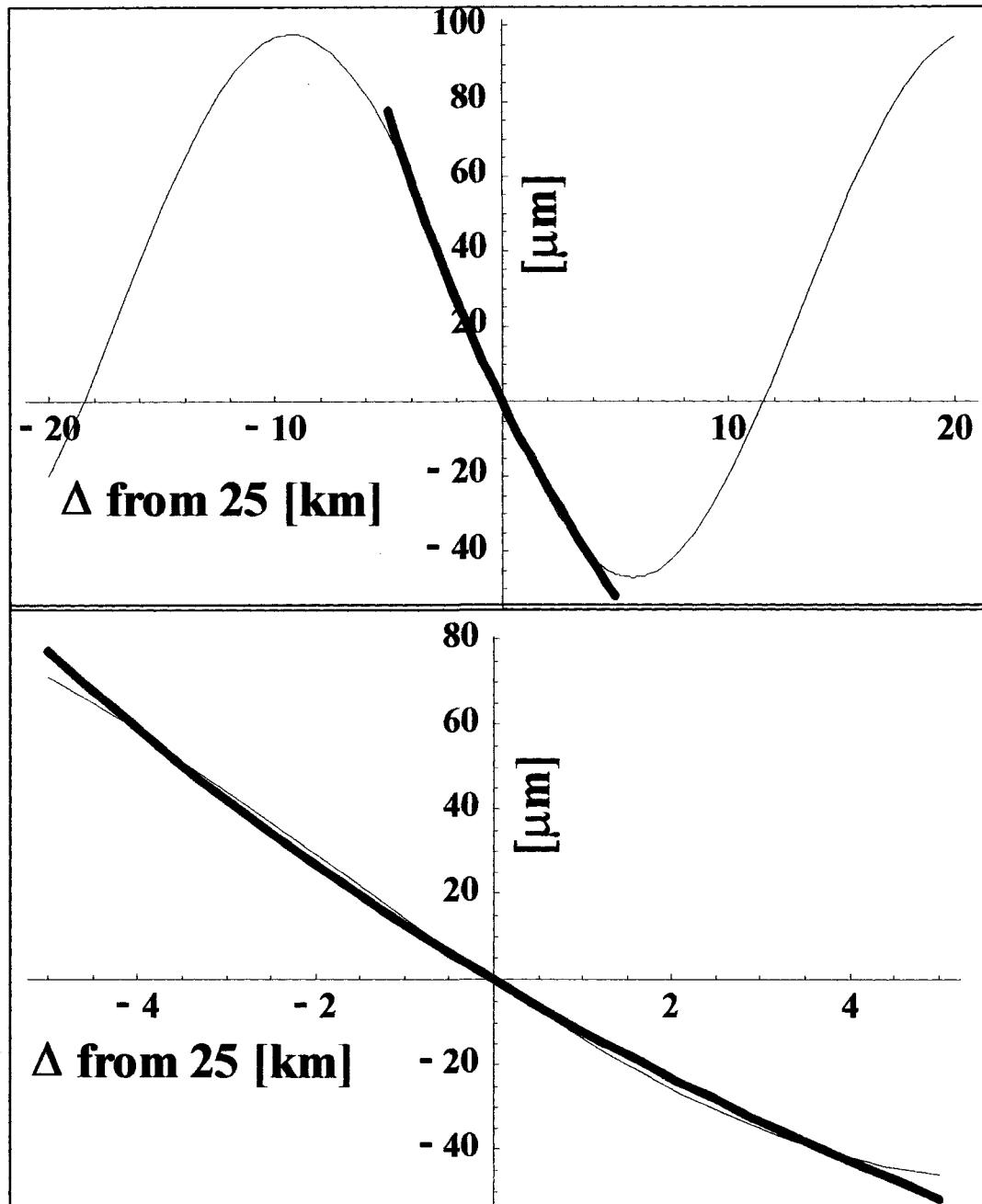


Figure 2.6 This figure shows the mathematical curve of figure 2.5 (dark thick line) fit to a sinusoid (thinner line). The top portion of this figure shows the fit over a period and a half of the sinusoid. The lower portion shows the fit only over the portion of the sinusoidal movement conjugate to 20-30km. The mirror movement is shown in microns vs. pulse height conjugate relative to 25km.

$$\partial mp = A \cdot \text{Sin}\left(\omega \frac{(z - 25\text{km})}{c/2} + \phi\right) + DC. \quad (2.13)$$

which has the following parameters. A is half of the peak-to-peak amplitude that mirror must move. ϕ is the phase of the sine wave when the mirror is conjugate to zero height; the phase between the zero km conjugate and the zero crossing of the sine wave ($\text{Sin}(0)$ condition) is nominally the laser delay trigger (if the triggering system occurs at zero crossing). Therefore, zero-crossing height is $(25\text{km} - (\phi \cdot c/2)/\omega)$. The laser delay in seconds is then, $(25\text{km}/(c/2) - \phi/\omega)$. The DC term is a piston term with units of meters (or in general length). It describes how much the mirror is moved in static piston from its 25km position. If, in a real system, the DR optics were statically aligned so that they were operating in the 25km conjugate configuration, the mirror must then be moved the amount DC in order to run dynamic refocus.

To this point, a general dynamic refocus system has been described. The amount the image conjugates change $\delta z'$ was drastically reduced by passing the light through a fast optical system. A curved mirror is moved in motion in order to reimage the rising laser pulse at a fixed image plane. The motion of this mirror is described exactly (paraxially), but a more practical solution would be to move the mirror sinusoidally. This sinusoidal motion has parameters that are found by fitting a sine wave to the exact (paraxial) solution for the mirror movement.

2.2.5 IMAGE DUE TO DYNAMIC REFOCUS

The concepts developed thus far allow a model to be created that give the geometrical image size as a function of laser pulse height in the atmosphere. Equation (2.13) describes the motion of the mirror used to give dynamic refocus. Equation (2.12) may be solved for to give the Δsag created by a moving mirror. (From this point on, care will be taken to describe the $f/\#$ of the space the mathematics describe.) This process will be done using the MMT as an example. The moving mirror happens when the light has been sped up to $f/0.6$, or f/DR space, therefore the sag created by the moving mirror will be

$$\Delta sag_{mirror} = \frac{\partial mp}{4Fn_{DR}^2} \quad (2.14)$$

where from this point on (unless otherwise stated) δmp will be the shorthand notation for the actual sinusoidal motion of the mirror described in equation (2.13). This Δsag_{mirror} was created to counteract the Δsag_{sky} describe in equation (2.3) where z_1 can be taken as $z_{25}=25km$ and z_2 is the location of the rising pulse. A residual Δsag is then created by subtracting these two

$$\Delta sag_{residual} = \Delta sag_{sky} - \Delta sag_{mirror}. \quad (2.15)$$

The resulting change in conjugate distance, in MMT space, is then found by using equation (2.6)

$$\partial z'_{residual} = 8Fn_{MMT}^2 \Delta sag_{residual}. \quad (2.16)$$

It is important to emphasize that this is the conjugate image movement in MMT space, after the light has gone through the DR system and been reimaged back into MMT space (please look forward to chapter 3 to see why this was done). The residual blur is easily found by utilizing equation (2.7)

$$Blur_{residual} = \frac{\partial z'_{residual}}{Fn_{MMT}} \quad (2.17)$$

This is the complete geometric model for dynamic refocus on the MMT. To modify this to a more realistic model two things remain to be done, allow amplitude of the blur circle to vary with pulse height as per the Lidar equation and convolve the geometric result with a kernel indicative of the atmospheric seeing. This model has been developed as a first

order paraxial construction; it does not include aberrations of the optics. Such a topic is outside the scope of this chapter but will be discussed, in part, in section 4.3.2.

2.3 OPTICAL MODEL ON THE 61”

The model developed in section 2.2 was done in general, with examples given for the MMT. The model assumed that the full MMT aperture was collecting and imaging the light. This dissertation covers the test of the MMT DR system on the smaller 61” telescope on MT. Bigelow. The details of how the 61” was configured for this test are given in section 4.3. This section will further develop the model of the last section using an off axis subaperture of the MMT. As well as adding to the intuitive understanding of the system, I hope to show that this is an effective test for the full MMT DR system.

2.3.1 EFFECT OF USING AN OFF-AXIS SUBAPERTURE

Geometrically the effect of using an off-axis subaperture is simple, the blur circle due to a subaperture is just a “masked” version of the blur circle for the full aperture. This concept may be seen schematically on the right side of figure 2.7. This figure is analogous to figure 2.2, except that in the present case the aperture is masked and light is only imaged through an off-axis subaperture. On the right side of the figure the blur circle due to the subaperture is shown with respect to the blur circle that would be created by the full aperture. When the pulse is at Height 1 (dotted lines with white background) the conjugate image is formed somewhere below to fixed image plane and the geometric

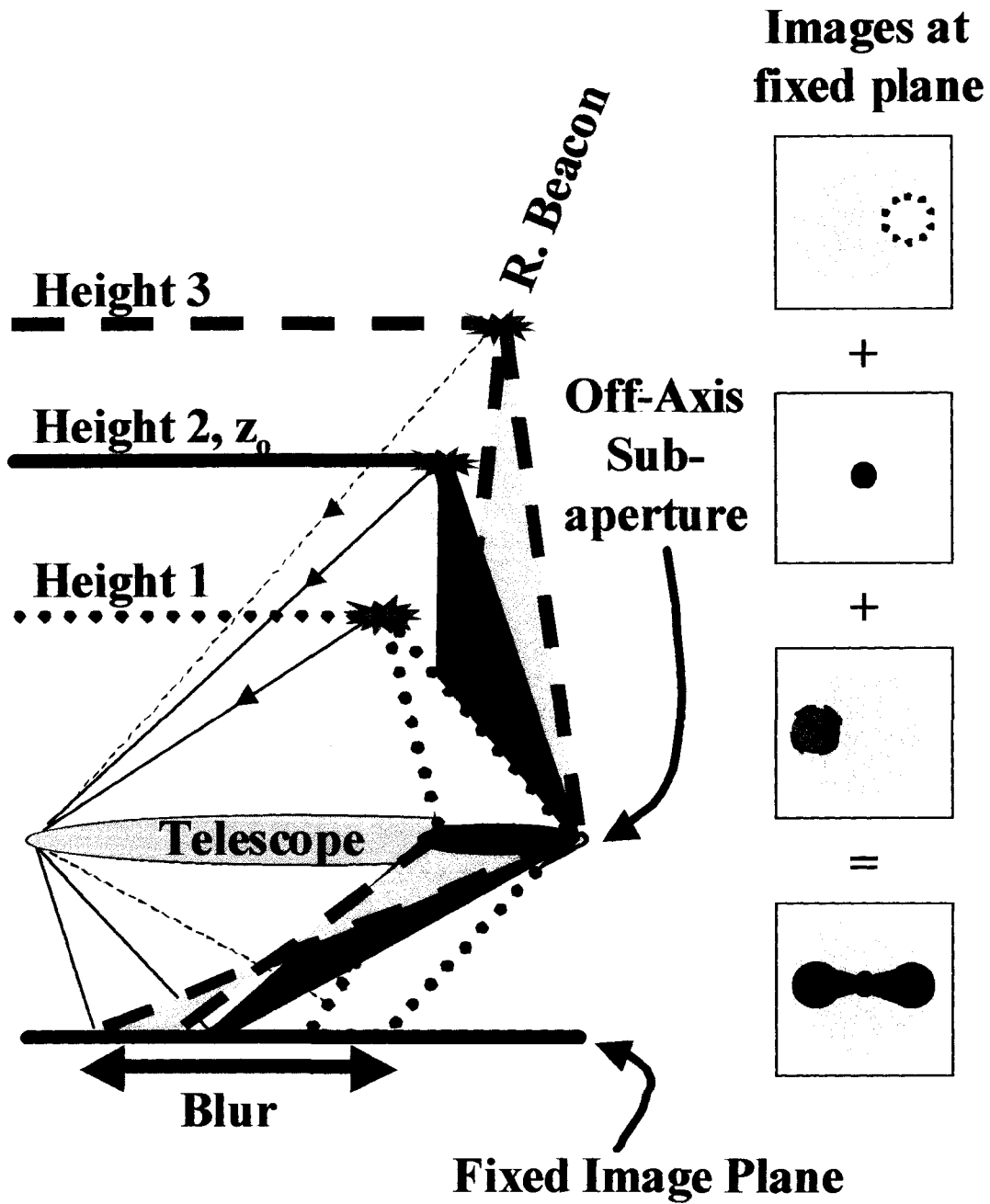


Figure 2.7 This figure is analogous to figure 2.2. In this figure light is considered from an off-axis subaperture. The light is schematically integrated to the right to form a "bowtie" image.

defocused blur circle lies to the right of the image of the light coming from Height 2 (solid line and dark gray color), which is conjugate to the fixed image plane. Likewise, for light from Height 3 (dashed lines, medium gray tone), the light comes to a focus somewhere above the conjugate plane and the blur circle occurs to the left.

The “integrated” image of these three cases is shown in the bottom right of the figure is a “bowtie”. This bowtie image has the same length as the diameter of the full aperture blur. This is of course a contrived situation, but close to what is expected for a pulse rising from 20 to 30km with a fixed image plane conjugate to 25km.

The length of the bowtie can be estimated. For the MMT full aperture, the blur circle diameter at 20km (using equation (2.9)) is 13.5arcsecs. For 30km it is 9arcsecs. This makes the bowtie length, in the geometric approximation, $\frac{1}{2} 13.5 + \frac{1}{2} 9 = 11.25$ arcsecs. The effect of dynamic refocus will be to reduce this bowtie length to a seeing limited spot and to “center” it. This is the dramatic effect of using DR on an off axis subaperture.

2.3.2 MODELING OFF-AXIS SUBAPERTURE

Figure 2.7 schematically shows the effect of the off axis subaperture. This section will extend the model created in section 2.2 to the case where an off axis subaperture is employed.

The first modification of the model is to the defocused blur circle created by the subaperture as opposed to that of the full aperture, which is described by equation (2.17). The only change made to this equation is to modify the $f/\#$. The off-axis subaperture has a smaller diameter aperture, thus a higher $f/\#$ and therefore a smaller blur circle than would be created by the full aperture. This is what has been schematically shown in figure 2.7. The blur circle size is then given by

$$Blur_{residual} = \frac{\partial z'_{residual}}{Fn_{subap}}. \quad (2.18)$$

Using a 61" off-axis subaperture on the MMT $f/subap = (61"/(15*6.5)) = 63$.

The next thing to consider is the centroid of the blur circle as a function of pulse height. Since, geometrically, the subaperture blur circle is just a masked version of the full aperture blur, the model only requires the constant off set, l , between the center of the full aperture to the center of the subaperture (figure 2.8). This offset can be normalized, p , and then multiplied by the full aperture blur circle (equation (2.17)) to give the subaperture centroid location. If a "local" chief ray was drawn from the subaperture center, its position would always coincide with the geometric subaperture centroid location and is given by

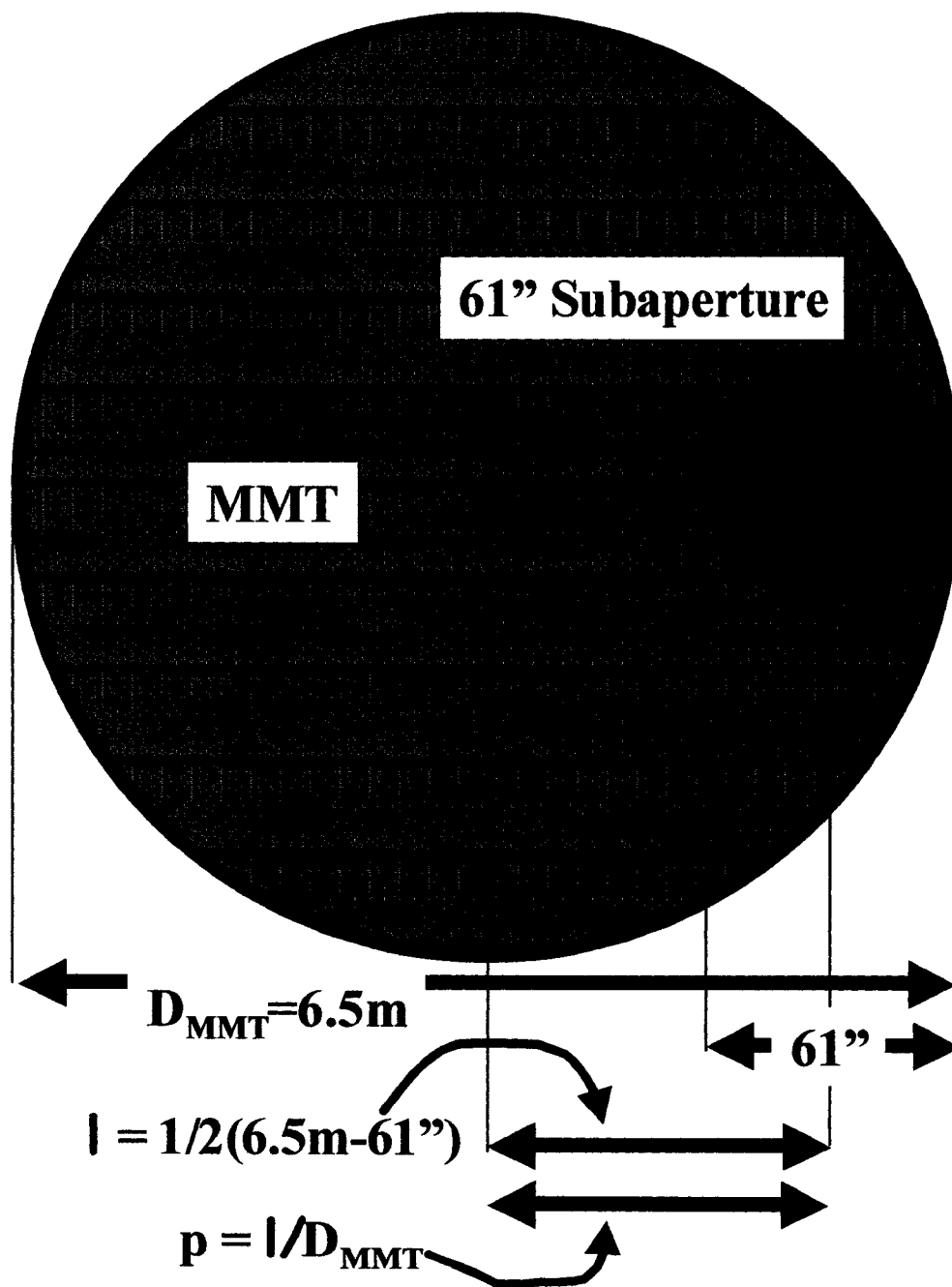


Figure 2.8 An off-axis subaperture of the MMT is shown geometrically above. This construction allows for the definition of the normalized proportionality factor, p , which is the offset of the subaperture blur circle from the full aperture blur circle.

$$\Delta ybar = p \cdot \frac{\partial z'_{residual}}{Fn_{MMT}}. \quad (2.19)$$

In summary, chapter 2 used first order, paraxial and geometric concepts to create a model for DR on the MMT using its full aperture as well as an off-axis subaperture. Chapter 2 also introduced simple concepts in order to understand the much more complex problem of dynamic refocus. The specific manner in which these concepts were implemented to engineer and test the DR system, and the subsequent results are the subject of the rest of this dissertation.

As a recap, the general steps taken to create a DR model would resemble:

- Find the Δsag_{sky} created by a rising laser pulse
- Find the Δsag_{mirror} created by a sinusoidally piston moving mirror
- Difference Δsag_{sky} and Δsag_{mirror} to get $\Delta sag_{residual}$
- Use $\Delta sag_{residual}$ to obtain $\delta z'$
- Use $\delta z'$ to get values for $Blur_{residual}$ (and $\Delta ybar$ if using an off-axis subaperture)
- Multiply the $Blur_{residual}(z)$ values by the photon return obtained from the Lidar equation

- Integrate the photon weighted $\text{Blur}_{\text{residual}}(z)$ circles to obtain an image
- Convolve the integrated image by a kernel indicative of double pass seeing

The results of such a model for a 61" off-axis subaperture are shown in figure 2.9. The top case shows no range-gating, the bottom case shows a 20-30km range-gate. In both cases, the geometric results are convolved with a 1arcsec (double-pass) seeing kernel.

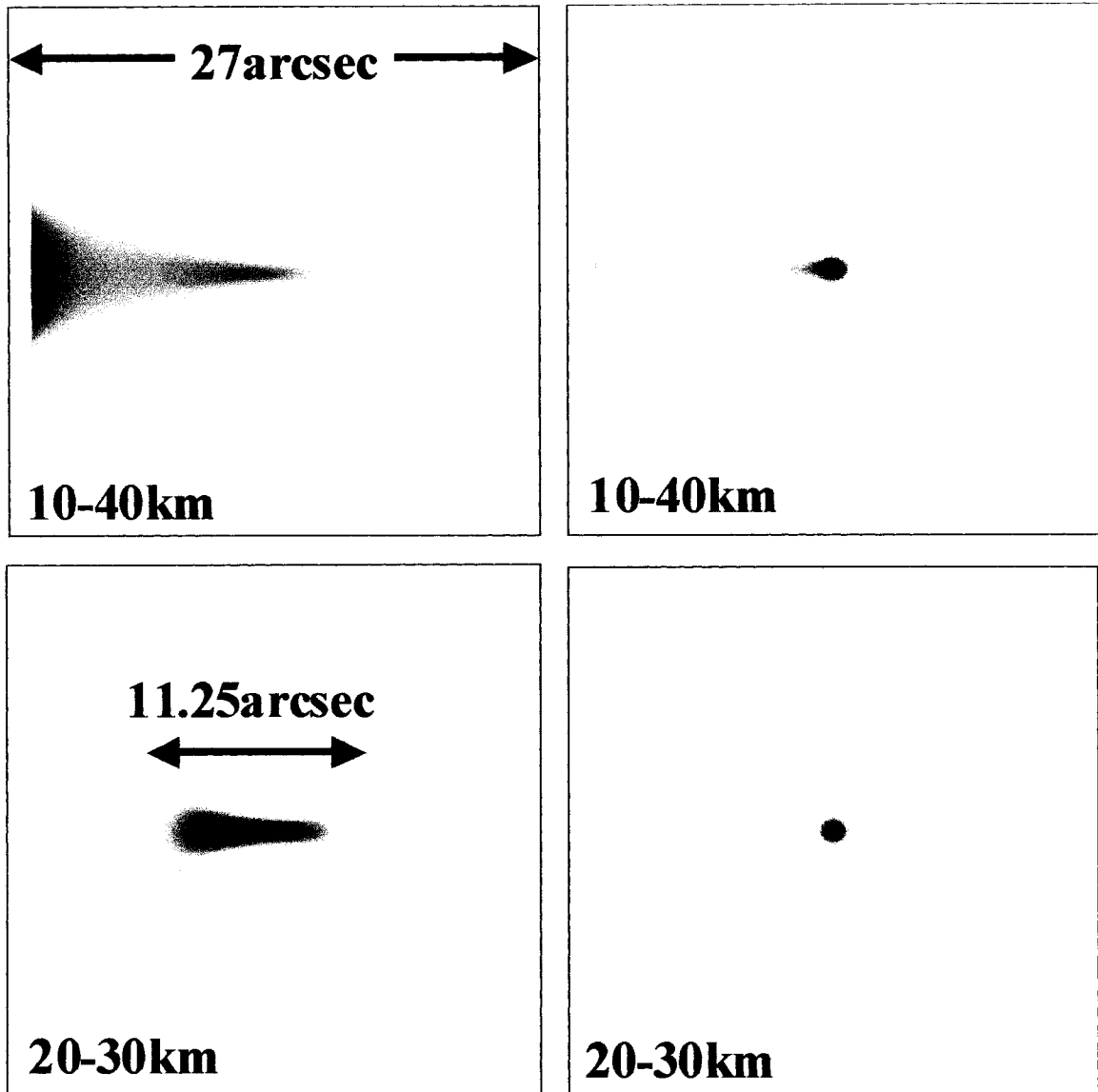


Figure 2.9 This figure shows the output of a model created using the principles set forth in this chapter. All images are for a 61" off-axis subaperture of the MMT and a 27arcsec field of view. The top left image shows light from 10-40km that is NOT dynamically refocused within the FOV. The top right shows the same case with DR. The bottom images are similar and show light from 20-30km. These images are individually scaled and are not indicative of the intensity change due to dynamic refocus.

CHAPTER 3 MMT DYNAMIC REFOCUS SYSTEM

This chapter will describe the details of the MMT DR system and its key components: the MMT DR optics, the aluminum rod resonator and the resonator driver.

3.1 INTRODUCTION

Chapter 1 outlined the current state of LGS's and concluded with the idea that dynamically refocused Rayleigh beacons could yield MCAO on the MMT within a tractable timetable. In chapter 2 paraxial and first order optics were used to develop a black box dynamic refocus system that included a mirror moving in sinusoidal motion. This chapter will carry the black box idea of dynamic refocus through to a completed design, optically, mechanically and electronically.

I hope to describe the components presented in this chapter in a manner that is an extension of chapter 2, to use first order principles to describe each component's feasibility, operation and design. It is my intention to present the topics discussed in this chapter not as work that I have done myself, but as components I utilized to accomplish the task of proving the MMT dynamic refocus system on the Mt. Bigelow 61" telescope

I do not claim ownership over any of the components presented in this chapter nor do I claim that I had any part in their development.

3.2 MMT DYNAMIC REFOCUS OPTICS

From chapter 1, it is known that multiple LGS's may be used to create a three dimensional tomographic solution of the atmosphere [Lloyd-Hart et al. 2001 & 2002]. Chapter 1 also introduced the concept of dynamically refocusing Rayleigh beacons for use as LGS's. In chapter 2, first order and paraxial principles were used to describe how a DR system might look and perform. Figure 2.4 lays out what a basic model for a dynamic refocus system may look like. Section 3.2 will further develop this basic model, eventually describing the MMT DR optical system design and its laboratory performance.

3.2.1 MMT DR SYSTEM REQUIREMENTS

The system requirements for MCAO on the MMT have been described by Lloyd-Hart [2001]. He has outlined that five Rayleigh beacons axially symmetric on a regular pentagon 120arcsecs in diameter dynamically refocused from 20 to 30km will produce the desired tomographic solution.

Further requirements are outline in sections 1.1.5 & 1.2.3 that included discussion of the size and intensity of the LGS image produced by a given SHWFS subaperture. It was noted that a smaller brighter spot yields better and faster AO correction. The DR optics, which will precede such an image on the SHWFS, must produce a small concentrated

dynamically refocused beacon image. The imaging requirement for the MMT DR system was that it produce a dynamically refocused image of the rising laser pulse with >80% encircled energy within $< \frac{1}{2}$ arcsec [Roger Angel: Personal Communication, 2003] over the geometric parameters outlined above. Another set of parameters that have been discussed but not formally defined are the effects of pupil aberrations due to the DR system.

Using the above requirements, the basic model set forth in chapter 2 will be extended in order to understand the MMT DR system design.

3.2.2 BASIC MODEL

The basic DR system model of chapter 2 is extended in figure 3.1. In this figure a rising laser pulse is shown at one of the points on the 120arcsec pentagon at a height of 25km. The MMT images this pulse to a conjugate plane that has a plate scale of 2.11 arcse/mm. The DR field lens is placed at this 25km conjugate plane and places a pupil near the entrance of the DR objective. The light passes through the DR objective, reflects off the DR mirror and passes back through the DR objective returning to a focus at the field lens/25km conjugate plane. The next few sections will use first order considerations to more fully develop each of these optical elements, resulting in the presentation of the MMT DR optical system design.

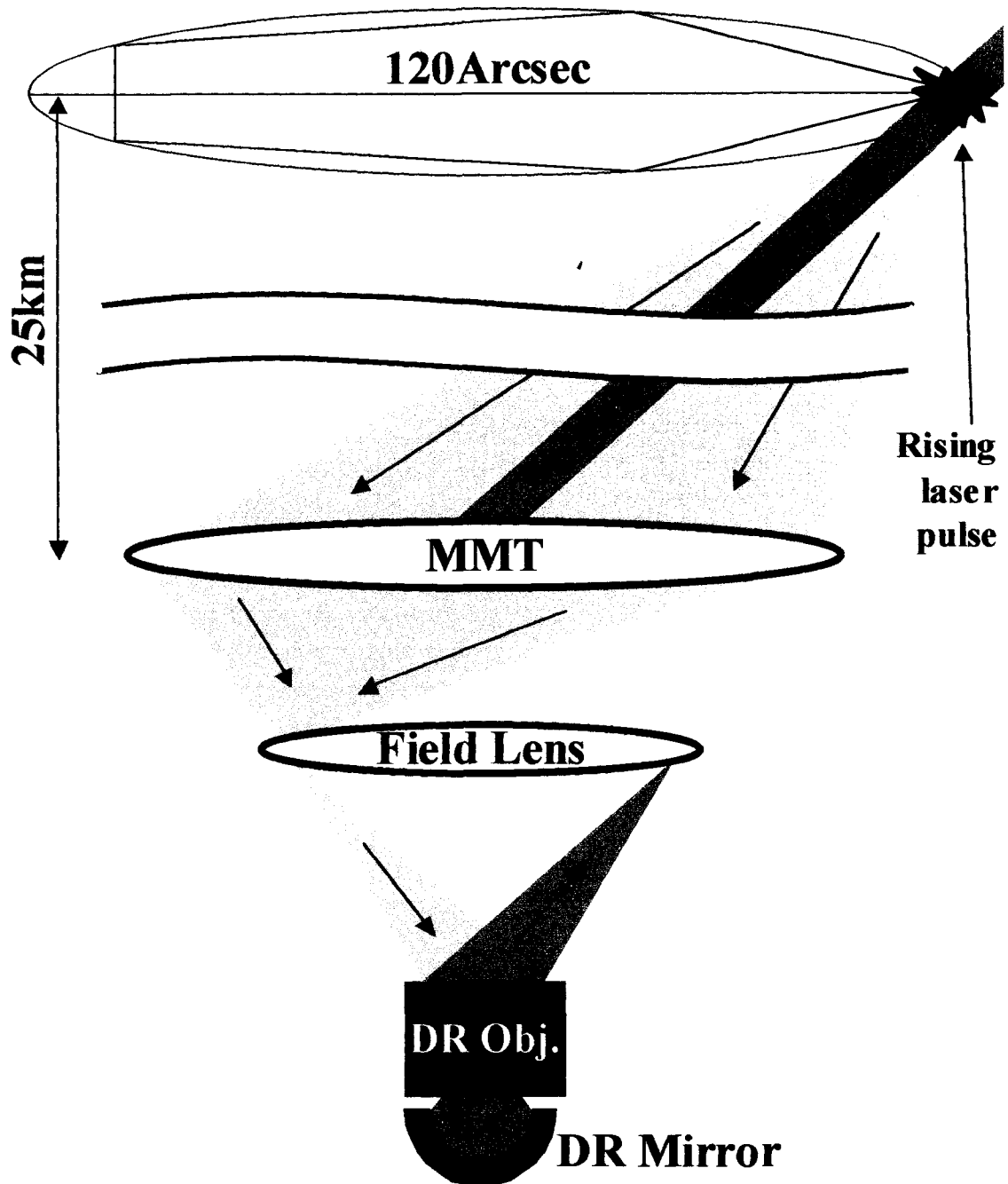


Figure 3.1 The basic layout of the MMT DR optical system is schematically shown in the above figure. A Rayleigh beacon produced by a beam projector behind the MMT's secondary sends laser pulses through the atmosphere. The beacons form a 120arcsc pentagon on the sky. The MMT DR field lens is conjugate to 25km.

3.2.2 FIELD LENS

The primary function of the DR field lens is to create a pupil near the entrance of the DR objective. The size of this pupil determines the diameter of the DR objective optics. It is assumed that the DR objective optics will almost certainly be custom optics, so to keep costs down, one wishes to keep their diameter's small. If one assumes 1 inch optics and 20mm clear aperture then the field lens must have a focal length of near 300mm (the pupil is in $f/15$ space and it can be assumed that the telescope pupil is effectively at infinity). The length of 300mm also keeps the optical system size small.

3.2.3 OBJECTIVE

The function of the objective is two-fold: to speed up the light to $f/0.6$ (as outlined in section 2.2.3) and to place a pupil at the DR mirror. It is essential that the DR mirror be at a pupil so that $150\mu\text{m}$ movement does not cause noticeable displacement of the image.

The two functions of the objective may be accomplished through the use of two optical elements, a magnifying lens at the pupil that changes the $f/\#$ and a field lens that re-images the pupil onto the moving mirror (figure 3.2). The objective magnifying lens has an approximate focal length of 12mm, which gives the field lens (a $4f$ or $1:1$ imager) a 6mm focal length.

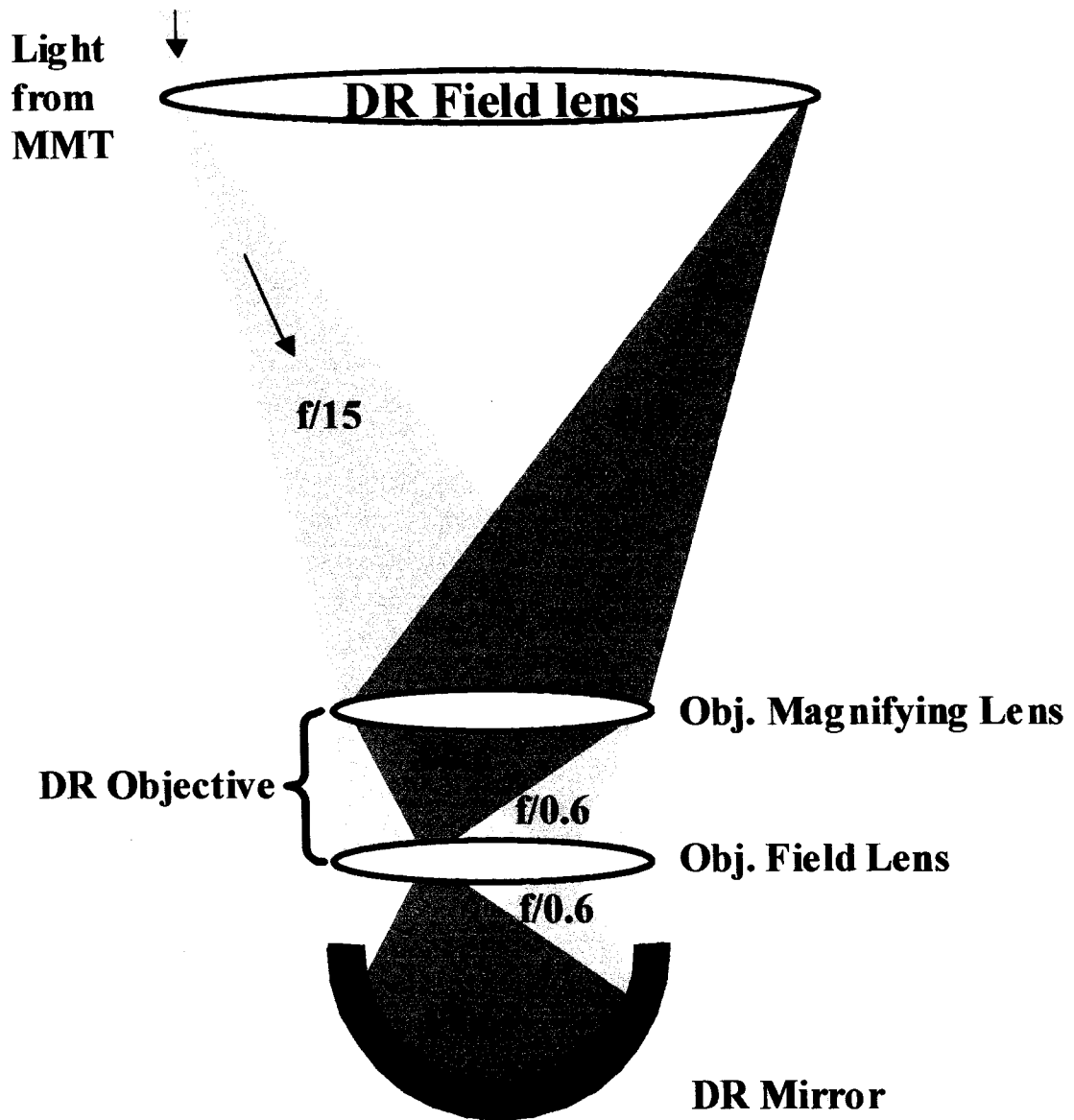


Figure 3.2 The MMT DR optics are schematically shown above. The DR field lens places a pupil near the entrance of the DR objective which shown as two optical elements. The first element, the magnifying lens changes the $f/\#$ of the MMT light. The second element is a field lens that places a pupil image at the DR mirror.

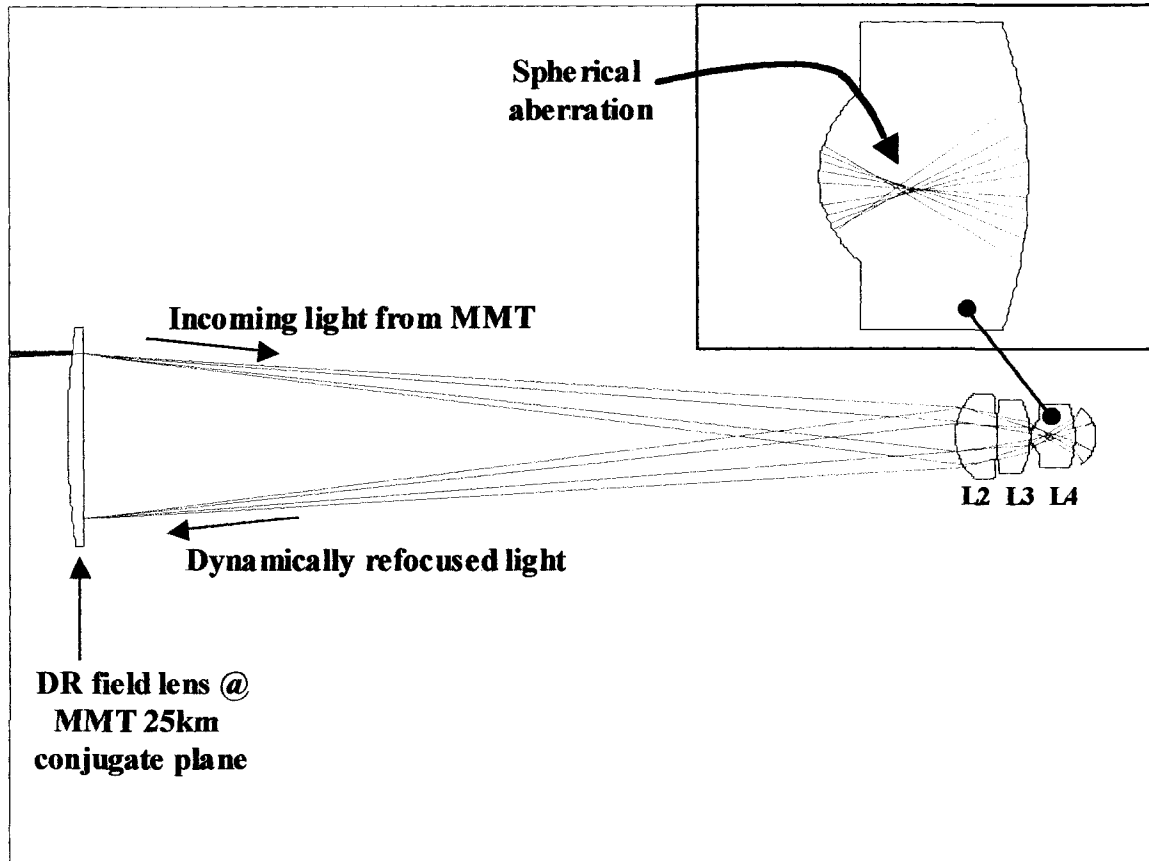
3.2.4 ABERRATIONS

If the MMT, DR field lens and two objective lenses were perfect and introduced no aberrations, the DR mirror would introduce a large amount of astigmatism and Petzval curvature [Shack, 2001]. The Petzval curvature is of less concern because the system operates only on one zonal field. The astigmatism is of more concern because it will greatly degrade the image produced by the DR optics. Therefore, in the design of the DR objective the optics must include an opposite amount of astigmatism to balance the mirror.

The DR mirror's location gives the DR system symmetry about a pupil, which cancels out odd third order aberrations in any optical system. Chromatic affects are ignored for this design, because the Rayleigh beacon is only operated at the doubled Nd:YAG wavelength, 532nm. This leaves spherical aberration as the remaining third order aberration left to consider. The control of this aberration may be understood after the system is presented.

3.2.5 MMT DR OPTICAL SYSTEM

The MMT DR system designed by Roland Sarlot, along with its prescription is shown in figure 3.3. The wave aberrations attributed to each surface calculated by Zemax are shown in table 3.1.



Surface	Comment	Radius of Curvature [mm]	Thickness [mm]	Glass	Semi-Diameter [mm]	Conic
0		Infinity	2500000.00		7275.70	
1		Infinity	12000.00		0.00	
2	MMT PRIMARY	-16255.25	-7307.08	MIRROR	3251.00	-1.00
3	SECONDARY	-1794.60	7307.08	MIRROR	332.56	-1.41
4		Infinity	2288.00		109.49	
5	INFI CASS FOCUS	Infinity	374.04		40.00	
6	25KM CASS FOCUS	226.62	5.62	SF6	37.99	
7		3236.98	300.00		37.99	
8	L2-SA CORRECT	20.16	14.43	SF6	14.99	
9		-97.96	0.30		14.99	
10	L3	515.25	11.05	SF6	12.99	
11		-28.70	0.30		12.99	
12	L4	7.57	14.98	SF6	6.00	
13		-32.97	7.33		10.98	
14	MOVEABLE MIRROR	-12.02	-7.33	MIRROR	9.84	
15	L4	-32.97	-14.98	SF6	10.98	
16		7.57	-0.30		6.00	
17	L3	-28.70	-11.05	SF6	12.99	
18		515.25	-0.30		12.99	
19	L2-SA CORRECT	-97.96	-14.43	SF6	14.99	
20		20.16	-300.00		14.99	
21		Infinity	0.00		28.44	

Figure 3.3 The Design of the MMT DR optical system and its prescription is shown above. The spherical aberration present of the image formed in L4 is shown in the inset at the top of the figure.

Surface	Zemax Code	W040	W131	W222	W220	W311
Object	1	0.00	0.00	0.00	0.00	0.00
Primary	STO	-15.88	-71.06	0.10	-0.05	0.00
Secondary	3	15.83	70.98	-0.02	0.47	0.00
Dummy	4	0.00	0.00	0.00	0.00	0.00
Dummy	5	0.00	0.00	0.00	0.00	0.00
DR Field Lens 1st surf	6	0.00	0.00	0.00	0.83	-6.51
DR Field Lens 2nd surf	7	0.00	-0.01	-0.02	-0.06	-0.34
L2 1st surf	8	96.48	55.51	7.98	9.36	3.84
L2 2nd surf	9	133.53	-103.78	20.17	1.93	-4.67
L3 1st surf	10	-84.30	83.97	-20.91	0.37	5.03
L3 2nd surf	11	215.31	-34.79	1.41	6.58	-0.59
L4 1st surf	12	-0.15	5.49	-50.19	24.94	2.80
L4 2nd surf	13	-347.01	-174.30	-21.89	5.73	-1.31
DR Mirror	14	0.02	3.00	139.78	-69.93	-3.85
L4 2nd surf	15	-343.48	211.51	-32.56	5.73	3.25
L4 1st surf	16	-0.29	-7.62	-49.85	24.94	0.17
L3 2nd surf	17	213.83	10.97	0.14	6.58	0.17
L3 1st surf	18	-86.51	-75.84	-16.62	0.37	-3.48
L2 2nd surf	19	136.31	90.18	14.91	1.93	3.10
L2 1st surf	20	93.50	-64.50	11.12	9.36	-5.15
DR Field Lens 2nd surf	IMA	0.00	0.00	0.00	0.00	0.00
	TOT	27.17	-0.27	3.56	29.06	-7.53

Table 3.1 The third order aberration coefficients attributed to the Zemax modeled surfaces of the MMT DR system. The astigmatism due to the DR mirror is highlighted as well as the spherical aberration due to the second surface of L4.

In table 3.1 the astigmatism, W_{222} coefficient, caused by the DR mirror is shown in bold.

It is seen that the first surface of L3 and L4 as well as the second surface of L4 add significant amounts of negative astigmatism to counteract the effect of the mirror.

Figure 3.3 shows the large amount of spherical aberration in the image formed within L4.

This is a result of the aberrations acquired at all the prior surfaces in the objective. It is

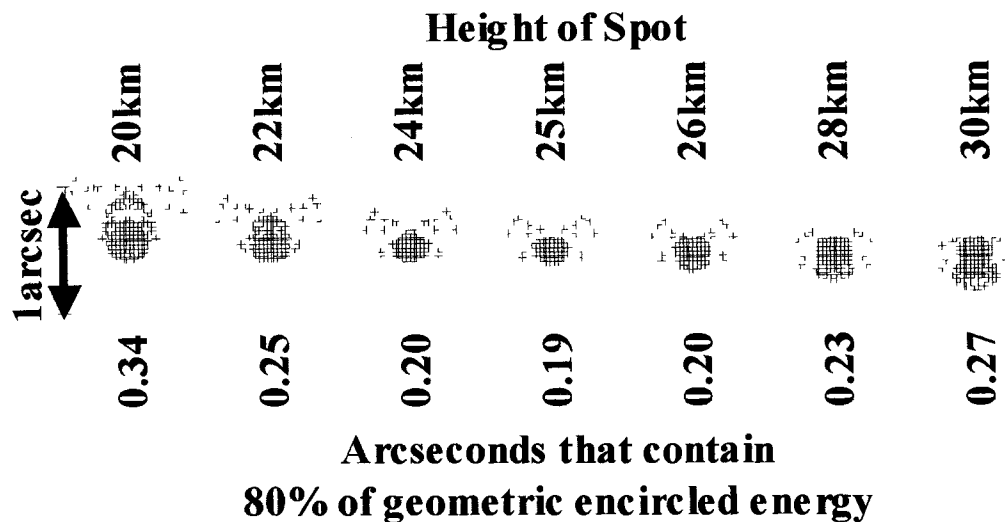
interesting to note in table 3.1, the large amount of negative spherical aberration present on the second surface of L4 that cancels nearly all of this affect.

The combination of L2 and L3 may be thought of as the objective magnifying lens presented in figure 3.2 and L4 may be thought of as the field lens. Spherical aberration is quartically dependant on marginal ray height, so any deviation of a marginal ray height from nominal would produce dramatic results in a system with a large amount of spherical; for example the second surface of L4. One could change the marginal ray height on this surface by adjusting the power of the L2-L3, magnifying lens combination. This adjustment may be accomplished by adjusting the spacing between these two lenses, making this spacing adjustment a spherical aberration tuner.

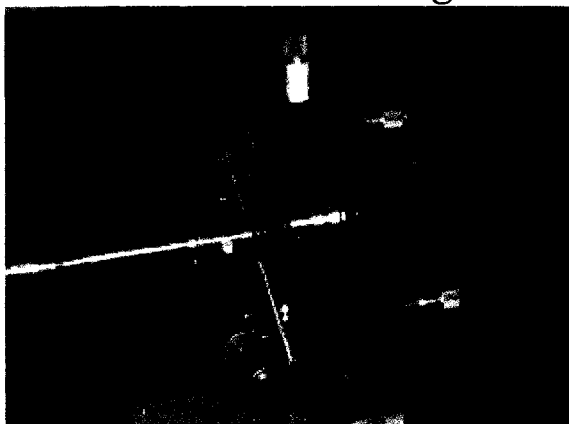
The performance of the system is shown as a series of spot diagrams in figure 3.4. The system requirements were stated in terms of encircled energy, so the spot diagrams are related to the geometric encircled energy in this figure.

3.2.6 FABRICATED SYSTEM

Brad Piccirillo of Optical Systems Inc. in Charleston New Hampshire built the system shown in figure 3.3. The tight tolerances required a well designed and built mechanical cell to hold the elements of the DR objective. Along with the physical mounting requirements it was thought that the cell might become a window for an evacuated box.



**Rear view of objective cell in
its tip/tilt mount,
DR mirror and ringer**



**Front view of objective cell in
its tip/tilt mount,
DR mirror and ringer**



Figure 3.4 The performance of the MMT DR optical system shown in figure 3.3 is shown above as a series of spot diagrams. The geometric encircled energy of the spots are also stated. The images in the lower part of the figure show the MMT DR objective mounted in its cell.

that would hold the resonator. The vacuum box would eliminate any damping due to the air between the DR mirror and the cell. It would also eliminate the (very loud) sound of the running resonator.

A stainless steel cell was designed by Brian Cuerden and built by the Steward Observatory machine shop (shown in figure 3.4 and diagrammed in figure 3.5). Stainless steel was chosen because it matched the thermal expansion coefficient of the SF6 glass of the DR objective lenses. The cell was designed so that a spacer ring determines the distance between L3 and L4. L2 is held in its own cell that mates with the main cell. This allows the distance between L2 and L3 to be changed by positioning L2's cell with three push and three pull bolts. The pull bolts anchor L2's cell to the main cell and the push bolts are set screws that literally push the two cells apart. The adjustment of these bolts serves as a spherical aberration tuner.

The cell also has three nylon tipped set screws per lens that may be used to center the lenses. It has not yet been necessary to utilize these features.

3.2.6.1 ALIGNMENT

This section will describe how the lens cell is aligned and tested.

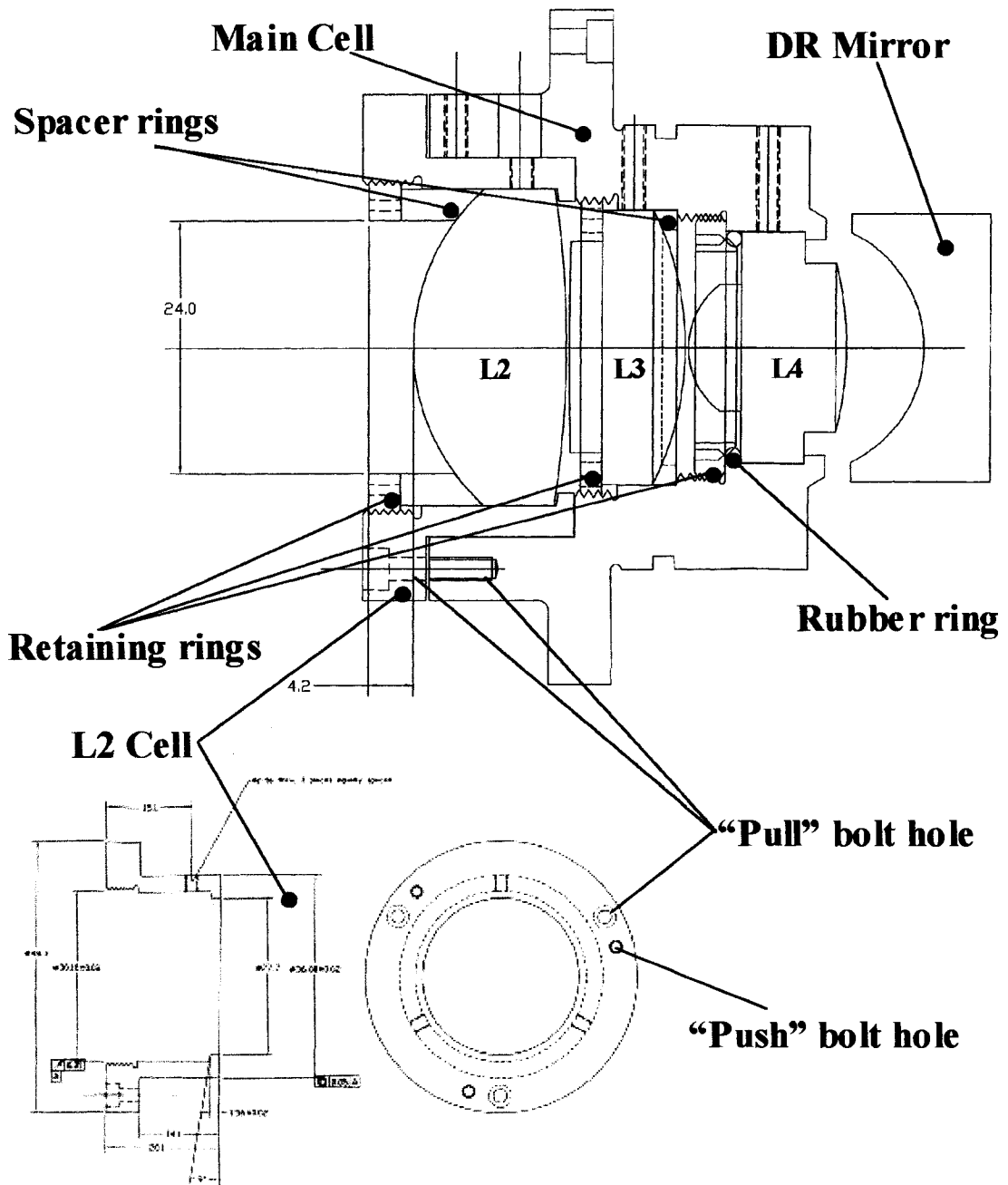


Figure 3.5 Brian Ceurden's design for the stainless steel cell that supports the MMT DR objective optics.

First, three small strips of Teflon tape are applied at 120degree intervals on the metal surfaces that interface with the glass. L4 is set into place, a rubber ring is placed above the lens and its retaining ring is screwed into place holding the rubber ring against the lens and the lens firmly in place in the cell.

A brass spacer ring is then placed in the system and L3 is placed on top of it. A retaining ring is engaged to hold L3 firmly in place.

L2 is placed in its own cell with a spacer ring on top of it; a retaining ring holds these firmly in place. The L2 cell is placed in the main cell. This is done carefully because when the push bolts of the L2 cell are not extended, surface 2 of L2 touches surface 1 of L3. Each push bolt is slowly turned until the L2 is barely seen to lift. When all push bolts are in this position, they are each extended an 1/8th turn more to insure the glass surfaces are not touching.

The lens cell is placed into an optical set up is aligned so the objective cell, DR mirror and laser optics are all on axis in a manner similar to that described in section 4.3.3.4. After the system is aligned on-axis, the laser assembly is rotated to its off axis position shown in figure 3.6. Collimated light is passed through an infinity corrected microscope objective that focuses the light through a 5 μ m pinhole. The pinhole is 300mm from the

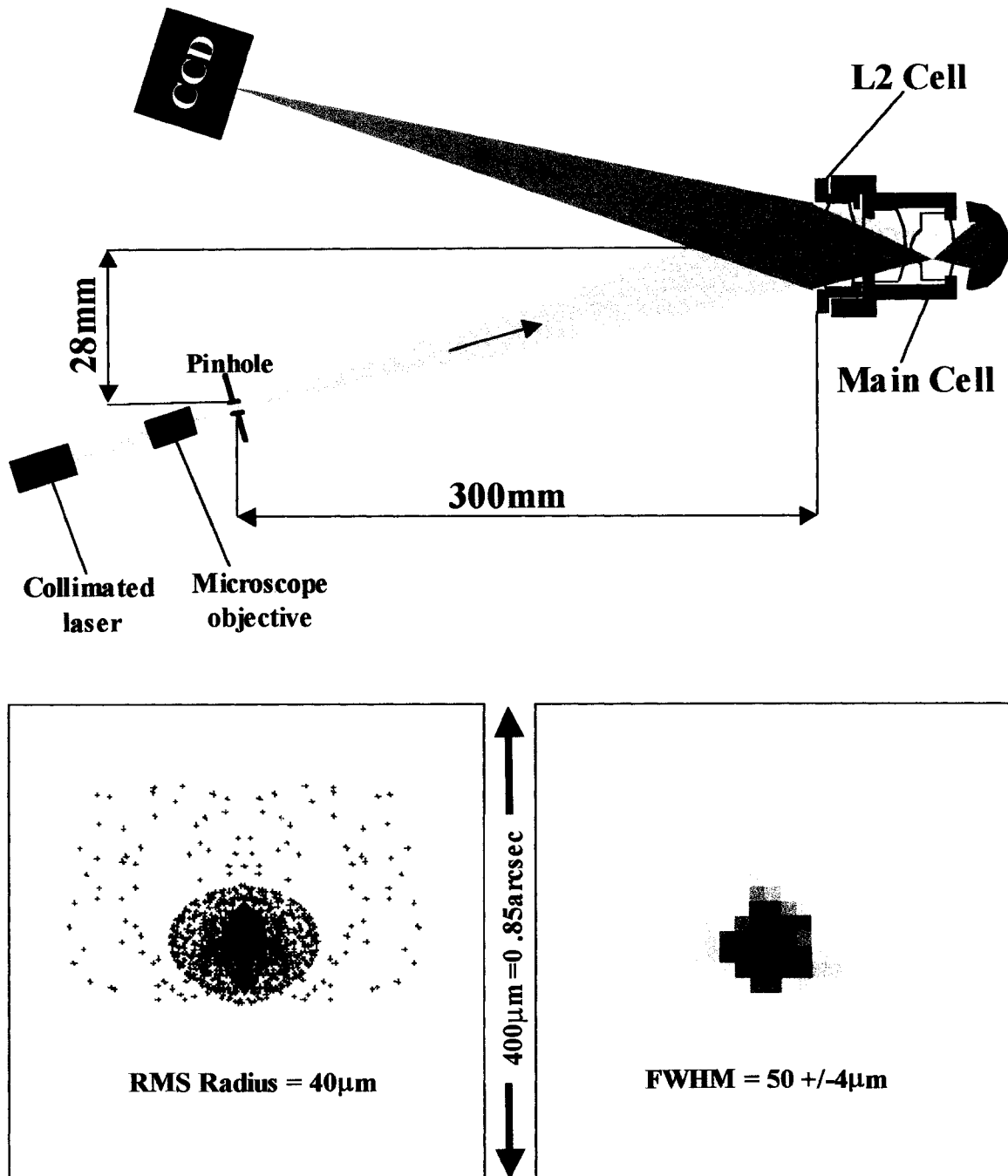


Figure 3.6 The layout for optically testing the MMT DR objective and cell is diagrammed above. The results of the test are also shown in the lower part of the figure.

first surface of L2 and approximately 28.44mm from the optical axis in order to mimic the 25km beacon image shown in figures 4.1, 4.2, and 4.3.

The axial position of the DR mirror is used to focus the image on the CCD. Residual coma in the image is eliminated by translating the DR objective cell in x and y. With no adjustment of the DR L2 cell, the image will display a significant amount of spherical aberration. Taking the DR mirror in and out of focus and viewing the images on the CCD, the sign of the SA is found by noting the soft and hard side of focus. The L2 lens cell is moved coarsely by hand away from the main cell. The sign of SA is checked so that it is opposite from the initial position. If it is opposite, this test indicates that when the L2 cell is pressed against the main cell, with the current position of the push bolts, L2 is too close to L3. This is the desired condition, because it is known that L2 and L3 are barely separated and decreasing the separation between them would be difficult.

With the case that the sign of SA was opposite than the original position, the push bolts are each extended a $1/8^{\text{th}}$ turn (moving the L2 cell away from the main cell) and the pull bolts are firmly tightened. This operation is iteratively repeated until the image falling on the CCD is minimum. At every iteration, the pull bolts are tightened as if the cell were to be operational so that in the case that the image is at the minimum size, no further adjustments are necessary.

3.2.6.2 TEST RESULTS

The results of the DR objective cell alignment are shown in figure 3.6. The test image was taken with StellCam Ex CCD camera. This camera exports an analog signal that is digitized by a National Instrument's image acquisition card. This leads to inherent spatial uncertainties; it is assumed that the pixels in the image are $13 \pm 1 \mu\text{m}$. Including these spatial uncertainties, the test image is very similar to the expected spot diagram, which is shown at the same scale in the figure.

Two things should be noted here. The first is that the lens cell cannot be aligned in the gimbal mount in which it used on the mountain (shown in figure 3.4) because there exists no access to the push/pull bolts. It was aligned in the lab using the xyz translation stage shown in figure 3.4, but with a (New Focus) claw mount to control tip/tilt. Second, the alignment of the DR objective described above was done on the optical table at the Steward Observatory lab and the DR objective was shipped to the mountain as a single unit. Even though the push/pull bolts were firmly clamped after every SA iteration, it was noted that something came loose on one passage. This resulted in poor imaging and the loss of one telescope run. The misalignment of the DR cell was only noticed while aligning for the last telescope run I was involved in. The extremely poor imaging was observed as a large amount of coma when aligned as described in section 4.3.3.4, the parent SA was seen when it was placed back in the set up shown in figure 3.6. Upon noting the poor imaging while aligning on the mountain, the cell was taken back to the lab and realigned.

In summary, section 3.2 described the design, alignment and performance of the MMT DR optical system presented in black box form in the last chapter. The dynamic part of dynamic refocus was outlined in chapter 2 as axial, sinusoidal motion of the DR mirror. The mechanical device that accomplishes such a motion will be described in the next section.

3.3 RESONATOR

This section will serve to introduce the mechanical device that moves the DR mirror as prescribed in figure 2.5. It is beyond the scope of this chapter and this dissertation to fully describe this device. It is my intention to give a description that highlights the feasibility of such an instrument. I hope this chapter answers the question: “I have to move a mirror 150 μ m peak to peak at 5kHz, what can accomplish such a task?”.

3.3.1 DAMPED DRIVEN SIMPLE HARMONIC MOTION

As with any sinusoidally moving system, it is instructive to review of the effects of simple harmonic motion of a mass on a massless spring. The basic equation that describes such a motion is Hooke’s law

$$F = -kx \tag{3.1}$$

where F is the force required to cause a linear displacement, x , of a system with a spring constant k . The above equation may be extended to the case of a damped driven oscillator,

$$m\ddot{x} + c\dot{x} + kx = F_o \cos(\omega t) \quad (3.2)$$

where m represents a mass on a spring, c is a damping constant, ω is the angular driving frequency and F_o is the magnitude of a cosinusoidal driving force. Such a system will undergo resonance if it is driven near the natural frequency, ω_o , of the spring system

$$\omega_o = \sqrt{\frac{k}{m}}. \quad (3.3)$$

The maximum half amplitude of a system with low damping is given as [Fowles and Cassiday, 1997]

$$A_{\max} = \frac{F_o}{c\omega_o}. \quad (3.4)$$

The quality factor, Q , of an oscillator is proportional to the energy stored in the system divided by the energy lost in a single period of oscillation. Therefore, a system with high Q loses very little energy in a period. Intuitively the Q is inversely related to the damping in the system and may be defined as [Fowles and Cassiday, 1997]

$$Q = \frac{\omega_o m}{c}. \quad (3.5)$$

Combining equations (3.4) and (3.5) gives,

$$A_{\max} = \frac{F_o Q}{\omega_o^2 m}, \quad (3.6)$$

the maximum amplitude of an oscillator in resonance as a function of the Q of the system. Using the ideas developed above, the next section will develop a suitable resonant system for the MMT DR system.

3.3.2 MOTION OF AN ALUMINUM ROD

For the case of DR, the mirror needs to be moved in the axial direction. It is difficult to conceive of a spring moving a mirror with optical precision with only one degree of

freedom. However, it is not difficult to conceive of a rigid object in resonance, a bell, a chime or a tuning fork. If the desired motion is purely axial, one could imagine a cylindrical rod resonating in pure piston motion.

The Young's modulus [Serway, 1990],

$$Y = \frac{F/A}{\Delta L/L_0}, \quad (3.7)$$

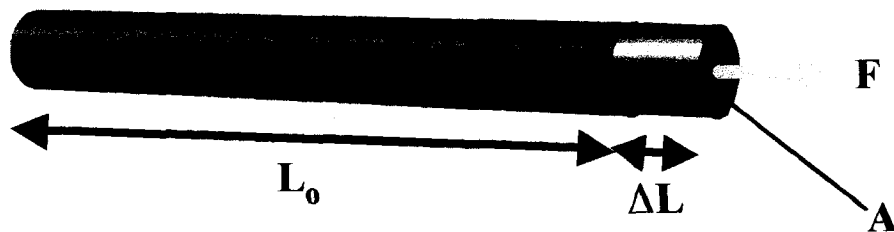
of an elastic material is defined through the amount the material is stretched (or compressed), ΔL , under a given force, F , where L_0 is the original length of the material and A is the cross-sectional area (figure 3.7). The above equation can be solved for F

$$F = \left(\frac{YA}{L_0}\right)\Delta L \quad (3.8)$$

which is similar to equation (3.1) with ΔL analogous to x and an effective spring constant,

$$k_{eff} = \frac{YA}{L_0}. \quad (3.9)$$

Young's modulus



Wire coil in a radial magnetic field

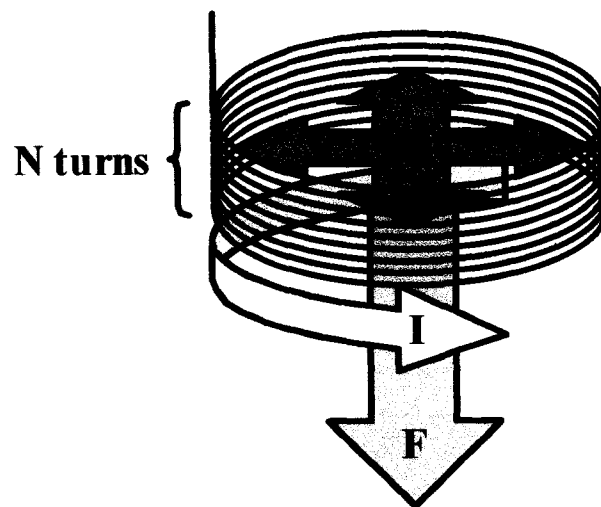


Figure 3.7 The explanation of equations (3.7) and (3.17) are diagrammed above. In the above image a rod of nominal length L_0 (dark gray) is shown stretched (light gray) by an amount ΔL to illustrate Young's modulus. In the lower figure, the force, F , due to a radial magnetic field, B , on a wire coil that has a current, I , flowing through it is shown.

By equation (3.3) an effective mass,

$$m_{\text{eff}} = \frac{k_{\text{eff}}}{\omega_o^2} = \frac{YA/L_o}{\omega_o^2}, \quad (3.10)$$

could be defined where the resonant frequency of the rod is simply

$$f_o = \frac{\omega_o}{2\pi}. \quad (3.11)$$

To find the resonant frequency, the speed of sound in the rod is calculated [Serway, 1990],

$$v = \sqrt{\frac{Y}{\rho}} \quad (3.12)$$

where ρ is the density of the material. If the rod is held at its center, then the fundamental wavelength of the sound within the rod is equal to the length of the rod, L_o . The resonant frequency of the rod is then

$$f_o = \frac{v}{L_o} \quad (3.13)$$

For the case of a 1m aluminum rod with the values [Serway, 1990] $Y=7*10^{10}$ [N/m²] and $\rho=2.7*10^3$ [kg/m³], the resonant frequency of the rod is 5.1kHz.

Combining equations (3.6) and (3.10) gives

$$A_{\max} = \frac{F_o Q L_o}{Y A} \quad (3.14)$$

the maximum amplitude of the rod as a function of the Young's modulus. This equation is then solved for the required driving force

$$F_o = \frac{A_{\max} Y A}{Q L_o} \quad (3.15)$$

Order of magnitude assumptions of the values in the above equation can be made:

$A_{\max}=75\mu\text{m}$ (half amplitude of sinusoid in figure 2.6), $Y=7*10^{10}$ N/m² [Serway,1990],

$A=507*10^{-6}\text{m}^2$ (1inch diameter rod), $Q=3,000$ (the Q of a piano string [Fowles and

Cassiday, 1997]), $L_0=1\text{m}$ (gives 5.1kHz resonant frequency). This yields sinusoidal driving force magnitude of $F_0=0.9\text{N}$ (approximately 0.25lbs) at the 5.1kHz resonant frequency. The next section explores what may yield such a force

3.3.3 RESONATOR DRIVER

One may continue looking to the musical world for inspiration and think of a loudspeaker as a driver. In a loudspeaker, a voice-coil is attached to a speaker cone. The coil is placed in the field of a permanent magnet. Current applied to the coil results in a force that moves the coil in and out. The movement of the coil/cone system pushes the air causing pressure waves or sound.

The force on a wire carrying current is given by

$$\vec{F} = I\vec{\lambda} \times \vec{B} \quad (3.16)$$

where I is the current passing through a length of wire, λ , that is within a magnetic field B . If the magnetic field can be made purely radial (figure 3.7) then the magnitude of the force on a coil of wire with N turns and a diameter D is

$$F = IN\pi DB \quad (3.17)$$

Making another order of magnitude calculation: $I=1\text{A}$, $N=100$, $D=0.075\text{m}$, $B=1.0\text{T}$ (the flux of a JBL 2012H Speaker) gives a force of 7.5N , more than the 0.9N required for driving the aluminum rod.

These order of magnitude calculations only show the feasibility of driving a 1m aluminum rod with a voice coil type driver. The actual MMT DR resonator/driver system presented in the next section is much more complicated than outlined in this section. A full description of these components is, as stated, beyond the scope of this dissertation.

3.3.4 MMT DR RESONATOR AND DRIVER

The MMT DR resonator and driver system is shown in figure 3.8. High quality permanent disk magnets are the source for the magnetic field. A wound copper ribbon coil is permanently and securely fastened to the pole piece. The iron pole piece guides the magnetic field so that it is nearly parallel as it passes through the resonator nearest the coil.

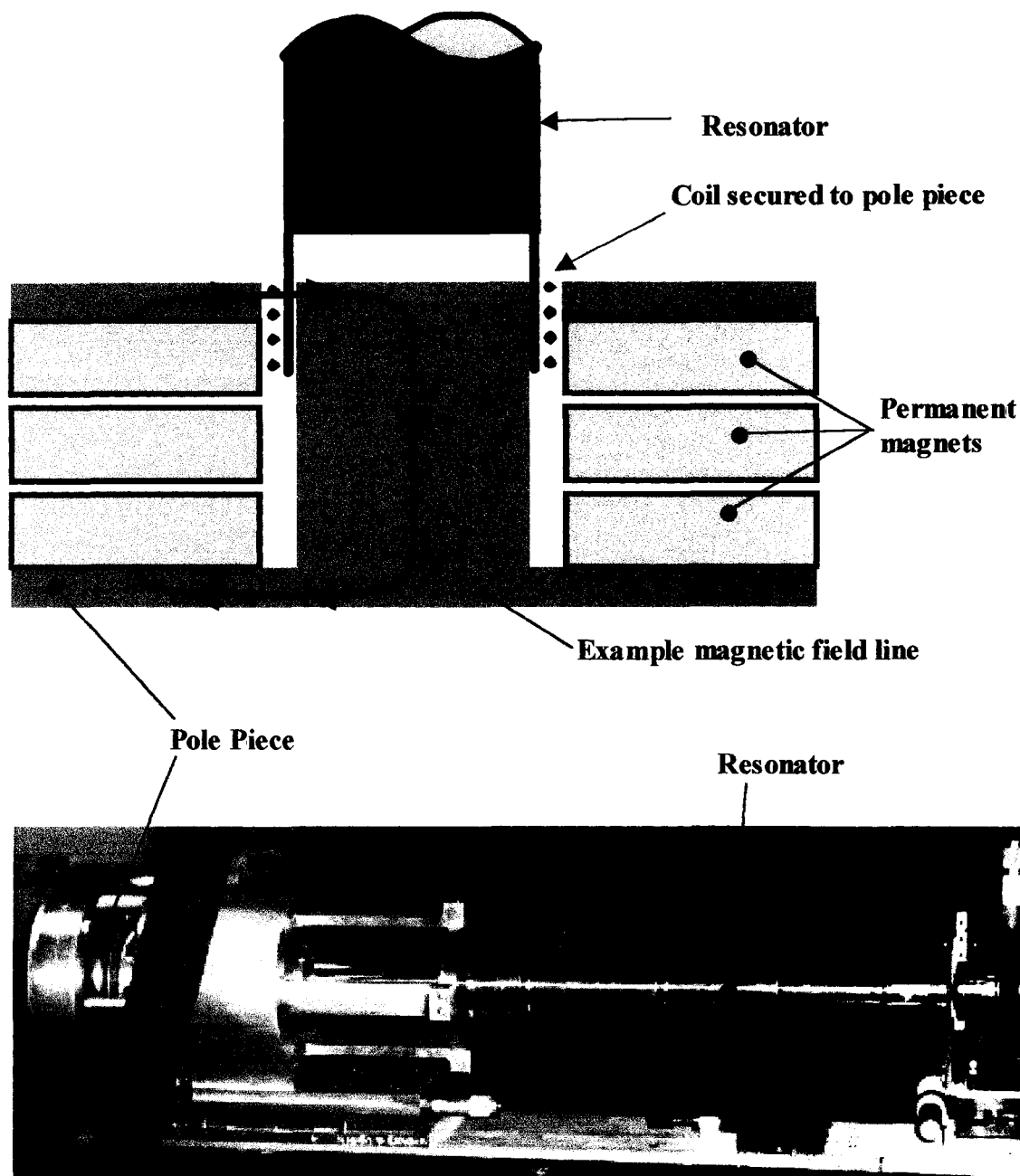


Figure 3.8 A cross-sectional slice of the MMT DR resonator driver is shown in the top image of the above figure. Permanent magnets are held in a pole piece that delivers a nearly parallel magnetic field through the resonator and coil. The actual resonator and driver system is shown in the image at the bottom of the figure.

When current flows through the coil, it creates a magnetic field that induces an eddy current in the resonator that opposes the current present in the coil. This eddy current is what is acted upon by the magnetic field creating the force described in equation (3.17).

A system similar to MMT DR system was tested for lifetime and Q. Some of the results of these tests are shown in figure 3.9. A measurement of Q can be measured using

$$Q = \frac{\Delta f}{f_{center}} \quad (3.18)$$

where Δf is the half power bandwidth. The Q measurements were made using the amplitude of the resonator, which is related to the square root of the real power. The results in figure 3.9 use the $2^{-1/2}$ amplitude bandwidth that corresponds to the $1/2$ power bandwidth. The half power Q is also plotted as a function of time in order to determine lifetime characteristics of the resonator. It is noted that the Q changes as the resonator heats up, but no significant overall change was noticed over 60hrs of testing.

The MMT DR resonator and driver are shown in the bottom of figure 3.8. The resonator is firmly held to the driver. The driver is placed on a linear translation stage to allow focus of the DR mirror.

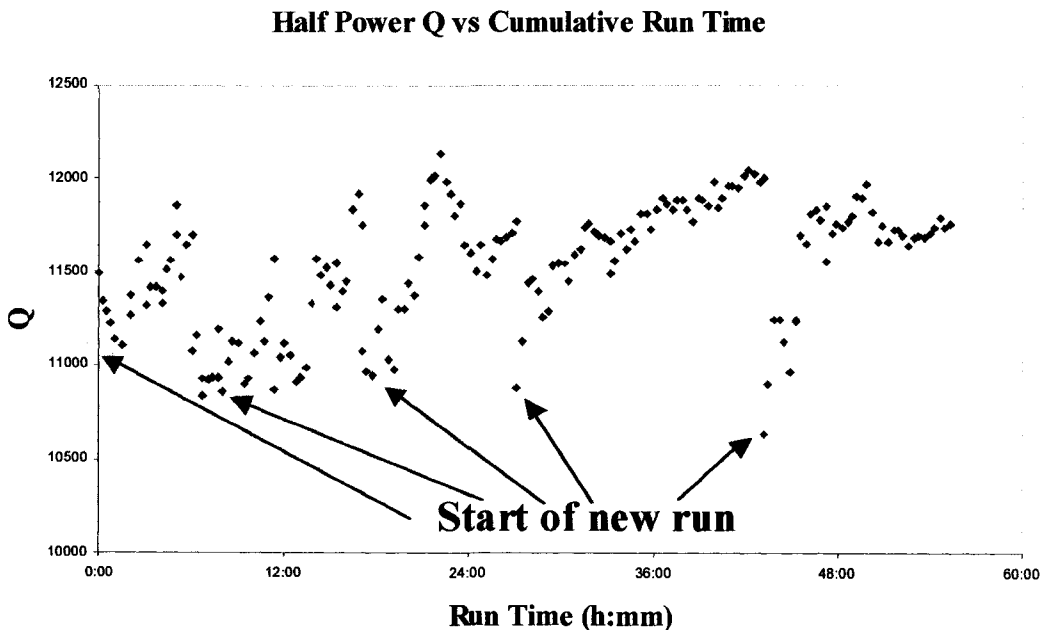
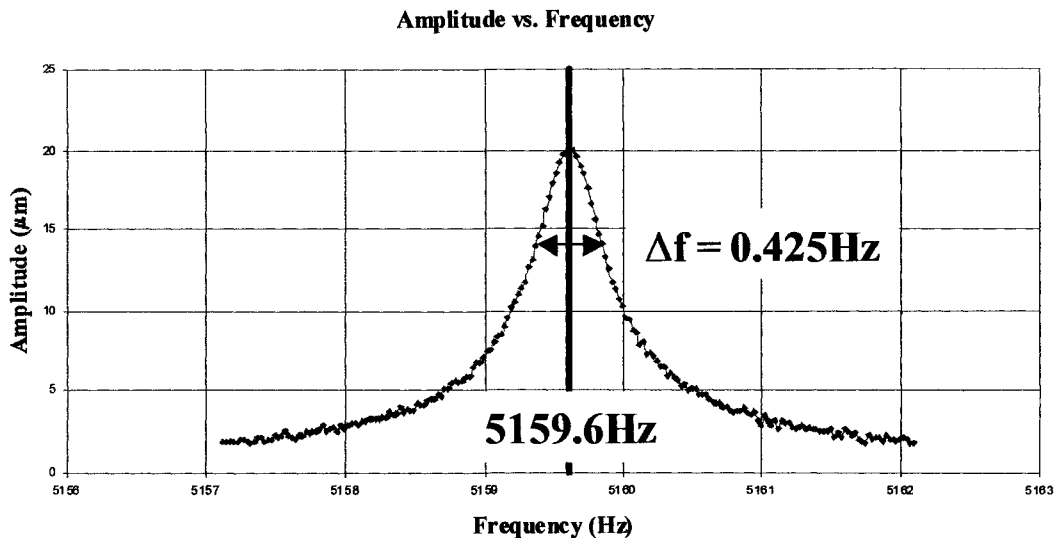


Figure 3.9 Test results of an earlier version of the MMT DR resonator/driver are shown above. The top graph shows the amplitude of the resonator as the frequency is changed. This allows a measurement of Q (equation(3.18)). The lower graph shows the Q of the resonator over nearly 60 hours of testing. The Q changes as the resonator warms up, but on average remains equal over the length of test.

CHAPTER 4 MT. BIGELOW FIELD-TESTS

This chapter will describe the Mt. Bigelow 61” field-tests, the equipment used, the overall system design, testing and performance.

4.1 INTRODUCTION

This chapter will go through, in detail, the heart and soul of this dissertation, the proving of the MMT dynamic refocus system on the 61” telescope. The chapter will begin with a discussion of the overall system architecture. Each major component will then be discussed using the format: design philosophy, design and expected results, component alignment and then component contribution to total system error.

The components to be discussed are the following.

- The 61” to MMT converter, which optically makes the light from the 61” telescope appear as if it is coming from a 61” off-axis subaperture of the MMT.
- The test-bed that investigates the light in “MMT-space”.
- The beam projector, which projects five Rayleigh beacons.
- The control electronics, which oversees the timing of the mechanical resonator with respect to laser firing and gated camera.
- The gated camera, which range-gates the image of the Rayleigh beacon.

At the end of the chapter, a summary of component errors will be presented.

4.2 SYSTEM ARCHITECTURE

The overall system architecture is shown schematically in figure 4.1. Light paths are represented by thin black lines and electronic signals are represented by thick gray dashed lines. Light is collected by the 61" telescope, it is then passed through the 61" to MMT converter. When the light leaves this converter box it acts exactly as if it were coming from a 61" off-axis subaperture on the MMT. From the converter box the light enters the MMT dynamic refocus optics presented in chapter 3. F/0.6 light exits these optics and hits the f/0.6 mirror that is epoxyed to the mechanical resonator. The light is reflected by the mirror, undergoes a parity change and is sent back through the DR optics. The light then enters de-magnifying optics on the MMT test-bed (not shown) and finally the gated camera.

The mechanical oscillator, the ringer, not only moves the mirror in sinusoidal piston motion, but also acts as a master clock. An optical distance-measuring device picks up the amplitude and time dependant resonant frequency of the ringer; and feeds these signals back to the CPU. The CPU employs a software phase-locked-loop (PLL), which continually updates the driving signal sent to the ringer. To accomplish this, the driving frequency from the software PLL is fed to a function generator, which is then amplified

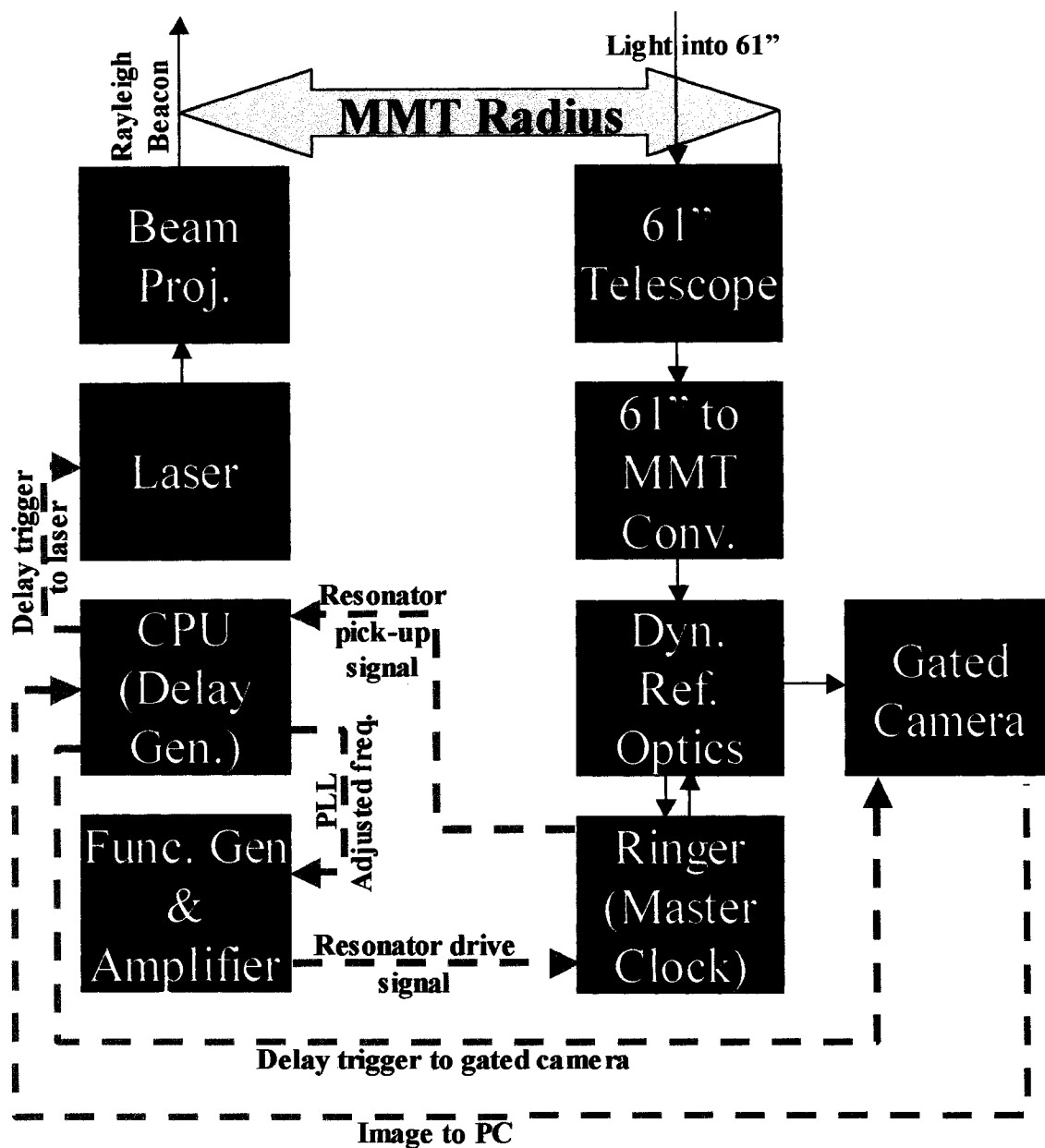


Figure 4.1 The 61" DR experiment is schematically outlined. Optical paths are indicated by thin black lines and electrical paths are indicated by thick gray dashed lines.

by an audio amplifier (not shown) and drives the resonator voice coil (not shown) keeping the ringer at resonance.

The CPU also performs the duty of a delay generator as well as a PLL. Delayed TTL pulses are sent to the laser so that it may be triggered with the correct phase delay (see discussion below equation (2.13)). The laser is optically fed into a beam projector, which has its optical axis located approximately an MMT radius from the edge of the 61". Delayed TTL pulses are also sent the gated-camera so that it may open its shutter when the laser pulse is rising between 20-30km.

These components will be discussed individually in the following sections.

4.3 61" TO MMT CONVERTER

As previously stated, the DR optics created are for use on the MMT. The concept of using an off-axis subaperture and its results were outlined in section 2.4, where it was shown that DR on an off-axis subaperture will produce a dramatic result, namely a long bowtie dynamically refocused to a spot limited by seeing. This section will highlight how a completely different telescope (the 61" on Mt. Bigelow) may be configured to act as an off-axis subaperture of the MMT (on Mt. Hopkins).

4.3.1 DESIGN PHILOSOPHY

The basic design philosophy for the converter box is shown in figure 4.2. The 61" is an $f/13.5$ system with a plate scale of 0.1 mm/arcsec (10arcsec/mm). A 61" MMT subaperture would produce an $f/63$ beam and have the MMT plate scale of 0.474 mm/arcsec (2.11arcsec/mm). The converter box concept is to change the light emerging from the 61" to mimic the 61" MMT subaperture. The $f/13.5$ light from the 61" is close to that of the $f/15$ beam of the MMT, so a simple magnifying lens, operating with a magnification of 4.74 ($=PS_{MMT}/PS_{61''}$), almost accomplishes the whole conversion. The magnifying lens images the 61" focal plane to a conjugate plane with the MMT plate scale. This is seen in figure 4.2 as the production of the correct plate scale but a slightly incorrect $f/\#$. Completing the description of this figure, field lens 1 (at the 61" focal plane) serves to place a pupil at the magnifying lens. This allows the magnifying lens to collect all of the light, yet remain of a small diameter. Field lens 2 (at the created-MMT focal plane) will serve to place the exit pupil of the system at the correct distance from the created-MMT infinity focal plane.

Another aspect of the MMT subaperture is that it is off-axis. The schematic design of conversion optics that produces the equivalent of an on-axis subaperture is illustrated on the right side of figure 4.2. To make the subaperture off-axis, the correct amount of tilt may be added in an equivalent MMT image plane. This will be accomplished (figure 4.3) by using a field mirror very near the second field lens shown in figure 4.2.

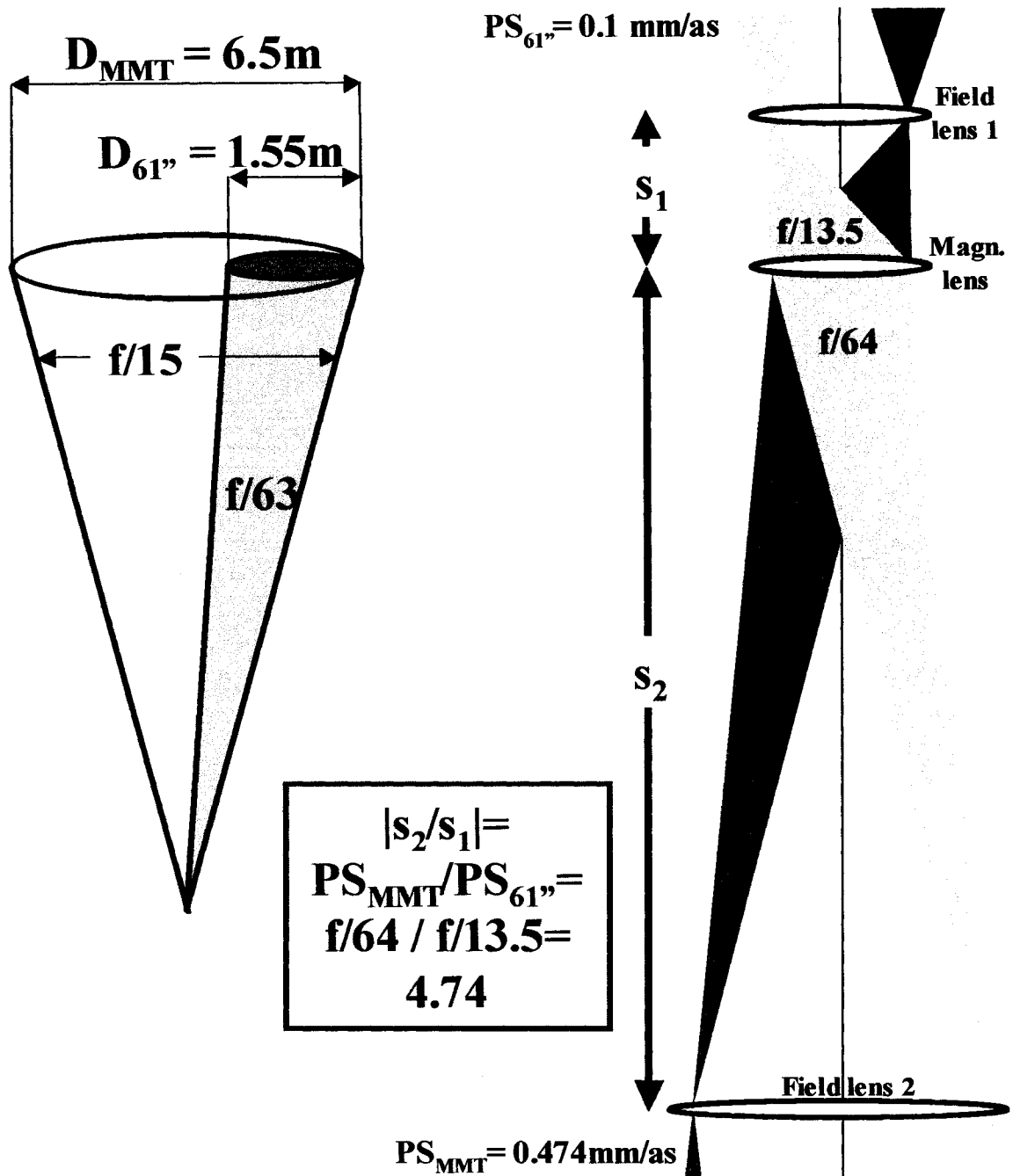


Figure 4.2 On the left side of the above figure, the full MMT cone of light is compared to the cone of light coming from an MMT 61" off-axis subaperture. On the right side of the above figure the 61" to MMT converter box philosophy is diagrammed.

A detail noticed from figure 4.2 is that the image at the equivalent MMT image plane has undergone a parity change. The light gray beam that starts out on the left at the 61" focal plane ends up on the right at the created-MMT focal plane. This can be dealt with by using a k-mirror. The complete schematic for the design philosophy is now shown in figure 4.3.

Stepping through the components in figure 4.3, the k-mirror introduces a parity change. Field lens 1 and the magnifying lens were discussed above. The field mirror adds tilt in an (nearly) image plane, which introduces translation in a pupil plane. The tilt of the field mirror is what makes the subaperture appear off axis. In addition, field lens 2 places the created-MMT exit pupil at the correct conjugate.

The light exiting the last element of the converter box, field lens 2, appears as if it is coming from an off axis subaperture on the MMT. Because of this, the MMT DR system may be placed following the converter box. The off-axis subaperture light is drawn as the shaded gray beams, the full MMT beam is traced out by the dashed lines. The pupil that is formed at the entrance of the DR objective is shown by the convergence of the light beams as well as face on, in both cases the 61" off axis subaperture is located at the bottom.

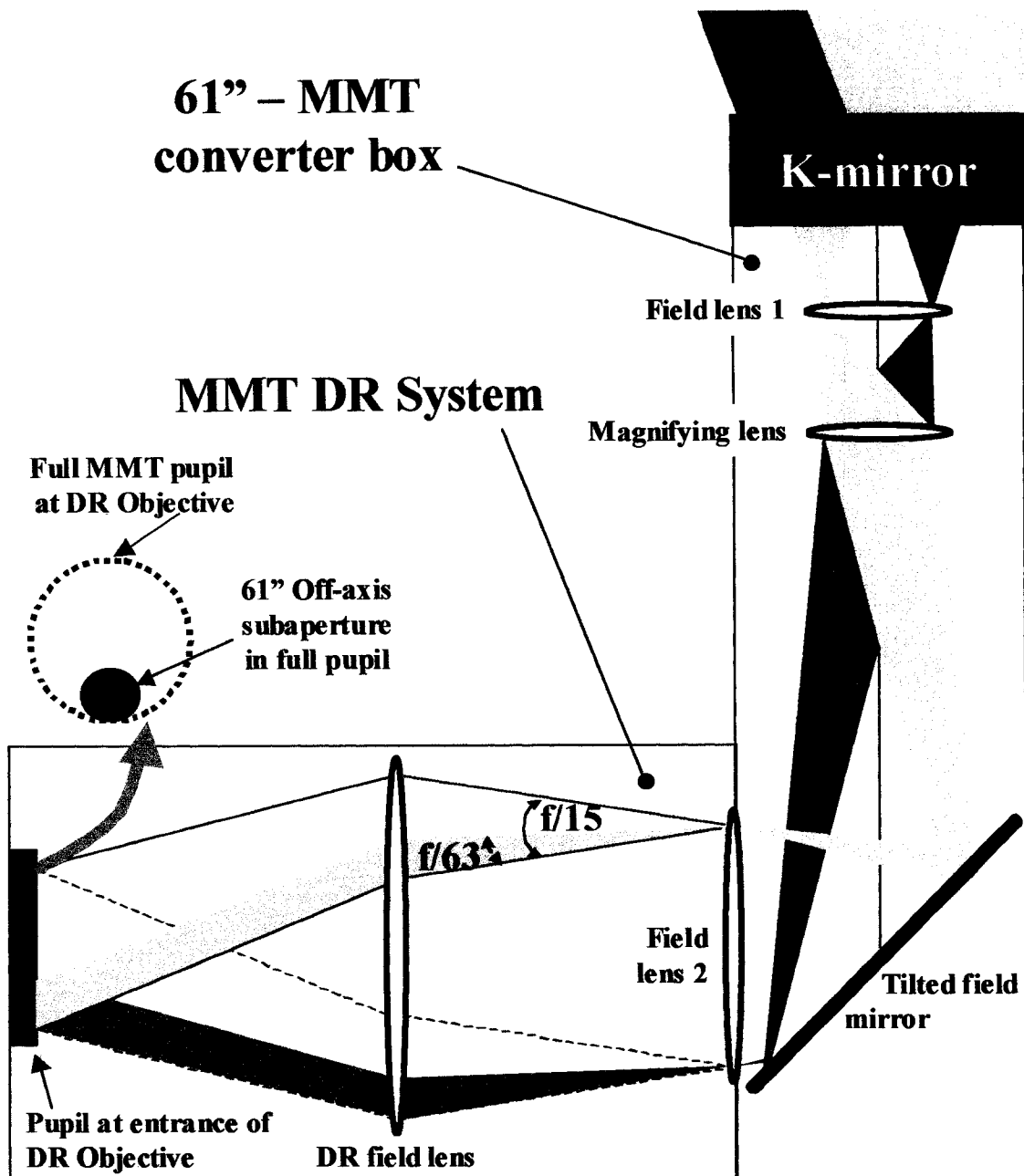


Figure 4.3 Shown above is a more complete schematic of the 61" to MMT converter box that now contains a tilted field mirror that translates the exit pupil of the converter box. The MMT DR optics are also shown, the subaperture beams (filled gray beams) are shown in comparison to the full MMT beam. The off-axis subaperture is illustrated in the pupil near the DR objective.

The philosophy discussed above was inputted into Zemax to create the converter box design presented in the next section.

4.3.2 DESIGN AND EXPECTED RESULTS

Figure 4.3 shows the design philosophy for the 61" to MMT converter box, which is very close to that of the final design. The obstacles that remained are: the 61" is $f/13.5$ which is close but not exactly $f/15$, the optics to be used need to be cheap and off-the-shelf (therefore, they could not get too large), the optical set-up had to fit into a finite amount of space and of course, it has to introduce very little aberration.

A system similar to figure 4.3 was inputted into Zemax with lens parameters that were approximately "buyable". Zemax was optimized using constraints of output $f/\#$, exit pupil location and plate scale magnification. Then one by one, Zemax optimized lenses were replaced with similar off-the-shelf lenses, and the system was re-optimized. This was done iteratively until all lenses were off-the-shelf and all the system constraints were met. In the resulting design, the position of field lens 1 & 2 differed from the exact infinity focal planes; this is what compensated for exit pupil location and $f/13.5 \neq f/15$. The result, folded up with the MMT DR system attached is shown in figure 4.4.

The k-mirror consists of 3 Edmunds' mirrors (in order, 32-125,45-336 & 32-134) each with Edmunds' enhanced aluminum coating, which has a quoted reflectance of $>95\%$ for

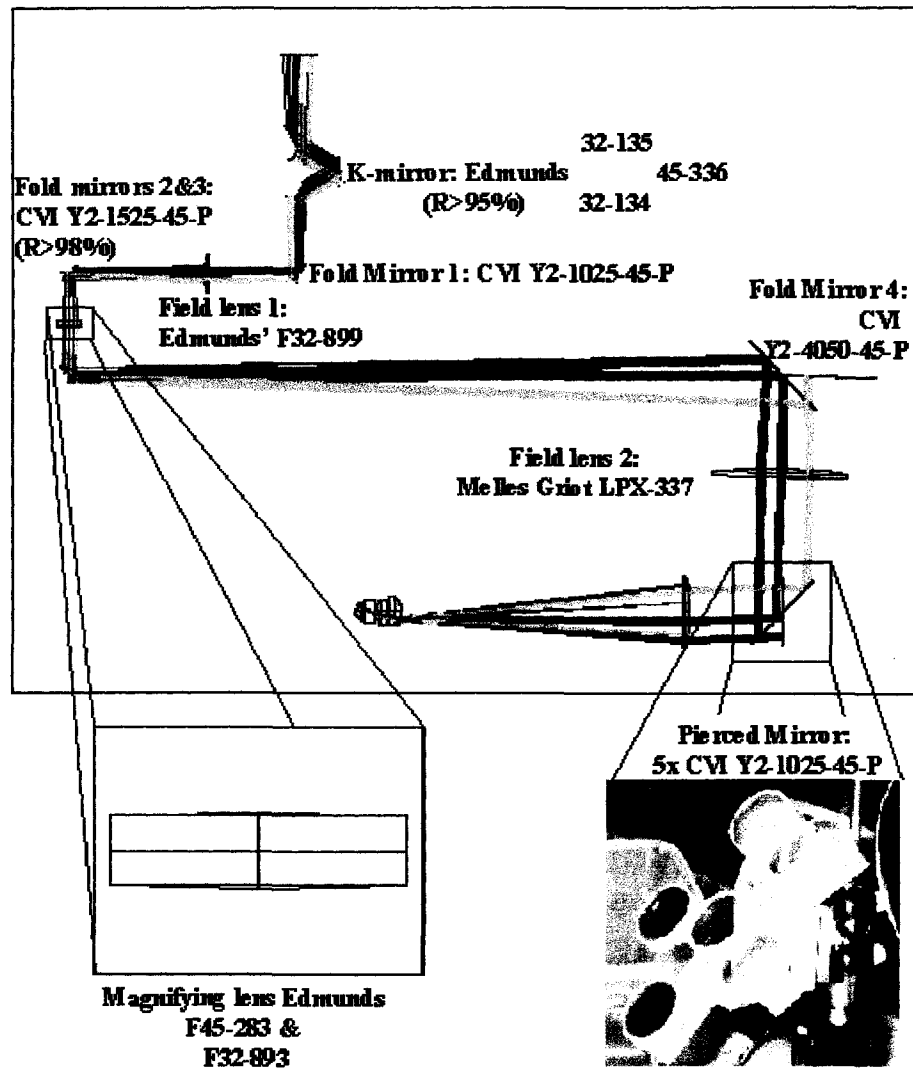


Figure 4.4 The 61" to MMT converter optics are diagrammed above. The off-the-shelf optical components are labeled and the pierced mirror is shown as an inset at the bottom left.

the visible range. Field lens 1 is an Edmunds F32-899, a $\lambda/4$ MgF₂ coated, 40mm diameter, 200mm focal length plano-convex lens. The magnifying lens is actually two plano-convex lenses with their plano sides touching (see figure 4.3). This was done to get the desired ROC's on each surface. The two plano-convex lenses are both Edmunds and are, a F45-283 $\lambda/4$ MgF₂ coated 25mm diameter, 750mm focal length lens and a F32-893 $\lambda/4$ MgF₂ coated 25mm diameter, 400mm focal length lens. Field lens 2 is a Melles Griot LPX-337, a $\lambda/4$ MgF₂ coated 145mm diameter, 1,000mm focal length plano-convex lens. All of the fold mirrors, "pierced mirrors" and the large field mirror are from CVI and coated with their Y2-532-45P coating, which has a quoted reflectance of >98% for s and p polarizations at 45° for 532nm light.

Fold mirror 4 is tilted at approximately 1.5 degrees, which is equal to $\tan^{-1}(1 / 97.5)$ (see figure 2.8 for a definition of 1). This translates the system's exit pupil to the correct position of a 61" off axis subaperture. The pierced mirror is at 45 degrees because that is how it would be placed on the MMT.

The many rays shown in figure 4.4 correspond to a regular pentagon projected on the sky; the modeled geometry of the Rayleigh beacons is shown in figure 4.5. A regular pentagon (with diameter 120arcsecs) is projected on the sky with a point facing north. The center of the beam projector is an MMT radius from the edge of the 61", to the South. As an aside, when modeling in Zemax, in an MMT design the beams may be

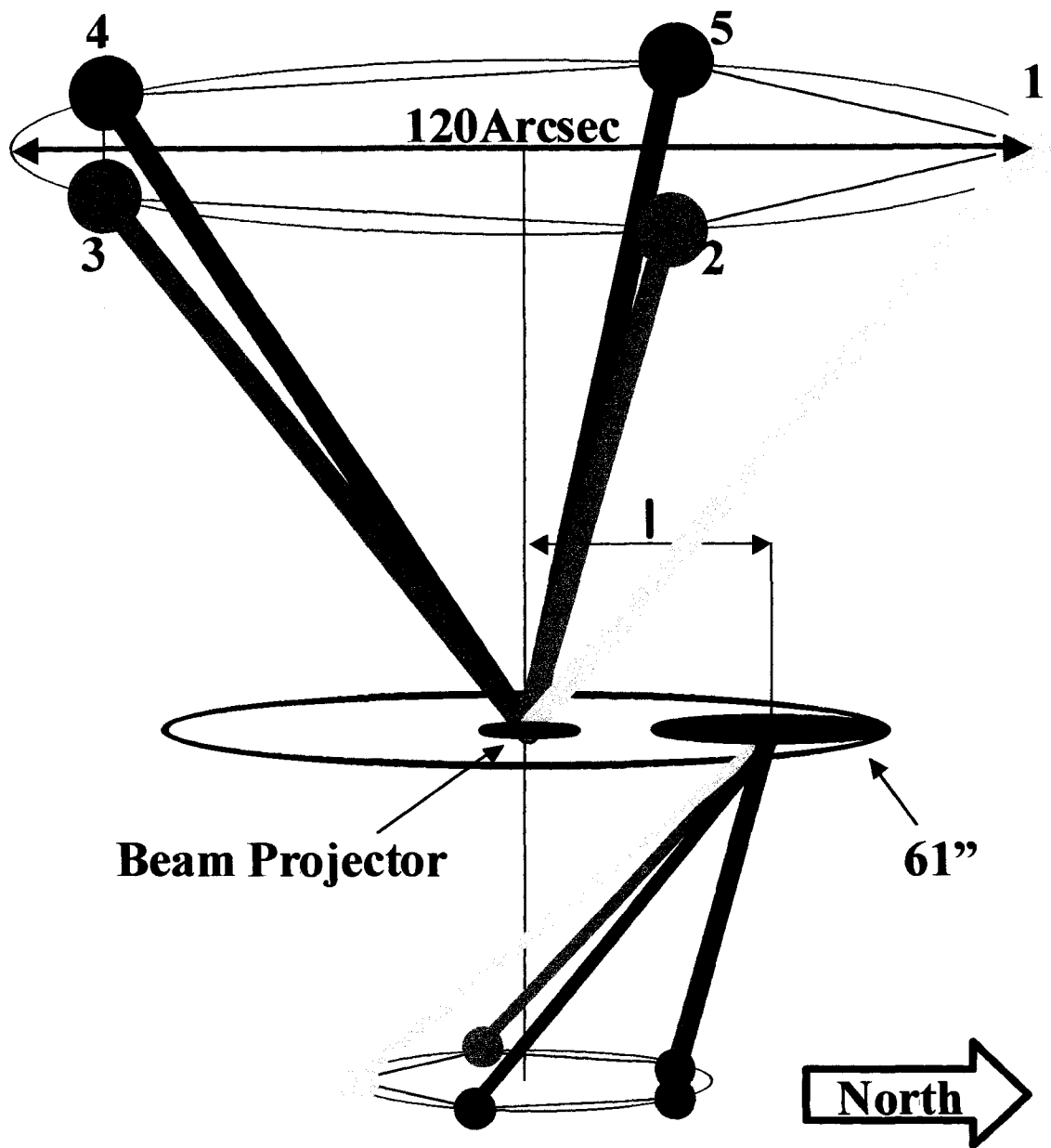


Figure 4.5 The geometry used for the 61"DR experiment of the five Rayleigh beacons. The beacons fall on a regular pentagon that is inscribed within a 120arcsec diameter circle. One of the pentagon's points, designated spot 1, is directed north. The beam projector is situated 2.475m from the center of the 61" telescope, to the South.

inputted simply as field angles. In the case of the off-axis subaperture, the field inputs were found by solving for Cartesian (x,y) position relative to the 61” axis given laser spot altitude (z).

The performance of the converter box, coupled with the MMT DR system is shown as a “configuration matrix spot diagram” exported from Zemax (figure 4.6). Each of the spots (numbered in figure 4.5) are shown for heights 20,25,30 and 40km. The image plane for these spots is the 25km conjugate fixed focal plane (the DR field lens) after being dynamically refocused. The scale bar (shown in the 20km,spot #1 box) corresponds to 1mm or 2.11arcsecs in the MMT plate scale. The circle drawn in each picture is the airy disk diameter that corresponds to diffraction-limited performance. The largest RMS diameter is 203 μ m (0.43arcsecs) and corresponds to spots 3 and 4, with nominal performance for all other spots of about 50 μ m RMS diameter. The design performance of the converter box represents an RMS spot diameter of less than ½arcsecond for all beams at all DR heights.

4.3.3 CONVERTER BOX AND MMT DR SYSTEM ALIGNMENT

As seen in figures 4.3 and 4.4, the amount of optics in the converter box small, only three lenses and a few fold mirrors. The alignment of this system should be very straightforward. However, it requires a bit of TLC and finesse, especially when coupling

	Spot #	20k	25k	30k	40k
0.00, 9168.28 μm	1		•	•	•
11200.00, 1120.15 μm	2	•	•	•	•
6834.19, -11888.60 μm	3	•	•	•	•
-6834.19, -11888.60 μm	4	•	•	•	•
-11200.00, 1120.15 μm	5	•	•	•	•
SURFACE: IFF					
CONFIGURATION MATRIX SPOT DIAGRAM					
LENS HAS NO TITLE, FRI OCT 10 2003 UNITS ARE MICRONS.					
RURY DIMS : 79.81-88.75		REFERENCE : CHIEF RAY		<small>WWW.PLEASANTHILL.COM/WWW.ZEMAX.COM/LENS/LENS.ZIX</small> CONFIGURATION: ALL 4	

Figure 4.6 The configuration matrix produced by Zemax for the dynamically refocused images of the spots diagrammed in figure 4.5 is shown above. The largest spot sizes correspond to spot 3 and 4 and have an RMS diameter of 0.43arcsec.

it to the MMT DR optics. This section will introduce the alignment philosophy, optics and procedure used.

4.3.3.1 ALIGNMENT PHILOSOPHY

The basis of my alignment philosophy is to be able to build the system from the ground up on a short enough timescale that it may be built and rebuilt a few times over the course of an observing night. I felt that this was critical function for a prototype system, like this one, where experimental results may be achieved, analyzed and it found necessary to make an “on the fly” adjustment.

On future systems where DR is not the goal, but a tool, this will not be necessary. But while DR was itself the experiment, my set-up treated it as such. It should be noted here, that the experiment was shipped to the mountain unassembled. It was done this way because most of the optical mechanical structures were adjustable to allow for unforeseen adjustments that may be deemed necessary. Because of this, I did not trust that any assembly done in the lab would port reliably to the mountain.

In addition to allowing for a quick assembly, the alignment procedure must allow for a robust enough assembly to produce results similar to those predicted by the design (section 4.4.2).

With these constraints in mind, I developed the alignment procedure that is described in the next few sections. It is not an interferometrically accurate procedure, nor is one done purely by eye. In the end produced results similar to those predicted in section 4.4.2, and gave us the flexibility on the mountain that the experiment required.

The remaining sections of 4.4.3 will explain how this alignment takes place, in a temporal manner. Along with the alignment of the optics outlined in section 4.3, the alignment optics themselves will also be discussed. Because the optics must exist on some structure, the procedure is begun with a brief discussion of the cage.

4.3.3.2 THE CAGE

A welded steel tube cage (figure 4.7) designed by Matt Rademacher and fabricated by the UofA Instrument Shop is the support structure for the converter box optics and MMT test bed when attached to the 61". The steel tubing is 1.5 x 1.5 inches with 0.080inch thick walls. It was designed and built in two parts, the upper cage supports the converter box optics described in section 4.3, the lower cage holds the MMT test-bed that will be described in section 4.4. When both parts are connected, the full cage weighs approximately 220lbs.

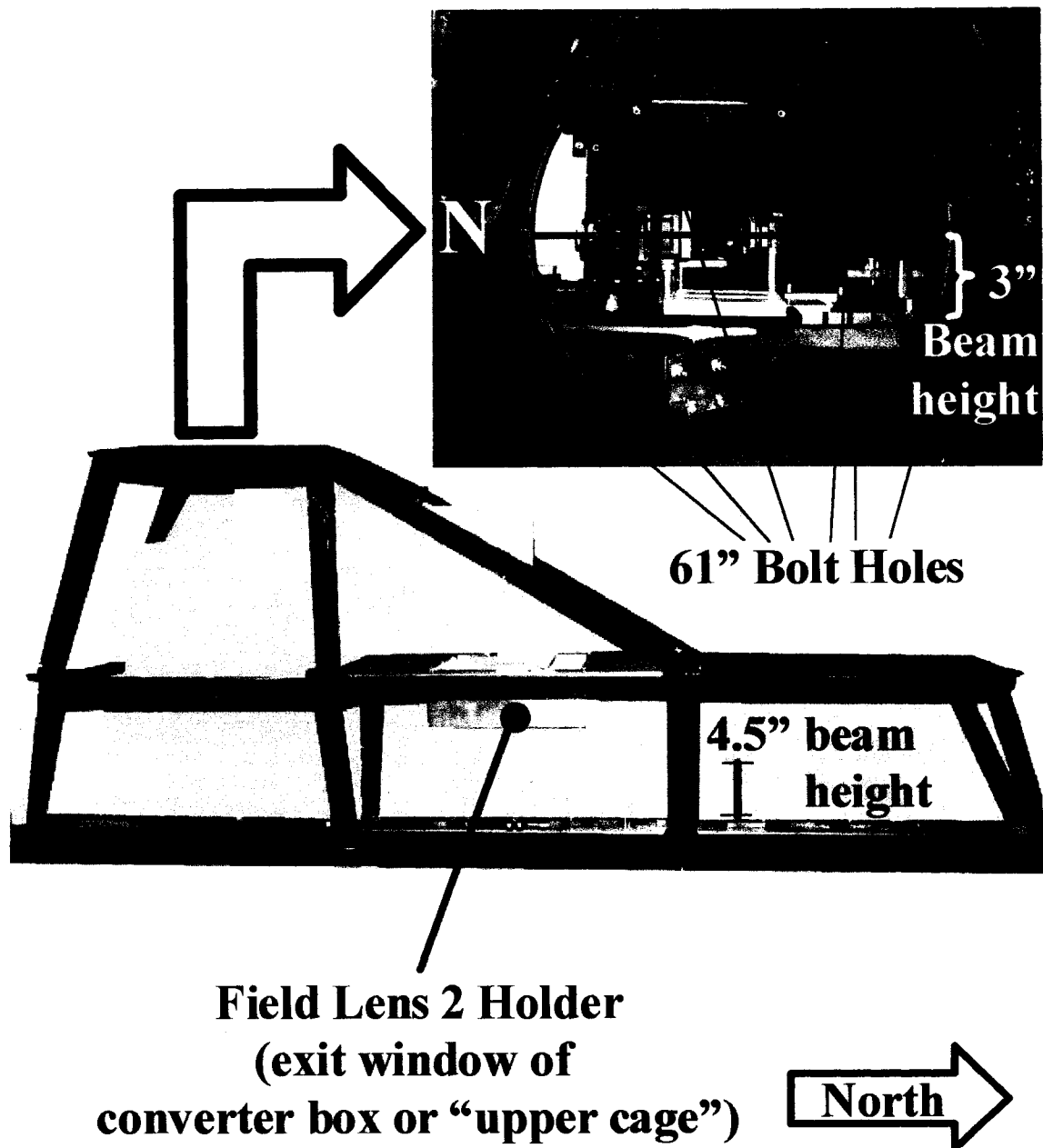


Figure 4.7 The steel cage that supports the 61" DR is highlighted above. The cage was made in two parts: the upper cage supports a breadboard that is mounted vertically and the lower cage supports a breadboard that is mounted horizontally. Shown in the top picture, the breadboard in the upper cage located is 3 inches below the optical beam height while the breadboard in the lower cage is 4.5 inches below the optical axis.

The upper cage, which mounts to the 61” rotator plate, is the support structure for an optical breadboard. The breadboard is mounted vertically and supports the converter and alignment optics. The breadboard is situated 3 inches (within about a millimeter) below the geometrical center of the 61” bolt pattern (assumed to be the 61” optical axis) and is perpendicular to the mounting plate (within a few millimeters). In addition, a large aluminum lens holder (for field lens 2) is fixed to the upper cage; this is shown in figure 4.7.

The lower cage mounts to the upper cage and supports the MMT DR optics and test-bed (discussed in section 4.4). The optical bench for the lower cage is another aluminum breadboard; this one is situated horizontally. The beam height is designed to be 4.5 inches above this breadboard.

4.3.3.3 ALIGNMENT PROCEDURE STEP 1: LASER AND MIRRORS

The upper cage supports an optical breadboard 3 inches below the optical axis of the 61” (figure 4.7). As a result of the way the cage was designed and manufactured there are three fixed constraints that the optical layout (of figure 4.4) needs to fit within: the optical axis of the telescope along with the locations of fold mirror 4 (previously referred to as field mirror in figure 4.3) and field lens 2. Because the layout is anchored to these points, it is fit onto the breadboard by being flexible with the locations of fold mirrors 1 and 2, as well as adjusting the infinity focal point of the 61” (by means of moving the 61”

secondary). All locations, separations and sizes of the optics in the system are obtained from the Zemax model. These parameters, as well as the optical axes connecting them, are laid out on the breadboard with paint pen.

Cardboard irises were created with a ~ 1 mm aperture located 3 inches above a stable base (figure 4.8). A line is drawn along the center of the iris' base so that when it is placed over a drawn paint pen line, the iris' aperture is 3 inches above the line within approximately a millimeter.

An internal alignment laser is placed at the far end of the optical layout (IAL in figure 4.8). Two irises, separated as much as possible, are placed along the optical axis that was drawn immediately following the laser. The laser is adjusted until its beam passes through both of the irises. This outlines the basis for how the reflective elements are aligned to the drawn optical layout: Irises are separated as much as possible and placed along the paint pen line drawn following any reflective element in the system. (An example of this is shown as the cartoon part of figure 4.8.) The element is then adjusted so the light passes through both irises. The element is also adjusted so the laser beam falls very near the geometric center of the reflective element.

Alignment mirrors 1 and 2 (AM1 & AM2) are placed in the system in this manner.

AM3, which is removable, because it blocks the 61" beam, couples the alignment system

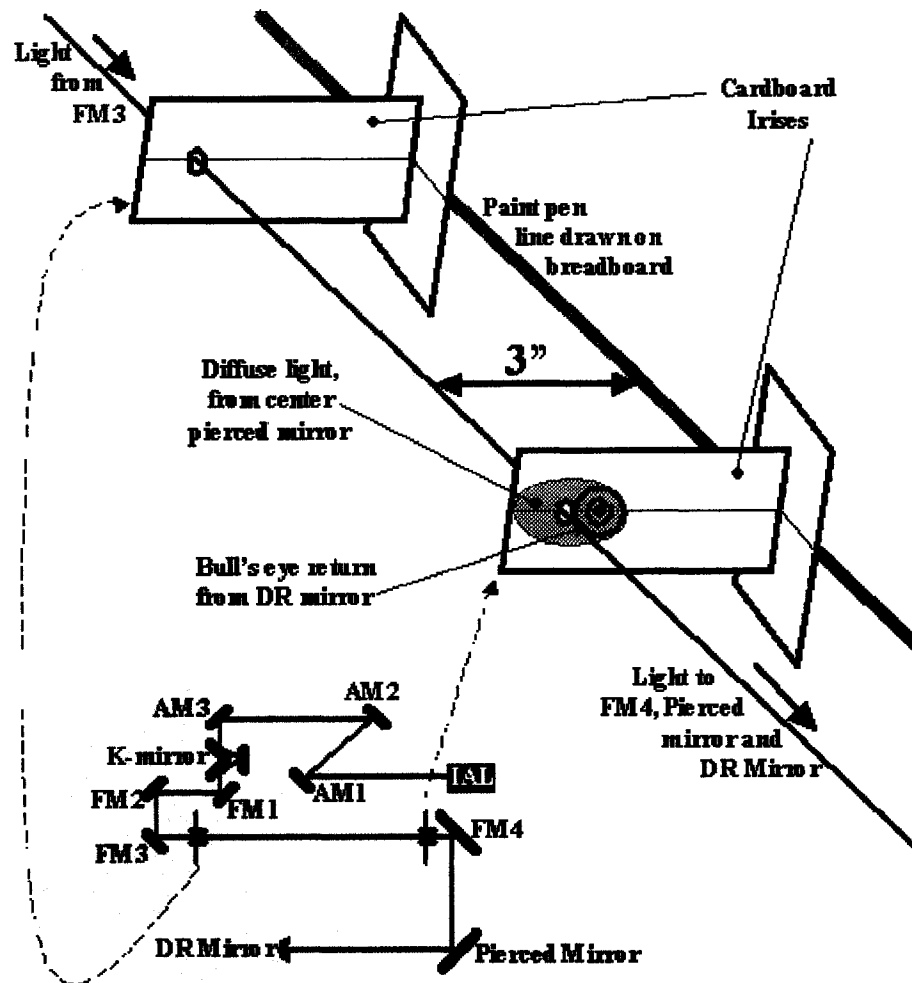


Figure 4.8 The reflective surfaces in the converter optics, DR optics and alignment optics are highlighted in the bottom of the figure. The reflective elements are the first components aligned in the 61" experiment. The locations of the cardboard irises, used aligning the system, after FM3 is aligned are also highlighted. The cartoon at the top of the figure shows light from the DR mirror after it is aligned with respect to the irises.

to the converter optics. The line drawn as the optical axis following AM3 is assumed to be the optical axis of the 61" itself.

With AM3 in place, the k-mirror is to be placed in the system. The k-mirror was constructed as a single entity. The bolt holes that hold the k-mirror to the breadboard are slightly oversized, so the unit may be slightly translated and tilted. This is done until light leaving the k-mirror follows the same path as light leaving AM3 (which follows the paint pen line that represents the optical axis of the telescope).

The basic alignment procedure is continued until reaching FM4. Cardboard irises are kept in the positions that were used to align FM3 (figure 4.8). On the lower cage breadboard, a mark was made that is geometrically below the center of FM4. FM4 is tilted so that the alignment laser is directed at this mark.

The pierced mirror is then placed in the system and initially positioned by tilting and translating (North-South) the mirror until the reflected laser beam is at a constant height of 4.5 inches. This is the nominal beam height, but because there are no x-y translation capabilities on the DR mirror the alignment laser and thus the pierced mirror must be slaved to the DR mirror position. The DR mirror is epoxyed to the resonator that is held firmly in the driver. A linear translation stage serves to focus the DR mirror, which has no other alignment capabilities.

The resonator and DR mirror are then loosely installed into the system. The resonator system may be roughly aligned by hand because of very slightly oversized bolt holes. The internal alignment laser is directed at the DR mirror and is quickly diverged upon reflection. The DR mirror is made of diamond turned aluminum. Imperfections due to the diamond turning process create concentric rings in the reflected diverging laser light. These concentric rings are used to align the resonator and pierced mirror.

By roughly adjusting the resonator system the image of the concentric rings is placed back near the last cardboard iris in the system (that remains placed before FM4, see figure 4.8). The vertical position of the concentric rings may be fine-tuned by tilting and translating (again, North-South) the pierced mirror. This procedure is done until the brightest rings are at the same vertical position of the cardboard iris aperture. To insure that the IAL beam is at the geometric middle of the center pierced mirror, the diffuse reflection off this mirror is examined. Pure translation should place the diffuse reflection evenly about the iris aperture.

The horizontal position of the concentric rings may not be fine-tuned; the degrees of freedom required to do this are not present in the system. It is true that FM4 may be tipped and tilted in conjunction with the tip and tilt of the pierced mirror to walk the

concentric rings. This is, however, not an acceptable solution because the tip and tilt of FM4 are what controls the subaperture position at the DR objective pupil.

At this point in the alignment procedure, all of the reflective elements are considered to be “squared-up”; the alignment laser follows the path traced out by the optical layout geometrically drawn on the breadboard. The next step is to align the MMT DR optics.

4.3.3.4 ALIGNMENT PROCEDURE STEP 2: MMT DR SYSTEM

As outlined in the last section, the light is now aligned with the DR mirror to within the degrees of freedom allowed on this system. The next step is to place the DR objective into the system. The objective is treated as a single element and is the only element shipped to the mountain assembled. Its alignment was outlined in section 3.2.6.1. In order to isolate the reflections caused by the objective only, a piece of paper is placed between the exit of the DR objective and the DR mirror. The back reflections from the surfaces of the lenses will be sent back toward the iris, still near FM4. The back reflections can be aimed toward the iris aperture by translation and tip/tilt of the DR objective. When the objective is very close to being aligned, circular fringes will be seen.

The objective is then fine-tuned by removing the paper in front of the mirror and then adjusting the DR mirror focus so that the IAL light is focused at the cardboard iris on return. The DR objective and mirror system is aligned when:

- The concentric rings of the diamond turned RD mirror are concentric about the iris aperture
- The return focus passes through the iris aperture
- The return focus does not shift about the aperture in any way when the DR mirror is translated through focus

An even more discriminating check of this alignment would be to test the above, not only at the cardboard iris but also in the exit aperture of the IAL itself.

If the return spot does shift about the cardboard iris when the DR mirror is taken through focus, it may be alleviated by walking the translation and tilt knobs of the DR objective corresponding to the shift direction.

The next element to align is the DR field lens. The alignment of this element is similar to all of the other refractive elements in the system. The IAL light entering the DR objective is blocked, so that no light may be seen back at the FM4-iris. A target is placed on the blocking element (usually cross hairs on a post-it note), indicating the path of the IAL beam. The field lens is placed in the system so that it is 300mm from the DR objective and 100mm from the center of the pierced mirror. It is adjusted in translation (x and y) until the back reflections of both its surfaces are coincident. It is then tipped and tilted so that both of these coincident back reflections pass back through the iris

aperture. At this point it is checked that the IAL light still hits the marked target, i.e. the cross hairs where the light hit before the DR field lens was placed in the system.

This procedure places the field lens along the path of the IAL in a manner that is sensitive to translation and tip/tilt to an accuracy defined by the lever arm between the DR field lens and the iris. The placement of the field lens is dependant on the geometrical layout drawn on the lower breadboard. It is assumed that the lens can be placed within a few millimeters. Considering the distances involved, this would correspond to a very small magnification effect.

As mentioned, this is the basic procedure used for all refractive elements. Again, it relies on the geometrical layout and the ability to place the element at its desired position to within a few millimeters. Misalignment due to misplacement in the z-direction mainly causes slight magnification problems. Again, given that the nature of the experiment was to prove dynamic refocus, this type of error was deemed acceptable because it is easily understood and does not cause imaging aberrations.

However, decenter and tip/tilt of the refractive elements will cause aberrations that will degrade and blur the image. The back reflection/ forward image method is the most straightforward and fastest geometrical method to correct for these errors.

Returning to the alignment, at this point the MMT DR optics have been aligned. In the course of this alignment, it was assumed that they are on axis; it is known that this is not the case in the 61" test. The off-axis ability occurs when FM4 is tilted, which is the subject of the next section.

4.3.3.5 PROCEDURE STEP 3:TILT OF FOLD MIRROR 4

Due to the manufacturing, the aluminum breadboard of the lower cage is a fixed distance, 369mm, away from the center of FM4. For a beam tilted at 1.5degrees, it will fall 9.7mm to the South of the mark placed directly below FM4's center. The beam is moved this distance by turning the horizontal knob of the FM4 mirror holder 3.5 turns.

The tilted beam also requires a displacement of 6.67mm, to the South, of the pierced mirror, which was centered at 4.5inch beam height. This is accomplished by moving the linear translation stage on which the mirror is attached.

There is no movement of any element of the MMT DR system. These elements remain aligned as if they were on the MMT, which means they remain "on-axis". At this point in the alignment procedure, the mirrors are squared in the converter box, the DR optics are aligned and the field mirror, FM4, is tilted as prescribed.

4.3.3.6 ALIGNMENT PROCEDURE STEP 4: REMAINING REFRACTIVE ELEMENTS

The next step in the alignment procedure, which is working for the most part backwards from the DR optics, is to align field lens 2. This lens has its own custom holder that is attached in a fixed z-position to the upper cage (figure 4.7). The lens itself is held by a cell with one degree of tilt that corresponds to the tilt of FM4. The cell has dramatically oversized bolt holes in order to provide some x-y translation. Using this structure, this lens is aligned as outlined in the last section.

Continuing, the magnifying lens and field lens 1 are placed in the system (in that respective order, see top of figure 4.9). At this point, the converter box is basically aligned. However, the alignment system (yet to be aligned) will provide an $f/13.5$ beam that will allow for a full test of the system.

The alignment system is shown in the bottom part of figure 4.9. It is designed to place the focus of a nearly $f/13.5$ beam of light on the 3rd mirror of the k-mirror. This focal

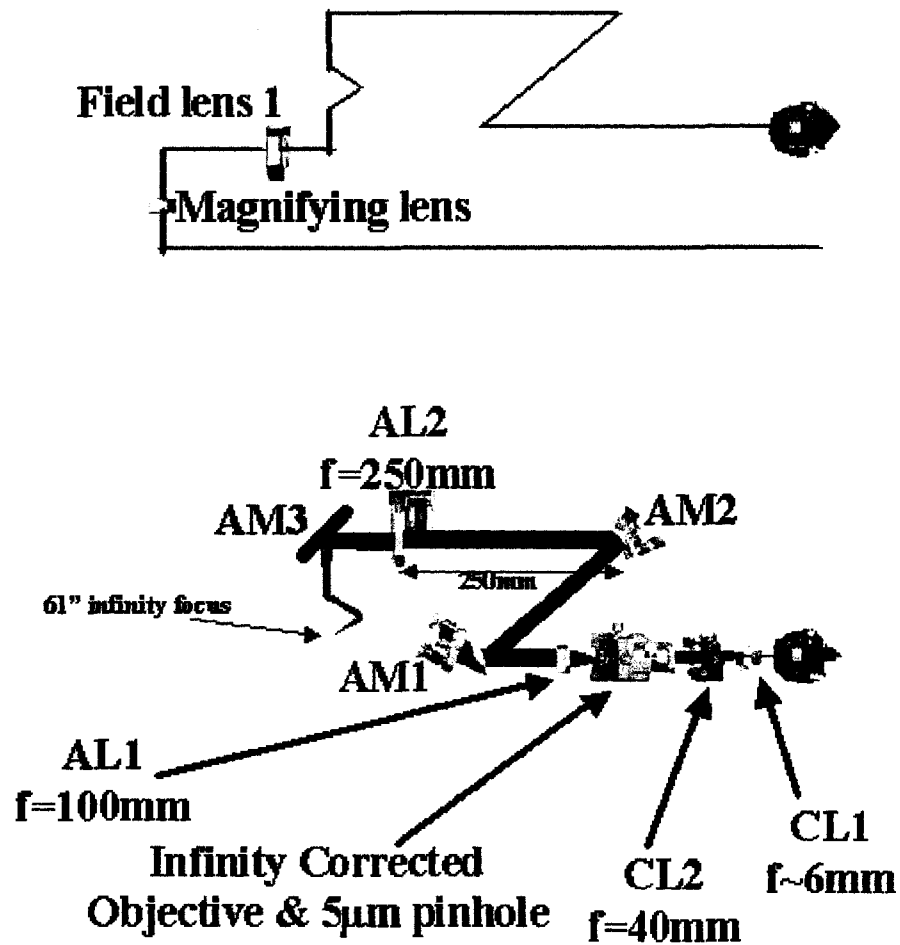


Figure 4.9 The top image shows field lens 1 and the magnifying lens placed of the converter optics placed in the system. The bottom image shows the operation of the alignment optics, which produce an $f/13.5$ beam focused at the surface of the last k-mirror, which is coincident with the 61" infinity focal plane.

position corresponds to the Zemax layout of the converter box. The alignment of these optics require some finesse.

As an overview, the IAL is roughly collimated by CL1 and CL2 and sent through an infinity corrected microscope objective. The light from this objective comes to a focus and is cleaned up by a 5 μ m spatial filter. AL1 is placed a focal length from the pinhole creating collimated light. AL2 focuses light on the third k-mirror, which corresponds to the designed infinity focal plane of the 61”.

To begin to set up the alignment optics AL1, AL2, the infinity corrected microscope objective, collimating lens 1 and 2 (CL1 & CL2) were each individually adjusted for height. By virtue of its mount, the infinity corrected objective may be placed in the system, aligned and removed leaving the mount in place. The metrics for aligning this objective are again the back reflections on the laser face and how evenly illuminated are the optics following the objective.

The objective is removed from the mount, so that it may be replaced with sufficient repeatability. CL2 is placed in the system examining the back reflections at the laser and the forward image at the cardboard iris near FM3 (see figure 4.8). CL1 is placed in the system and its resulting back reflections are examined. The more telling metric of the

alignment of this lens is the size and location of the nearly collimated beam falling on AM1, as well as the location of the beam falling on the iris near FM4.

CL1 and 2 present an expanded collimated beam to the infinity corrected microscope objective. Their alignment is not critical, since the light exiting the will be cleaned up by the 5 μ m spatial filter.

The microscope objective is returned to its mount along with the 5 μ m pinhole. The objective is then focused through the pinhole.

AL1 is now placed in the system to create collimated light. When aligning this lens, one does not have access to back reflections. It is noted that this lens (as well as AL2) is not crucial to the final operation of the DR system, it only serves to aid in the alignment and the characterization of the system. The method to align this lens is to first observe the approximately collimated light leaving the lens and falling on AM2. With AL1 in the system, a point image will be formed very near the iris after FM3. The lens is moved so this point image passes through the iris and the beam falling on the next iris does so evenly about its aperture.

A shear plate is placed along the optical axis between AM1 and AM2. AL1 is situated on a linear translation stage that is moved until the light leaving AL1 is collimated.

The last element in this part of the system is AL2, which is situated a focal length from AM2, making this mirror the stop of a telecentric system. Tilting AM2 serves to translate the laser beam in an image plane. AL2 is admittedly placed in the system by eye. When placed properly, the lens will be vertical, a focused laser spot will occur at the 3rd k-mirror and a focused spot will nearly occur at the iris near FM4.

There is little need to place AM2 ultra precisely because it is operating at nearly diffraction limited, it is an achromat producing an $f/13.5$ beam. The most important result of the placement of this lens is to produce a sharp image in the correct image plane.

4.3.3.7 ALIGNMENT PROCEDURE STEP 5: FINALIZING

At this point in the alignment procedure, all optical elements are placed in the system.

Only a couple procedures remain before the system may be tested. The first of these is to insure that there is a sharp focus at the 3rd k-mirror. Focusing AL1 by means of the linear translation stage it is clamped to easily accomplishes this.

The next detail is to ensure that the 61” infinity focal plane is re-imaged to designed MMT infinity focal plane. This is accomplished by focusing the magnifying lens by means of the linear translation stage it is clamped to.

The last thing that needs to be accomplished is that the IAL beam must mimic one of the five pentagon spots (figure 4.5). Spot 1, the northernmost spot, is usually chosen. To accomplish this, AL1 is refocused so that a sharp spot occurs at the DR field lens. Next, the pupil mirror AM2 is tilted until the spot is at the correct location on the DR field lens (given the MMT platescale). Finally, the DR mirror is focused to return a sharp spot back at the DR field lens. These spots should both lie on a 120arcsec diameter circle, about the DR field lens geometric center. This symmetry is actually a good test of the alignment. If the DR mirror focuses a sharp spot that is not symmetric with the incoming beam, something is incorrect.

The alignment procedure is returned to in section 4.4.3.

4.3.4 CONTRIBUTION TO TOTAL ERROR

At this point in the alignment of the system, the converter box and MMT DR optics are complete and placed in their nominal, 25km, position. However, the system cannot be actually tested (other than by eye) in this state. The 120arcsecond field, which is 57mm at the DR field lens, must be reduced in order to be fully seen with a CCD. The

operational reduction of the focal plane is what will be discussed in the next section. However, a non-operational reduction can be made. This demagnification reduces the field lens and the spots contained within) by a factor of 7 and places this image on a CCD. It is assumed that the de-magnification optics introduce no error to the system. The results are shown in figure 4.10.

The expected geometrical spot is given by Zemax as 0.27arcsec and is approximately diffraction limited. The actual results are about twice this size (FWHM = 0.53 vertical and 0.45 horizontal). This may be justified by: the liberties taken with the AL1&2, diffraction effects, magnification effects and the fact that the reduction optics are not perfect. However, this $\frac{1}{2}$ arcsec image is better than seeing limited. This firmly states that the converter box and MMT DR system (in this static case) will not optically affect the image of the Rayleigh beacon.

In summary of section 4.3, an optical system that makes the 61" appear as an off axis subaperture of the MMT was designed, built and tested in situ. The actual alignment of the converter box was outlined in detail. Accompanying this converter box is an alignment system that remains in place and only requires the removal of a mirror (AM3) when the system is operational (viewing DR on the sky). When tested, the converter box operates very near its design specifications, and well under the expected seeing limit for a double pass Rayleigh beacon.

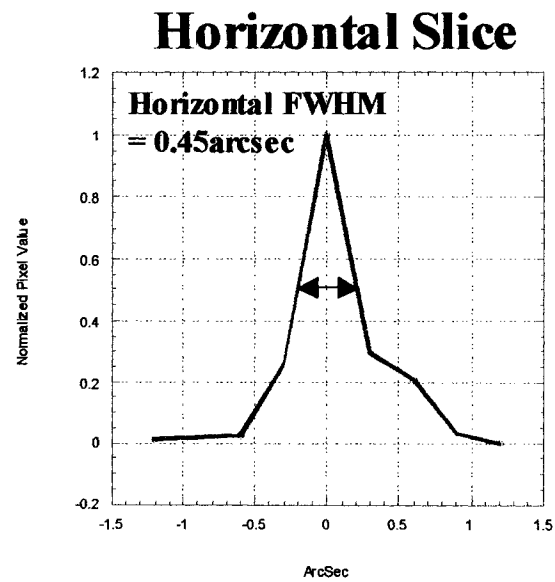
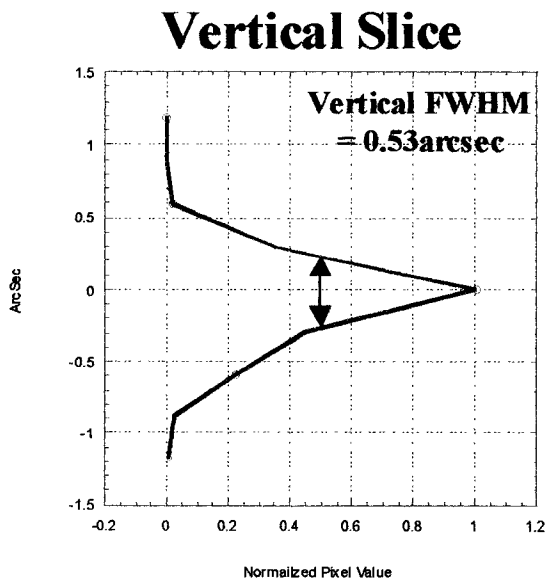
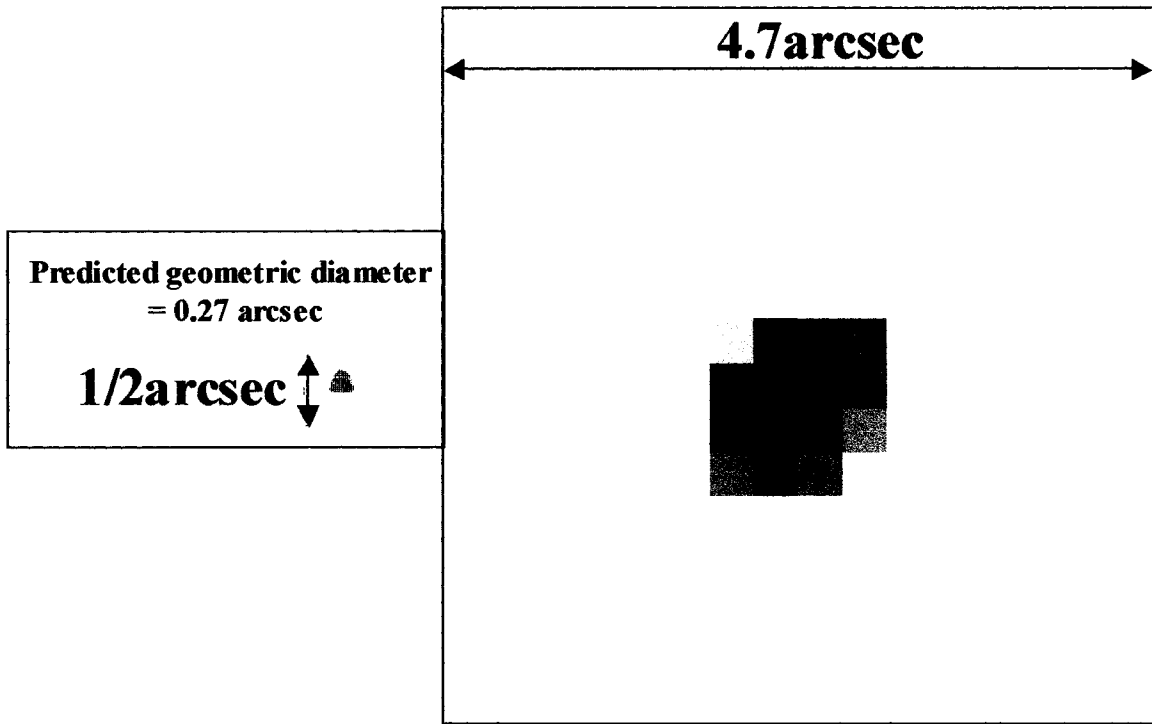


Figure 4.10 The results of aligning the converter box on the 61" telescope are shown compared to the predicted results. The PSF of the converter box is roughly twice the predicted value, but a third of the size associated to double pass through the atmosphere with 1arcsec seeing.

4.4 DEMAGNIFYING OPTICS AND GATED CAMERA, MMT TEST BED

It was alluded to in the last chapter that the dynamically refocused image at the DR filed lens is almost 60mm, this entire field needs reduced and imaged onto a CCD. It is also a goal of the experiment to investigate light traveling through specific heights in the atmosphere, for example 20-30km. The laser being used is a pulsed laser, so to achieve height discrimination a camera with a very fast shutter is required. It has already been mentioned that the laser will operate as low as 5kHz. In this case (imaging 20-30km @ 5kHz), the camera shutter needs to be open for $66\mu\text{s}$ every $200\mu\text{s}$. The camera we had at our disposal (Santa Barbara Instrument Group, ST-9XE) had a minimum shutter time of near 200ms, so it is obvious that the height discrimination, or range gating, could not be done with this camera alone.

By our group, previous attempts at range gating had been made by utilizing a Pockels cell as a fast shutter. Pockels cells work well for polarized light with very little field. In the current case of the 120arcsec images at the MMT plate scale, the field is appreciable enough to disallow the use of Pockels cells.

Our group did have access to and borrowed a Stanford Computer Optics, Quantum Leap 5n, S20Q micro channel plate image intensifier. This image intensifier works analogously to night vision goggles. Photons incident on a photocathode, placed at a focal plane, have a probability of causing an electron to be ejected from the photocathode

into a micro channel plate. A voltage applied to the micro channel plate causes the ejected electron to cause a chain reaction that creates many more secondary electrons. Upon exiting the other end of the micro channel plate, this large number of secondary electrons is accelerated through an electric field and finally impinges on a phosphor screen, much like a CRT, causing another image plane. This image plane is an amplified version of the original image plane.

Most importantly to this experiment is the fact that the image on the phosphor screen only occurs when there is a voltage applied to the intensifying system. Thus the intensifier may be used as a shutter, allowing an image only when a voltage pulse is present. The minimum gate width is given as 1.5ns, so it is more than sufficient for the purposes outlined above.

The electronic control for the intensifier is outlined in section 4.6, for this section it will be treated as a shutter with an effective PSF. The PSF is a result of transfer through the imaging train described above. The measurement of this PSF including the image reduction onto the photocathode and the imaging of the phosphor screen onto the CCD will be the subject of the remainder of this section.

4.4.1 DESIGN PHILOSOPHY

The design philosophy of the MMT test-bed is given in figure 4.11. The image at the field lens, which is assumed to be at the MMT platescale ($120\text{arcsec} = 57\text{mm}$), needs to be reduced onto the 25mm diameter photocathode. The intensifier then produces an amplified image on the phosphor screen (also 25mm diameter) that must be reduced and transferred onto the CCD (10.2mm square, 512×512 with $20\mu\text{m}$ pixels).

The DR focal plane is at the DR field lens, which is almost 70mm of clear aperture; the intent is to image this entire clear aperture onto the phosphor screen. The demagnification is about $1/3$. This demagnification could be done with a single large diameter lens, however due to spatial considerations, the thought was to employ an optical path similar to the inset at the bottom of figure 4.11. Optical element 1 creates nearly collimated light and places a pupil near element 2. Element 2, may be of small diameter small, collects the full field and places a real demagnified image somewhere following. In this design, element 1 needs to be of large diameter, but not necessarily well corrected since it is only dealing with zonal $f/63$ light. Element 2 however, must be well corrected because it is dealing with a significant field.

It is a good approximation that the light exiting the DR field lens is telecentric.

Therefore, if element 1 collimates the light the pupil will be focal length to the right. An image is then formed at the focal plane of element 2 making the magnification of the

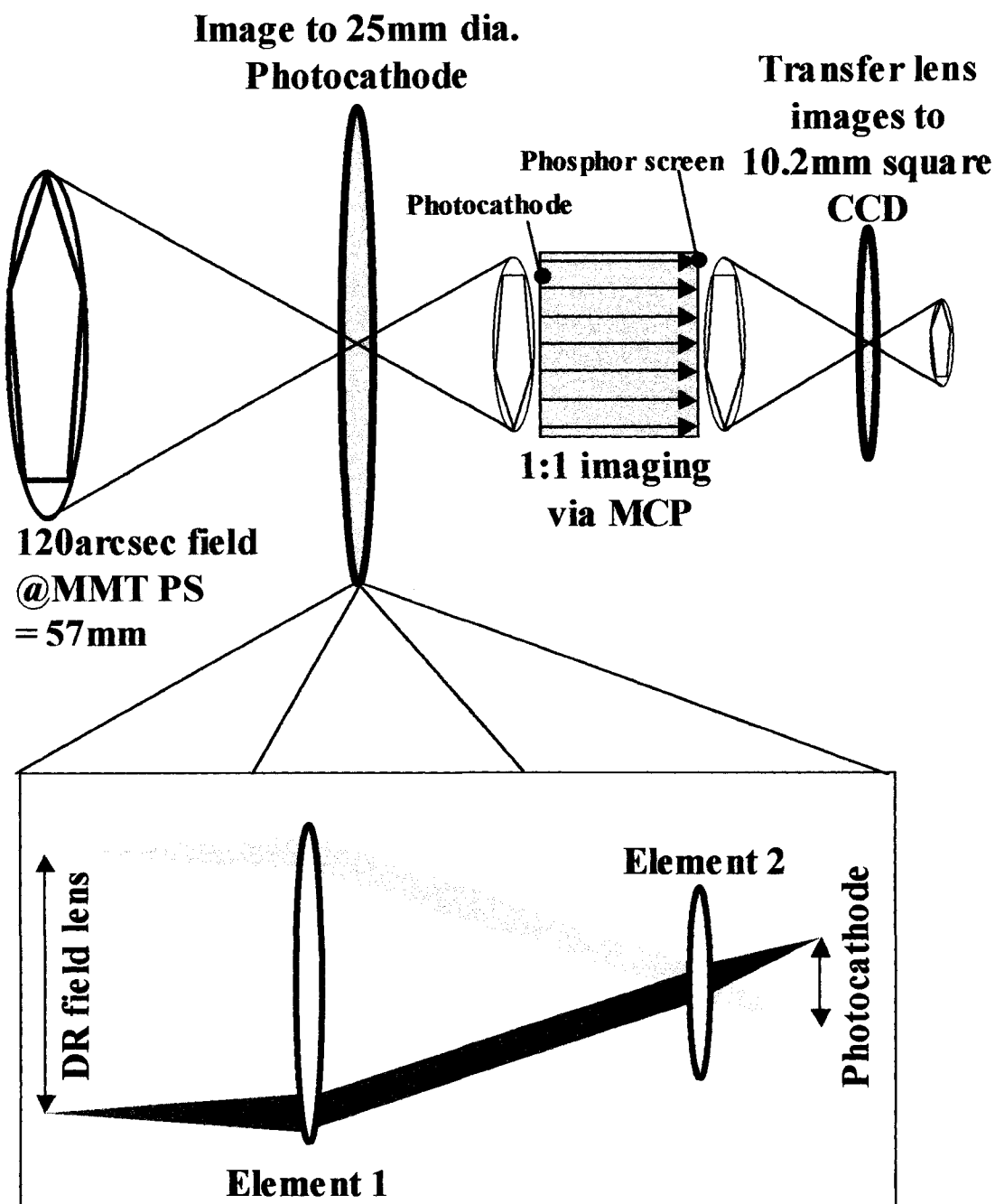


Figure 4.11 The philosophy of the gated camera optical train is shown schematically above. An optical system (broken up into two elements, see inset) reduces the image at the DR field lens onto the intensifier's photocathode. The intensifier's microchannel plate amplifies the image on the photocathode 1:1 onto the phosphor screen. A transfer lens images the phosphor screen onto a CCD.

system focal length of element 2 divided by focal length element 1. This however, is not an afocal system because this magnification of the system is not constant.

If element 2 is chosen to be a 100mm photographic lens, element 1 must be approximately a 300mm lens and of large diameter to collect all of the light from the field lens. If the test-bed is truly portable to the MMT element 1 must be 3inches plus $f/15$ divided by 300mm or nearly 4 inches. It is noted that a 100mm diameter lens with focal length 300 is a hard lens to purchase off the shelf.

The transfer lens that images the phosphor screen onto the CCD must accomplish the seemingly pedestrian task of a 2:1 imager. However, since the object for this lens is a phosphor screen, the lens must be fairly large and rather close to the screen to collect a reasonable amount of light. The close distance requires this element to be well corrected.

4.4.2 DESIGN AND EXPECTED RESULTS

Given the philosophy stated in the last section along with constraints of physical size and affordability, off-the-shelf photographic lenses were considered for element 2 and the transfer lens.

On the mountain adjustments resulted in the design presented in figure 4.12, which is the evolution of a previous design modified for use with the gated camera. Basically this system was the result of “coming up with something that works” on the mountain. It is however noticed that it is very close to the philosophy presented thus far. Element 1 of figure 4.14 is two 600mm elements operating together as approximately a 330mm lens. In figure 4.15, these are the two elements immediately following the pierced mirror to the right (separated by 135mm). The 100mm photographic lens focuses the light onto the photocathode. Knowing that the 330mm effective element does not exactly collimate the light a demagnification slightly different than 3.3 is expected. Both the data (the image of the field lens is about 23mm on the photocathode) and the Zemax model indicate a demagnification value of 3.0, which is near what was outlined in section 4.4.1.

The Zemax model also predicts that the addition of the two 600mm adds no noticeable aberration to the system. It is further assumed that the 100mm photographic lens introduces no noticeable aberrations. This means that the performance outlined in figures 4.6 and 4.11 (when properly scaled) should be nearly identical to the performance at the photocathode.

4.4.3 MMT TEST-BED ALIGNMENT

The alignment of the MMT test-bed picks up where §4.3.3.6 leaves off. As a reminder, the system was left in a state where it was mimicking the northernmost beacon (spot 1 in

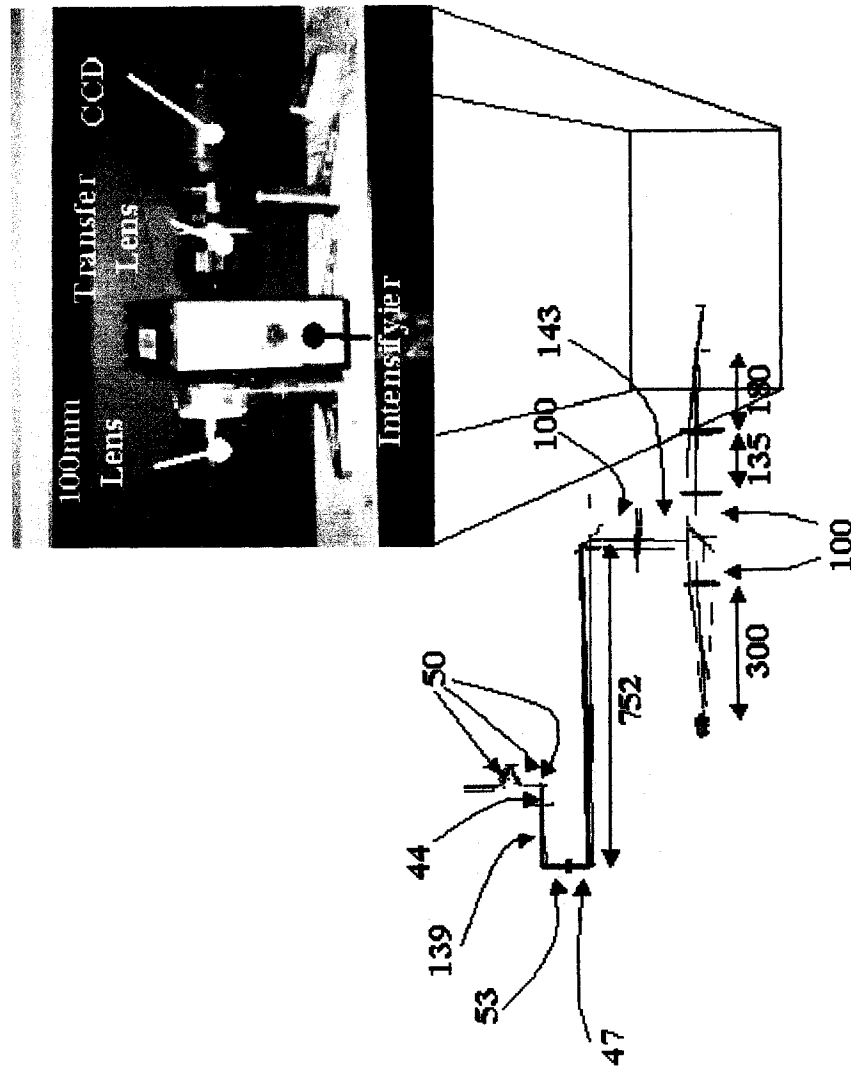


Figure 4.12 The receive optics for the 61" DR experiment are shown above. The distances between the elements are shown to the 1mm accuracy in which they are assumed to be aligned. The inset shows the detail of gated camera system that was outline in figure 4.11.

figure 4.5) at 25 km. In this case both the incoming and outgoing light come to a sharp focus at the DR field lens on a 120arcsec circle centered on the MMT optical axis.

For the MMT test bed, the alignment light is off-axis. The two 600mm lenses are put in the system by placing them at their respective locations drawn on the breadboard (indicated in figure 4.12). Because of the large diameter of the lenses, their tilts are controlled by eye. The IAL is viewed on a vertical target before and after the placement of the lenses. The fact that IAL should stay in the same vertical plane allows control of the lenses' translation.

The 100mm photographic lens is placed in the system using a similar method. The intensifier is then placed after the 100mm lens. The lights are turned out and a small amount of illumination is placed on the field lens. The intensifier is then aligned by looking at the image on the phosphor screen (by eye) until the field lens is centered and in focus.

The transfer lens is a 35mm photographic lens. It is aligned so that the circular image of the phosphor screen is fully circumscribed within the CCD chip (figure 4.13). The transfer lens is fine focused so that the ion events produced by the intensifier are as in sharp focus as possible on the CCD. To further reduce aberrations the transfer lens is

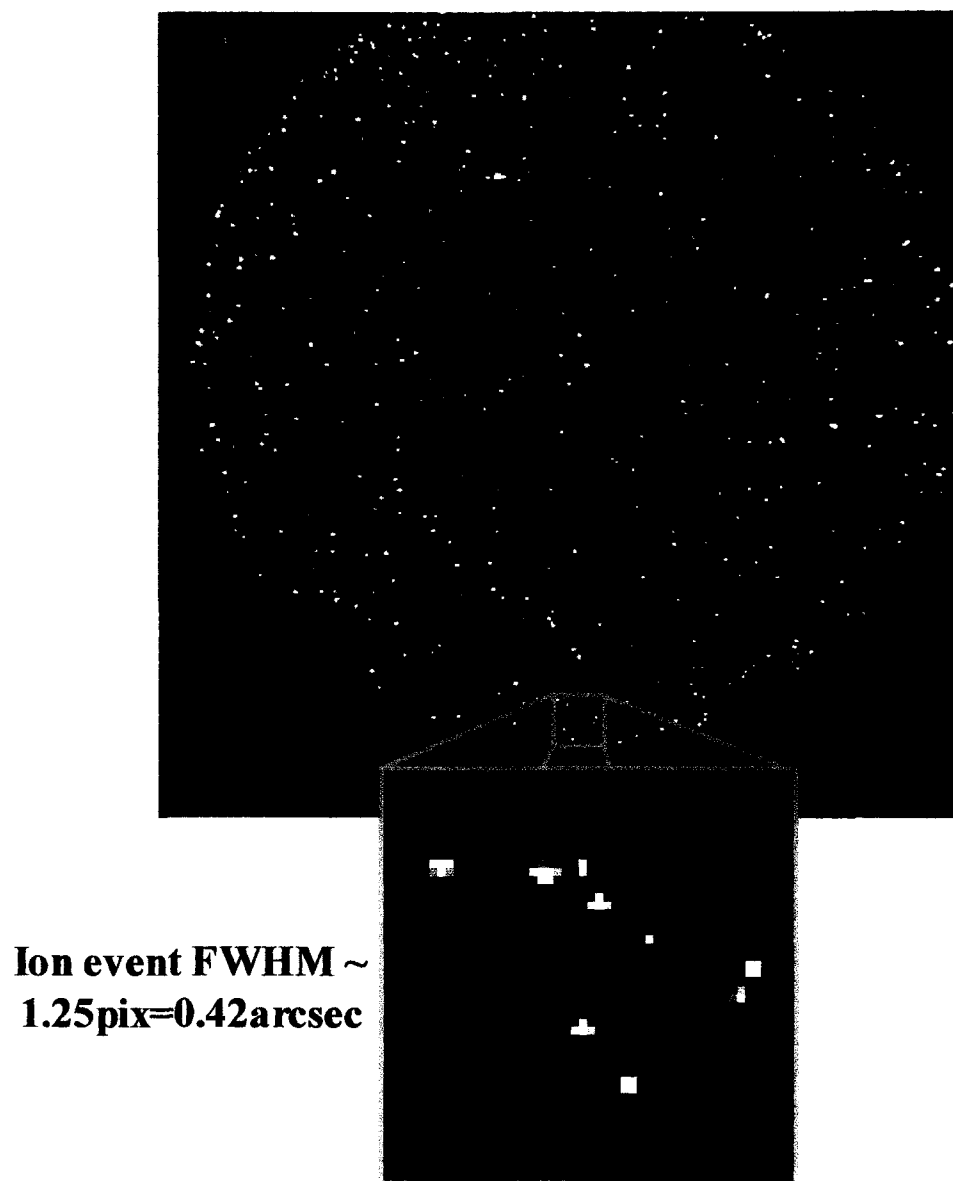


Figure 4.13 Shown above are the ion events produced by the intensifier that are imaged on to the CCD by the transfer lens. The inset is a magnified portion of this image. The PSF of the intensifier is less than $\frac{1}{2}$ arcsec.

stopped down two stops to $f/2.8$. The results are ion events with a size 0.42arcsec . This spot size is assumed to be the PSF of the intensifier transfer lens combination.

The 100mm lens is fine tuned by focusing until a sharp image of the field lens falls on the CCD.

4.4.4 CONTRIBUTION TO TOTAL ERROR

A result similar to that of figure 4.10 is achieved when the IAL passes through the entire converter box – MMT DR system – gated camera system. The result shown in figure 4.14 was obtained on a different day than figure 4.10. The degradation resulting in going through the gated camera system is seen to be minimal. The spots remain larger than the geometrical predicted results, but they remain almost a factor of two smaller than the expected size of a Rayleigh beacon in double pass. This figure represents the total PSF of the receive and DR optics.

4.5 BEAM PROJECTOR

Up to this point in the chapter, most of the discussion has surrounded the receive optics, this section will describe the send optics. The beam projector, BP, for use on the 61” was designed around two basic components: the laser, a Lightwave Electronics Q201-HD laser head and an $f/5$ parabolic 10inch diameter mirror.

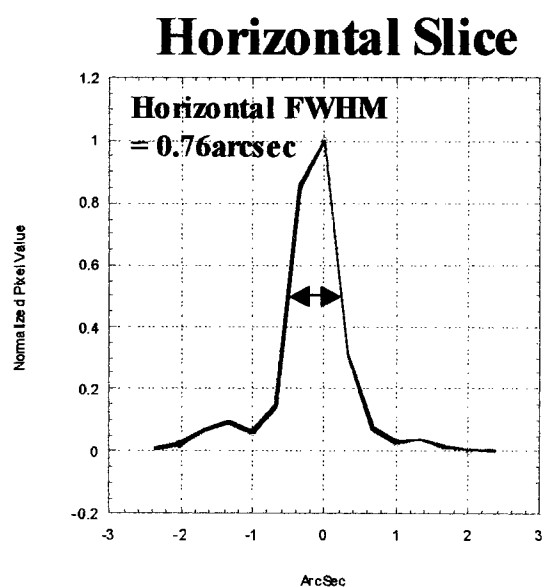
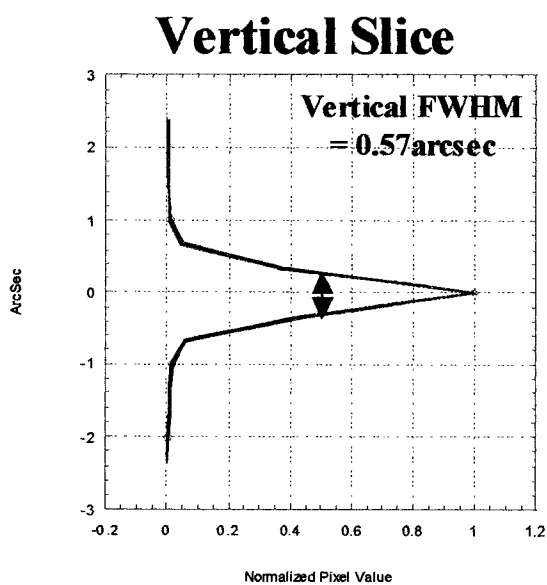
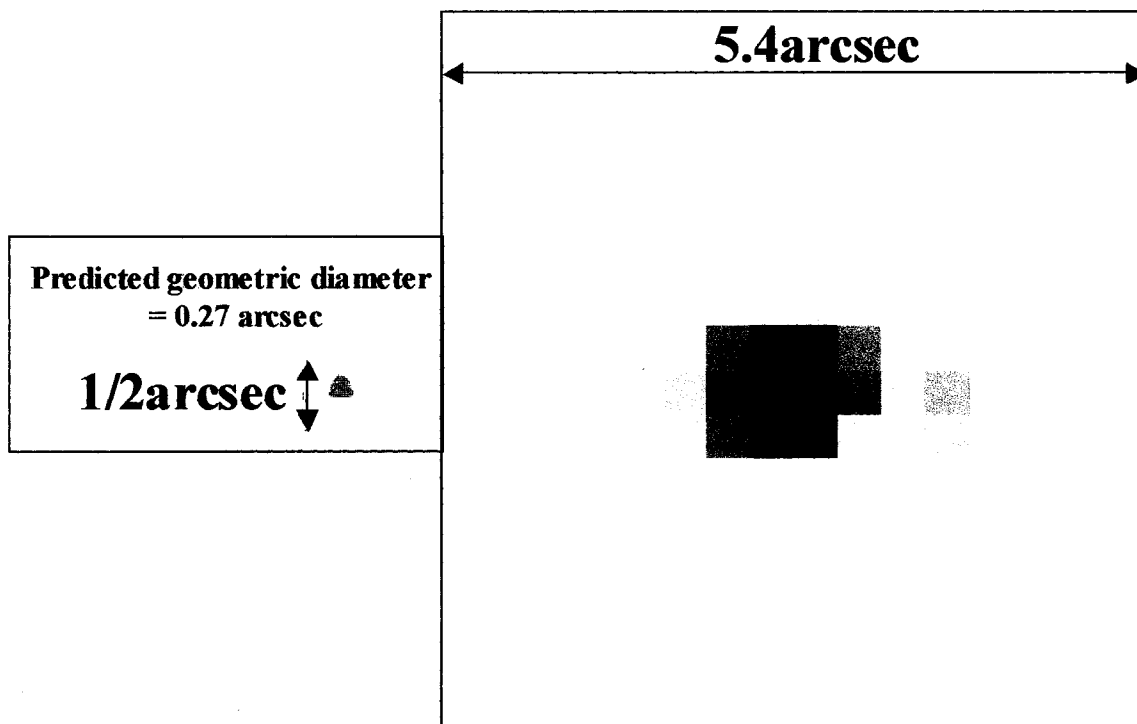


Figure 4.14 The result of imaging the IAL through the entire alignment optics, converter optics, DR optics and gated camera image train of the 61" DR experiment. In comparison to figure 4.10, there is little degradation of the image.

The laser head is specified to yield a 15ns (2.25m) pulse at 5kHz and operate at >12.5W average power. It is quoted to operate in the TEM₀₀ mode with a beam waist ($1/e^2$) diameter of 350 μ m (50cm from beam exit), to have an M² of 1.2 and to display a full angle beam divergence of 2.4mrad. These parameters were used in the design and modeling of the beam projector.

This section, as well as the section 4.6, will report on work done by Tom Stalcup, a fellow CAAO graduate student. I hope that the manner in which I present Tom's work displays my understanding of his part of the project as it pertains to the system engineering of the overall experiment. It is not my intention to take credit for any work that he has done, only to present it as the integral part of proving DR that it was.

4.5.1 DESIGN PHILOSOPHY

The optical constraint for the beam projector was that it produce a <1arcsec beacon spot over the range of 20-30km. In the geometric limit, if the beam is considered to be collimated through 30km, then a 97mm (3.8inch) spot subtends 1arcsec at 20km. The BP design is then reduced to creating a suitable collimated beam, which could be done by using the f/5 parabolic mirror as a collimating primary mirror. A well-corrected set of optics that produce an approximately f/15 beam with a focus coincident to the primary's infinity focal plane will produce such a collimated beam, figure 4.15.

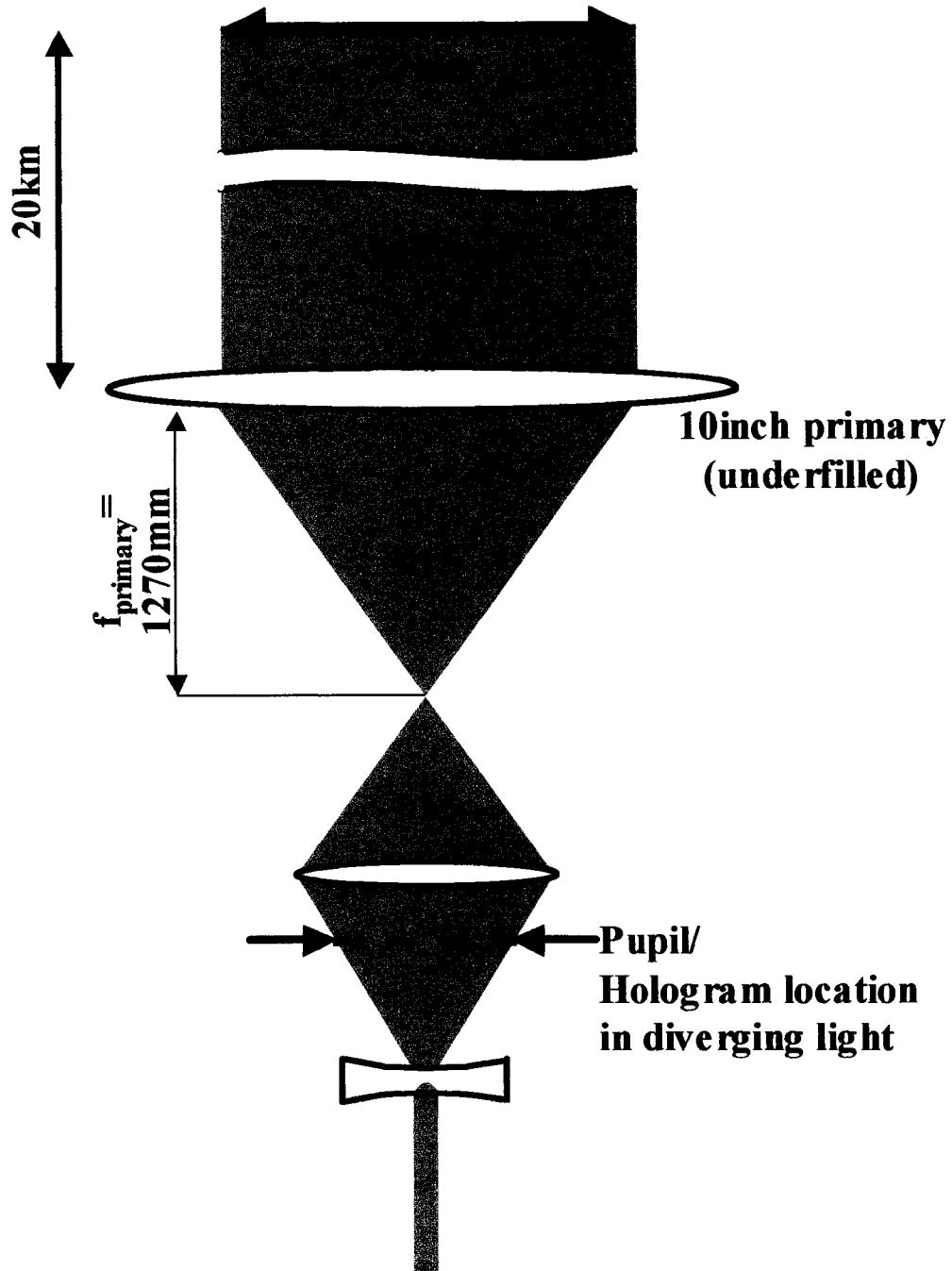


Figure 4.15 The schematic design for the BP in the geometric limit is shown above. If a perfectly collimated beam could be produced, a 97mm diameter beam would subtend 1arcsec at 20km. Also shown in this figure is a pupil/hologram in diverging light, this allows tuning of the beacon diameter on the sky.

If the rising collimated beam is considered to be Gaussian, then the problem is extended to adding enough phase at the primary to place a suitable beam waist at a given position on the sky.

A further design consideration is the ability to produce five Rayleigh beacons. A phase hologram could be manufactured to produce these five beacons which, in order to reduce its physical size, could be placed at any pupil in the BP. It is further noted that if the pupil, and therefore the hologram was in converging or diverging light, the hologram may be moved along the optical axis to fine tune the beacon separation (see figure 4.15).

4.5.2 BEAM PROJECTOR DESIGN

The optical performance of the Lightwave laser along with first-order geometrical and Gaussian optical constraints presented above were placed into Zemax. An optical layout similar to figure 4.15 was entered and Zemax was allowed to optimize to produce beacon images that were <1 arcsec over the 20-30km range. One by one, the Zemax optimized components were replaced with off-the-shelf components. After each replacement Zemax was re-optimized. This was done iteratively until all optical components in the system were off-the-shelf components. The resulting design is shown in figure 4.16. It is important to note that the optical elements had to meet the optical performance required as well as meet the power requirements of the laser.

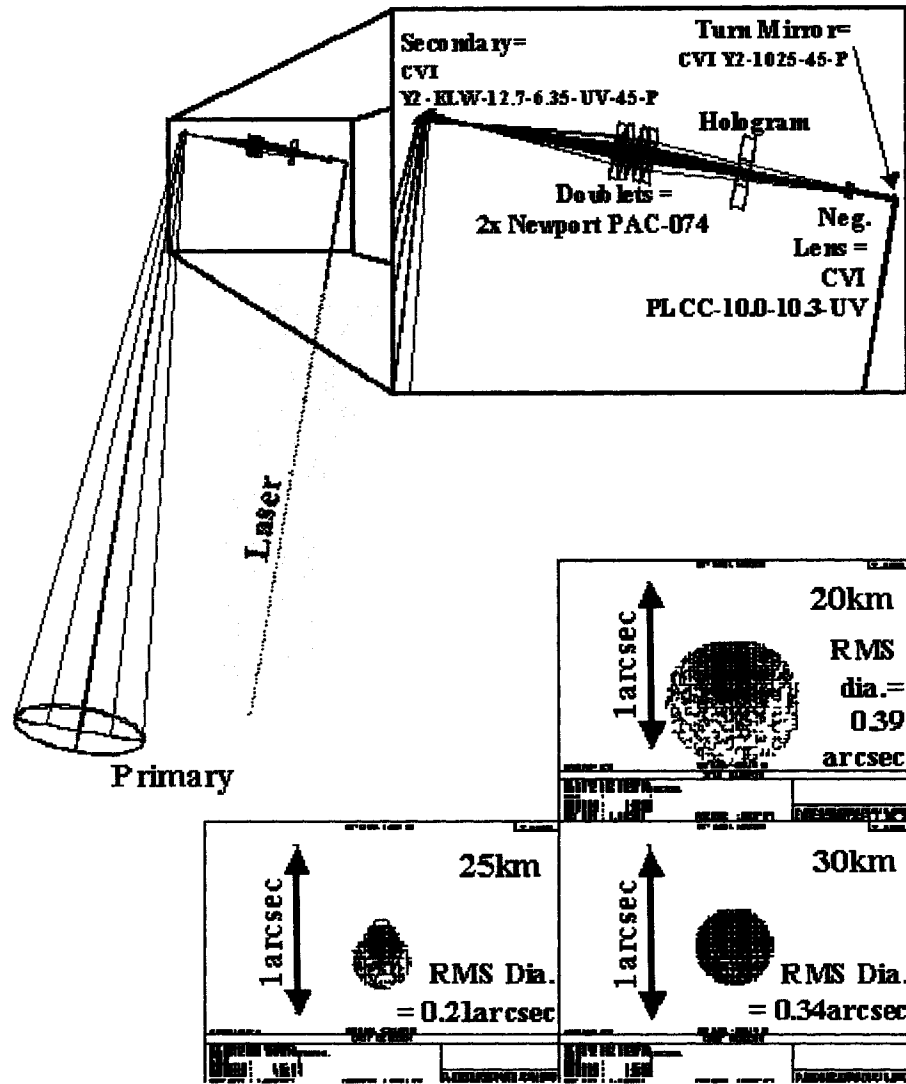


Figure 4.16 The 61" BP design is shown above with all of the optical components labeled. The inset at the top of the figure is detail of the major optical components. The performance of the beam projector is shown at the bottom of the figure.

With the optical design in place, the magnification between the hologram placement and its image on the primary mirror was calculated. Knowing this magnification allowed the five beacon phase hologram to be calculated. The phase hologram was manufactured by Reverse Scientific and Technical Company, Novosibirsk, Russia; on the recommendation of Jim Burge.

The final design and performance of the BP is shown in figure 4.16. Since the beam projector is an axially symmetric system, it is expected that all beacons will behave equally. The spot diagrams shown are for the 60arcsec radius produced by the hologram (modeled as a diffraction grating in Zemax) at 20, 25 and 30km have RMS diameters of 0.39, 0.21 and 0.34arcsec respectively. Using the Gaussian beam propagation function in Zemax, the $1/e^2$ diameters are 0.8, 0.79 and 0.85arcsec. If the geometric and Gaussian performance results are root-sum-squared the result would be a less than 1arcsec beacon, meeting the design criteria.

4.5.3 BEAM PROJECTOR ALIGNMENT

The alignment of the BP optics are described by what was first done in the lab at Steward Observatory and then what was done onsite at Mt. Bigelow.

4.5.3.1 IN THE LAB

The relative tilt and decenter tolerance of the doublets, shown in figure 4.16, is tight. A custom lens cell was constructed to appropriately hold these lenses. After the lenses were placed in the cell the back reflection/forward image technique outlined in section 4.3.3.1 was used to check their alignment. It was also noted that one could see circular fringes when looking at the cell.

The doublet cell and negative lens are mounted on a single assembly so that only one element needs to be placed in the BP at the mountain. To align this assembly the following steps were taken.

The height of the center of the secondary was measured along with the height of the horizontal platform that supports the cell/lens assembly. The difference of these heights gives the beam height above the platform. In the lab a laser is shown so that its beam is at this constant height above an optical table. Two irises are then firmly placed on an aluminum plate with their apertures centered on this beam. This iris assembly will be used to align the BP on the mountain.

The iris assembly is removed and the lens cell, on a duplicated aluminum plate, is placed in the laser path. The lens cell is aligned on the plate using the previously discussed back

reflection/ forward image technique. The negative lens is placed on the plate and the alignment process is repeated to position this lens in translation and tip/tilt.

The lenses' specifications (given by the manufacturer) and geometric measurements (of the cell and negative lens holder) allowed the following separations to be computed: the distance between the cell and the doublet vertex as well as the distance between the negative lens' vertex and its holder. The correct cell to holder distance was then calculated, and an internal micrometer was used to set the separation of the two holders. The two elements were then firmly clamped to their aluminum plate so that the assembly may be treated as a single unit.

4.5.3.2 ON THE MOUNTAIN

On the mountain, the BP alignment takes similar steps as the converter box alignment.

The beam projector optics are supported by a wooden box that also supports the Lightwave laser. This wooden box is clamped to the 61" yoke 95inches (2.4m) from the telescope's optical axis. The ideal distance is defined as 1, which approximately 75mm (3inches) away from the actual location.

The Lightwave laser is then bolted to BP box. The box is shipped with the secondary and primary in place; requiring only the placement of the one turn mirror (figure 4.16). To accomplish this, the iris assembly discussed in the last section is placed on the horizontal platform. The iris assembly is tilted and translated along with the turn mirror until the Lightwave laser beam hits the center of the turn mirror, passes through both irises and hits the center of the secondary mirror.

The secondary mirror is tipped and tilted to aim the laser beam to the geometric center of the primary. The primary is then tipped and tilted to aim the laser beam back at the secondary. Fine-tuning is accomplished by further tipping and tilting the primary until the reflected laser beam returns to the laser's entrance aperture. At this point, the BP mirrors are considered squared.

The iris assembly is replaced by the doublet/negative lens assembly on the horizontal platform. The assembly is aligned by use of the back reflection/ forward image method. The horizontal platform on which the assembly is placed has linear stage that allows it translation along the optical axis.

To complete the BP alignment, the hologram is placed between the lenses (as shown in figure 4.16). A large flat mirror is placed on the top of the BP box and tuned so that the

reflected light returns to the laser aperture. The horizontal platform's translation stage is then adjusted to auto-collimate the BP.

The hologram is aligned by looking at the beacons on the sky with the native 61", i.e. through no DR optics. The hologram is translated parallel to the optical axis until spots 3 and 4 (figure 4.5) are $(2 \times 60 \times \sin(36^\circ) =) 70.5 \text{ arcsec}$ apart, which is 353 $20 \mu\text{m}$ pixels at the 61" plate scale (10 arcsec/mm). A fold mirror, which was later found to be rather astigmatic, allowed the light to bypass the experimental optics and image the beacons at the 61" plate scale (figure 4.17). Rotation of the hologram allows the beacons to be placed on the correct pierced mirrors and be imaged through the entire DR system, an example of this is also shown in figure 4.17.

Focusing of the beam projector may be done by imaging the beacon with the range-gated camera around 25km and translating the doublet/negative lens assembly. One does this until the beacon image is as sharp as possible. As a caution, this must be done after it is insured that the DR optics are focused at 25km independently of the telescope and that the telescope places an infinity image where prescribed by the design presented in figure 4.12.

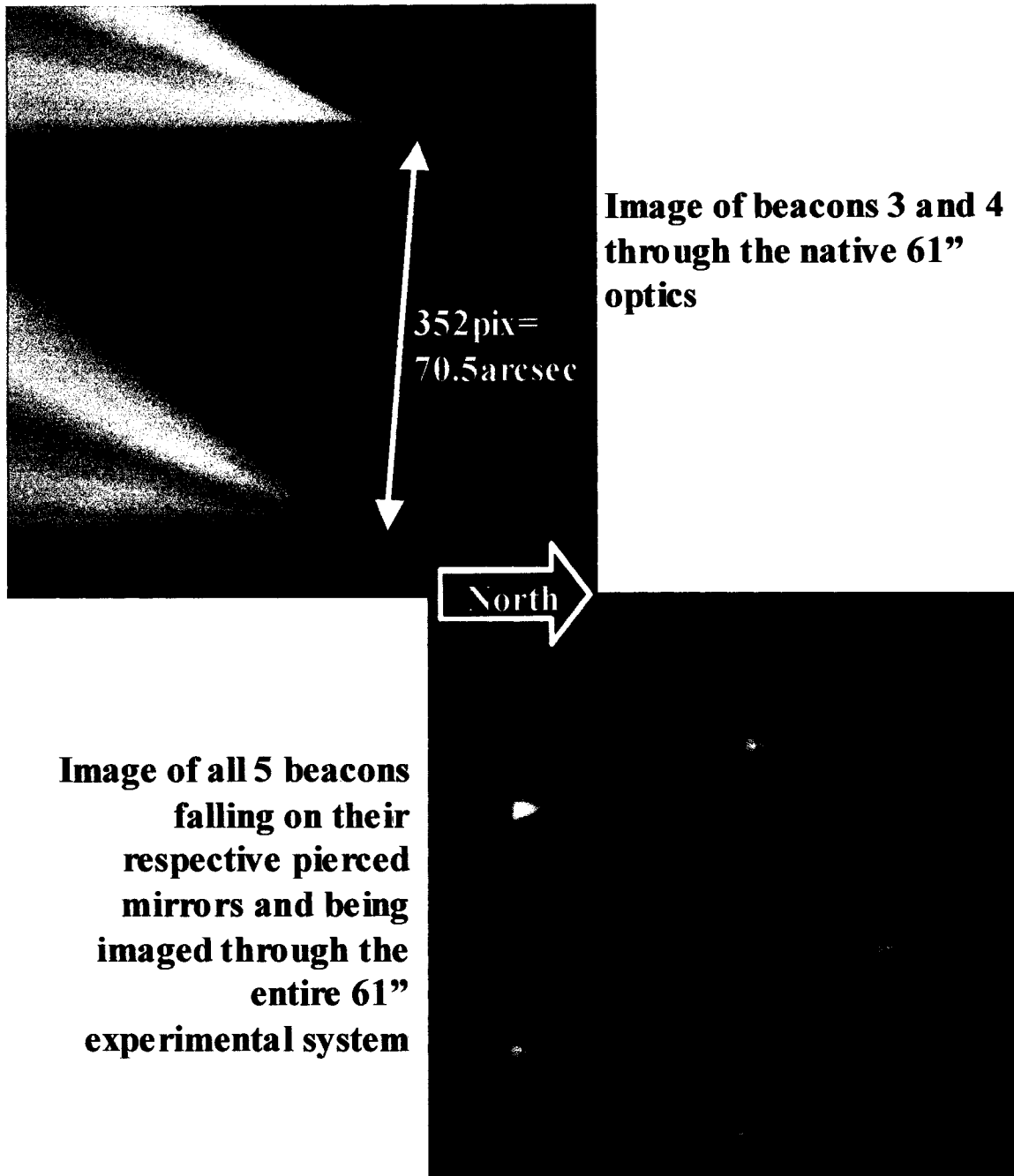


Figure 4.17 The alignment of the Rayleigh beacons on the sky. The top image shows spots 3 and 4 (figure 4.5) imaged at the 61" plate scale, this is done to align the beacons in magnification on the sky. The bottom image shows all five beacons being imaged through the entire 61" experiment optical train, this is done to align the beacons in rotation on the sky.

4.5.4 CONTRIBUTION TO TOTAL ERROR

To this point, sections of this type have included a laboratory measurement of the PSF of the subsystem. In the case of the beam projector, using a sky image is not useful because the beacon is convolved with atmospheric seeing. A laboratory measurement was made, however sub-pixel resolution would be required to make an accurate estimate of the BP PSF. So it will be assumed that the PSF is nominally the constraint value of 1arcsec.

4.6 CONTROL ELECTRONICS AND SOFTWARE

If chapter 4 is read as a temporal “how to”, then at this point all of the optical and mechanical components of the system are aligned and ready to run. This section will focus on the control electronics and software, which, in this active system tells each dynamic component when (and how) to perform its task.

Again, as in section 4.5, it is necessary to state that the work reported on in this section was done almost entirely by Tom Stalcup, a fellow CAAO graduate student. It is my intention to present his work, not as my own, but as a part of the experiment we worked on as part of a group. It is my hope to present his work from a system engineering level, and show how the experiment is governed and optically affected by the electronics’ subsystems.

4.6.1 DESIGN PHILOSOPHY

The basic philosophy of the control electronics (for the sake of brevity, it is assumed that the term electronics includes the software) has been outlined in section 4.2. The electronics have two main functions: to keep the ringer running at its resonance frequency with the desired amplitude, and to send timed pulses to the necessary subsystems.

In order to streamline the experiment, to begin to make it a usable “black box”, effort was made to create an easy and straightforward user interface. Emphasis was also placed on centralizing the control, reducing the number of subsystems and creating a less esoteric system. These goals led to the use of LabVIEW software and a PC to control the necessary subsystems. A high level explanation of the electronics is given in the next section.

4.6.2 DESIGN AND EXPECTED RESULTS

The system architecture is shown in figure 4.18. The PC is the governing element. It has three I/O possibilities, a USB port, a DAQ board with both analog and digital I/O and a GPIB interface.

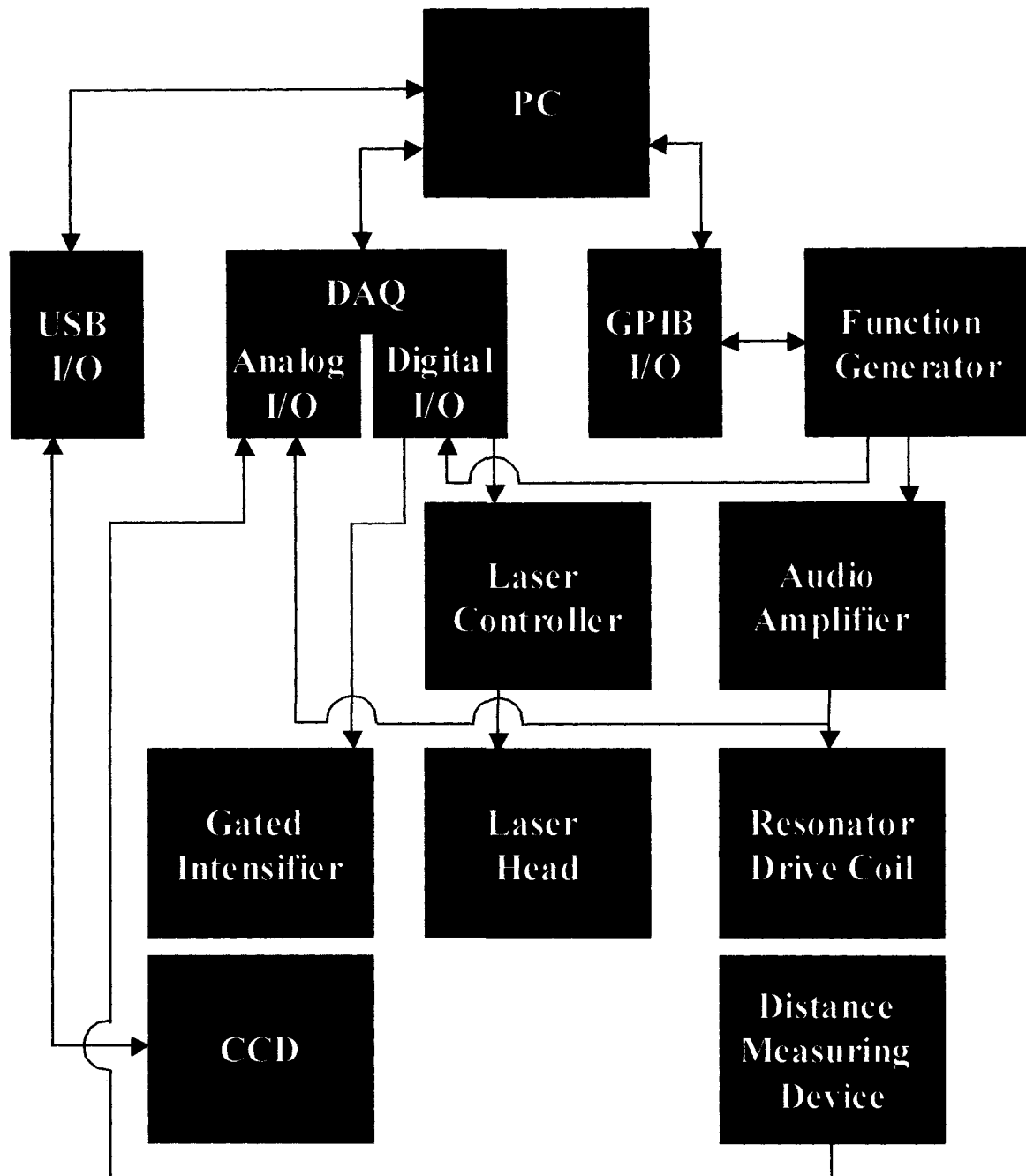


Figure 4.18 The system architecture of the 61" experiment control electronics is shown above.

The USB port is the hub that controls the data to and from the SBIG CCD camera. The software package that runs the CCD is the Apogee distributed Maxim DL.

A SuperLogics PCI-PD2-MF-16-1M/12L DAQ card serves as the analog and digital I/O hub. An input to this hub is the analog signal from the optical distance measuring device, DMD. This device is a Micro-Epsilon optoNCDT 1605 and has a measured gain of 2.2 mV/ μm at 5kHz. The DMD is aligned to view the hypotenuse of a 45degree right angle prism that is epoxyed to the side of the resonator about 1inch from the DR mirror vertex (figure 4.19). The hypotenuse of the prism has a slope equal to one, therefore any axial motion of the resonator is translated 1:1 to vertical position viewed by the DMD. The DMD then produces an output equal to the measured distance multiplied by its gain. When the resonator is running the DMD sends a sinusoidal, resonance signal to the analog input; this serves as the input to the software PLL running in LabVIEW on the PC.

The other input to the analog I/O hub monitors the drive signal being sent to the resonator. The PLL running in LabVIEW takes advantage of a program that allows the triggering, like an oscilloscope, of an electronic signal. The PLL program triggers off the drive signal, it then computes the average phase difference resonance (DMD) signal. This phase difference is used to calculate a modified drive signal frequency that is sent to the function generator.

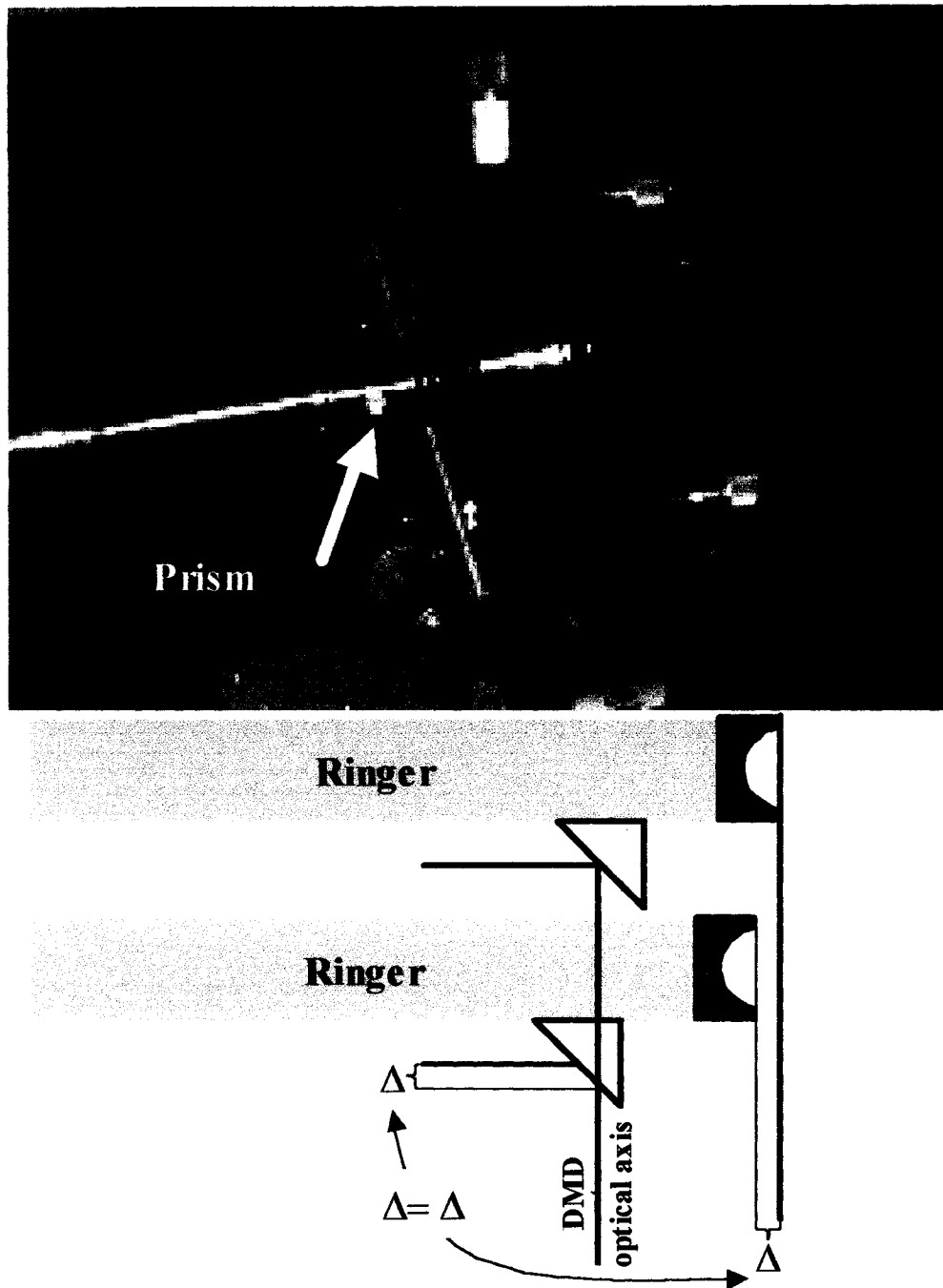


Figure 4.19 The prism epoxyed to the ringer that is used as a pick-up for the DMD is shown above. The DMD views the hypotenuse of a 45 degree prism, therefore any horizontal displacement of the ringer is registered as vertical displacement by the DMD.

The modified drive frequency is sent to the Agilent/HP 33120A 15MHz arbitrary waveform function generator via the GPIB hub. The function generator is controlled to within 1/1,000 of a Hertz. The amplitude of the resonator is also monitored by the DMD. The desired amplitude of the ringer is set by the user as an input to the LabVIEW PLL program. The actual amplitude of the ringer is the result of a sinusoidal signal produced by the function generator amplified by an audio amplifier and applied to the resonator drive coil. The PLL program determines the correct amplitude of the sine wave produced by the function generator. A feedback loop in the PLL program averages the last 4 amplitudes read by the DMD and accordingly adjusts the amplitude sent to the function generator.

The only input to the digital I/O hub is a sync signal from the function generator. This signal acts as the reference for the digital delays discussed in the next paragraph.

The digital I/O hub has two outputs. The LabVIEW PLL program accepts user inputs for camera trigger and laser phase delay. For a review of the delay terminology refer to the paragraph following equation (2.13). The delays are calculated and passed to counters operating at 1MHz (giving $\pm 1\mu\text{s}$ or $\pm 150\text{m}$ accuracy on the sky). The signal sent to the laser controller triggers the laser to fire a user-defined time from the mirror's sinusoidal

zero crossing, the laser delay. The DR mirror's conjugate position when the laser is fired is defined to be zero km.

The signal sent to the intensifier is a negative going pulse that begins at user-inputted start height (converted to time) from the laser firing (zero height) and ends at the user-inputted end height. This pulse turns the intensifier gain on; in this state the intensifier operates like an open shutter, as described in section 4.4. When the intensifier is not receiving the negative going pulse, it does not produce an image and may be considered to be in the closed shutter state. A timing diagram is shown in figure 4.20.

4.6.3 ALIGNMENT

Section 4.6 has described the electronics and software, which in the spirit of the previous alignment sections, does not need to be "aligned". However, I will take advantage of this space and describe the DMD alignment and the physical placement of the electronics.

The DMD is aligned so that it gives an analog signal of zero volts, is situated perpendicular to the ringer (optical axis) and places its laser spot near the geometric center of the prism.

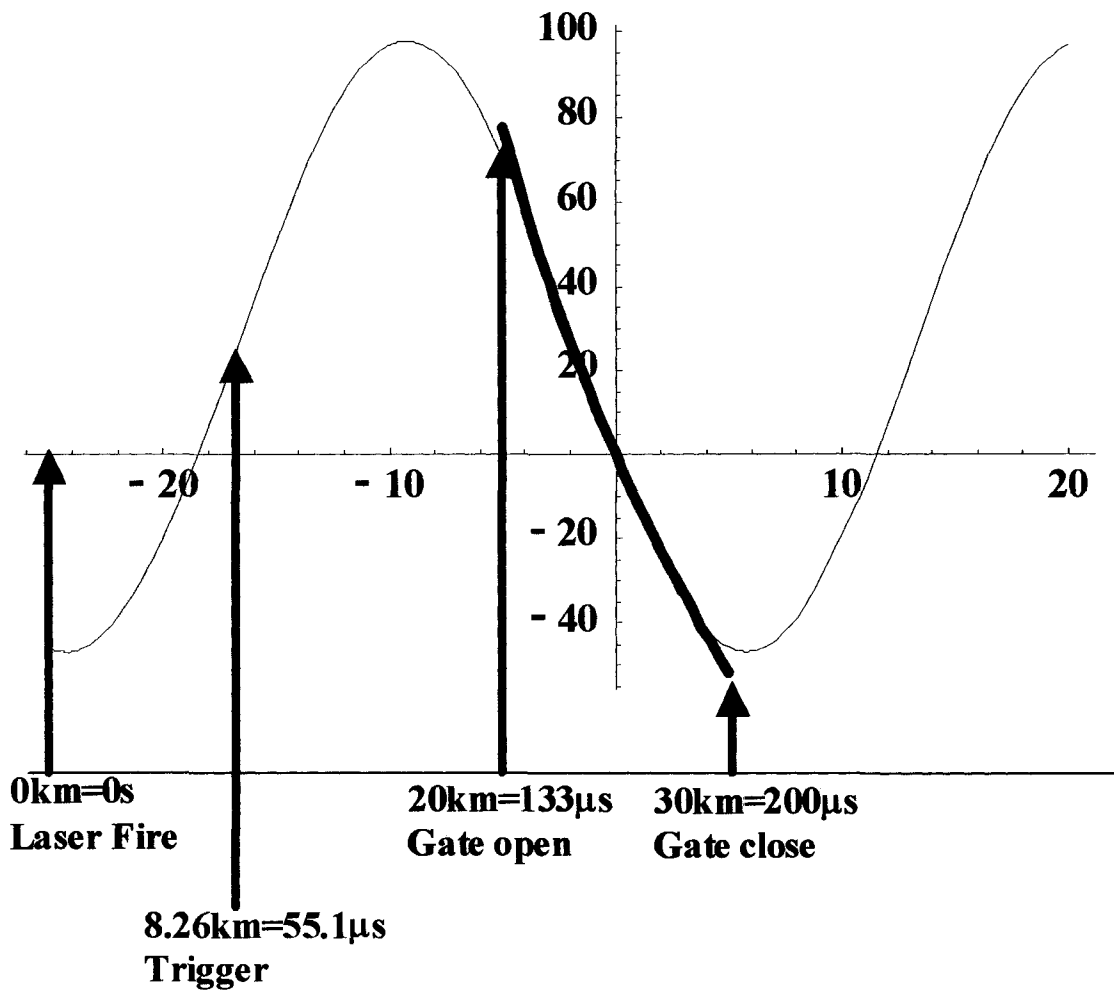


Figure 4.20 Timing diagram of the control electronics. For clarity all times are given relative to the laser firing time, =0. The trigger (sinusoidal zero crossing) occurs 55.1ms after the laser firing or (200-55.1ms=) 144.9ms before it (previous period). The range gate is open between 20 and 30km.

The bulk of the electronics: the PC, function generator, audio amplifier, laser controller, and laser chiller were placed in a warm room downstairs below the telescope dome. This was done to reduce the amount of heat radiated into the dome in order to reduce seeing. Initial and subsequent alignment efforts were carried out upstairs through the use of a secondary PC monitor, mouse and keyboard.

4.6.4 CONTRIBUTION TO TOTAL ERROR

The electronics produce quantifiable errors through the: 1MHz counting card and the $\pm 1\mu\text{s}$ accuracy of the DMD [Tom Stalcup: Personal Communication, 2003]. The $\pm 1\mu\text{s}$ counter card error corresponds to an optical error via the difference in phase of when the laser is firing and when it is supposed to be firing. If this is converted a defocus term of the rising laser pulse at 20km, this can be thought of as a $\pm 150\text{m}$ error or by equation (2.9) a $\pm 0.6\mu\text{arcsec}$ error. The error of the DMD may be converted to a defocus term by means of equations (2.14), (2.16) and (2.17) and results in a blur of $83\mu\text{m}$ or 0.175arcsec on the MMT.

4.7 SUMMARY OF COMPONENT ERRORS

The summary of component errors is shown below in table 4.1

Component	Error [arcsec]
Optics (predicted)	0.5
Optics (intensifier PSF)	0.75
Beam Projector	1
Electronics (DMD)	0.25
Atmosphere up	1.5
Atmosphere down	1.5
<i>RSS total</i>	2.5

Table 4.1 This table displays the expected errors contributed by each component of the 61” DR experiment. The errors are assumed to be independent so the total root sum squared error is calculated in the last row.

The values are rounded to the nearest $\frac{1}{4}$ arcsecond value. The optics predicted value is the result of the worst performer in figure 4.6, the optics intensifier value is the PSF value from figure 4.13, the beam projector value is from section 4.5.4, the electronics value is the DMD error from section 4.6.4 and it is assumed that there is 1.5arcsec atmospheric seeing in both the up and down beams. The errors are assumed to be statistically independent and are root sum squared, RSS, for a total error of 2.5arcsec. For 1arcsec seeing the RSS total is reduced to 2.0arcsec and for 2arcsec seeing it is 3.1arcsec. These are conservatively high values especially for the intensifier optics value, which is the larger FWHM in figure 4.10 that includes errors in the alignment optics, which are not present in the 61” experiment.

CHAPTER 5 RESULTS

The results from the 61” DR experiments will be given in this chapter. Section 5.1 will give a pictorial overview of what the experiment looked like. Section 5.2 will describe the results as they compare functionally to the model described in chapter 2. Sect 5.3 will give results concerning atmospheric measurement that are a consequence of the successful proving of DR. The dissertation will end with a summary given in section 5.4.

5.1 EXPERIMENTAL OVERVIEW

Chapter 4 gave a very in depth discussion to the workings of the Mt. Bigelow 61” DR field tests. This preamble to the results will serve to show the basic set up of the experiment.

The field tests reported on in this dissertation where done to prove the MMT DR system. The MMT will use an auxiliary telescope to project five Rayleigh beacons on a 120arcsec diameter regular pentagon. The MMT DR system will dynamically refocus the beacons over the 20-30km range-gate. The Mt. Bigelow 61” telescope was configured to act as a 61” off-axis subaperture of this MMT system (chapter 4).

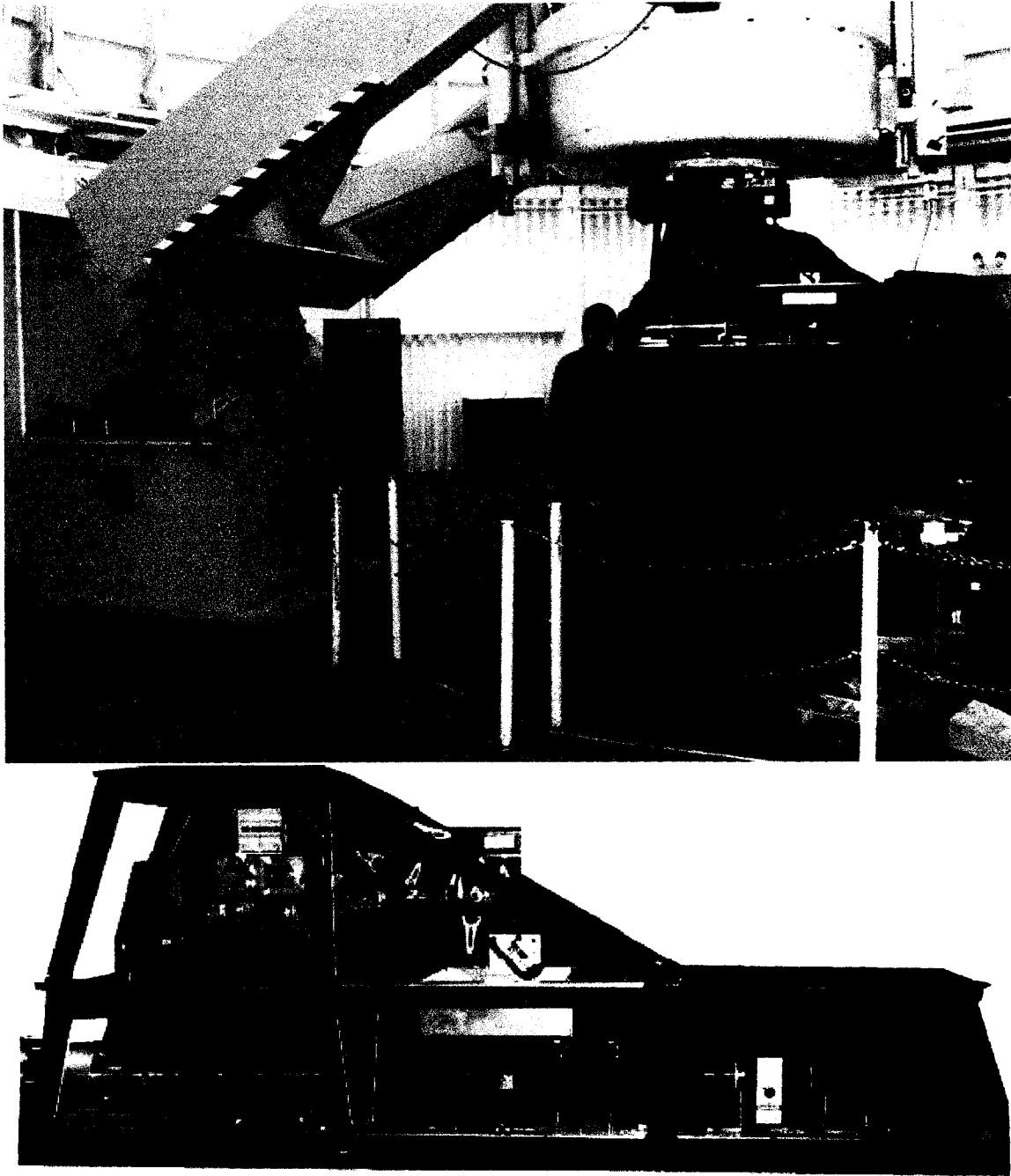


Figure 5.1 The 61" field test layout. The optics discussed in chapter 4 are shown attached to the telescope in the top image and in detail in the bottom image. A previous version of the beam projector is shown attached to the telescope yoke. The version of the projector discussed in this dissertation was placed in the same position.

The top image of figure 5.1 shows a set-up similar to the one that produced the results described in this chapter. The auxiliary beam projector (described in figure 4.16) is the black box attached to the 61” yoke. The distance from the center of the beam projector to the center of the 61” primary is approximately 2.4m, which is nearly λ (defined in figure 2.8). The optical instrument that converts the 61” to an MMT subaperture along with the dynamic refocus optics is shown attached to the telescope and in detail at the bottom of the figure (see chapter 4 for further explanation of these optics).

The beam projector, by means of a hologram, projects the five beacons on the sky (figure 5.2). The bottom left image of figure 5.2 shows the projected beacon viewed from outside the dome and the bottom right image shows the beacon viewed from within the dome. The upper image in the figure is an image of the beacons taken through a wider FOV guide telescope. It shows the beacons passing through a thin layer of clouds and impacting on a very dense layer of clouds. The higher order modes resulting from the hologram are readily seen in this image.

An aircraft spotter was present for all times that the beacons were projected into the sky. The spotter was armed with a remote kill switch that would immediately shutter the laser if a plane were in the area. Failing the kill switch, the spotter was either always within earshot or in radio contact via walkie-talkies with the DR team that had the ability to

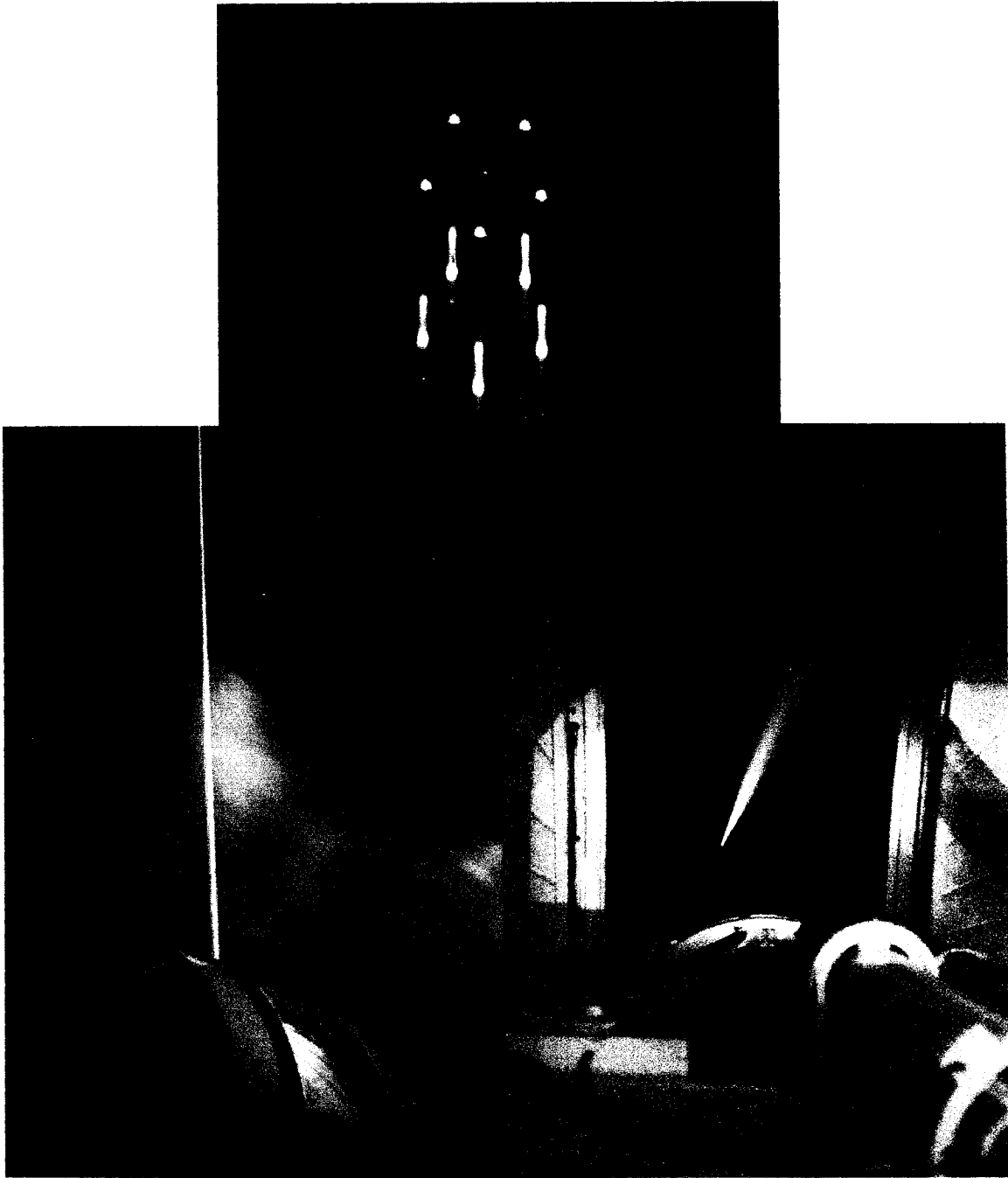


Figure 5.2 The beam projector viewed on the sky, from outside the dome and from inside the dome. The top image shows the five beacons passing through a low layer of clouds and impinging on a higher layer. The higher orders of the hologram are easily seen. The bottom two images show the projected beacons as viewed from outside and inside the dome.

instantly shutter the laser. Over the course of three runs, the spotter never reported an aircraft.

The beacons on the sky were imaged through the optics described in chapter 4 (figure 5.3). The translation of the beacons was controlled by moving the telescope in RA and declination. The beacons could be rotated on the sky by rotating the hologram.

Figure 5.3a shows the five beacons at 2:45am on 15 October 2003, with a range gate of 10-30km and a 0.5sec exposure.

Figure 5.3b is a composite image of 3sec exposures of 1km increments over the 15-30km range. These images were taken on 18 October 2003 between 4:13 and 4:20am.

Figure 5.3c is a composite image taken on 19 October 2003 at 1:35 to 1:37am. The range is over 10-30km and the individual images are over the ranges 10-12.5, 12.5-15, 15-20, 20-25 and 25-30km. Each of the images is a 0.3sec exposure.

Figure 5.3d is a 2sec exposure taken at 1:38am on 19 October 2003. The laser was triggered at 4.1Khz (instead of the normal 5kHz) in order to capture all the pulses at a height of 30-40km. Two of the five windows show saturation, this is a result of the lower

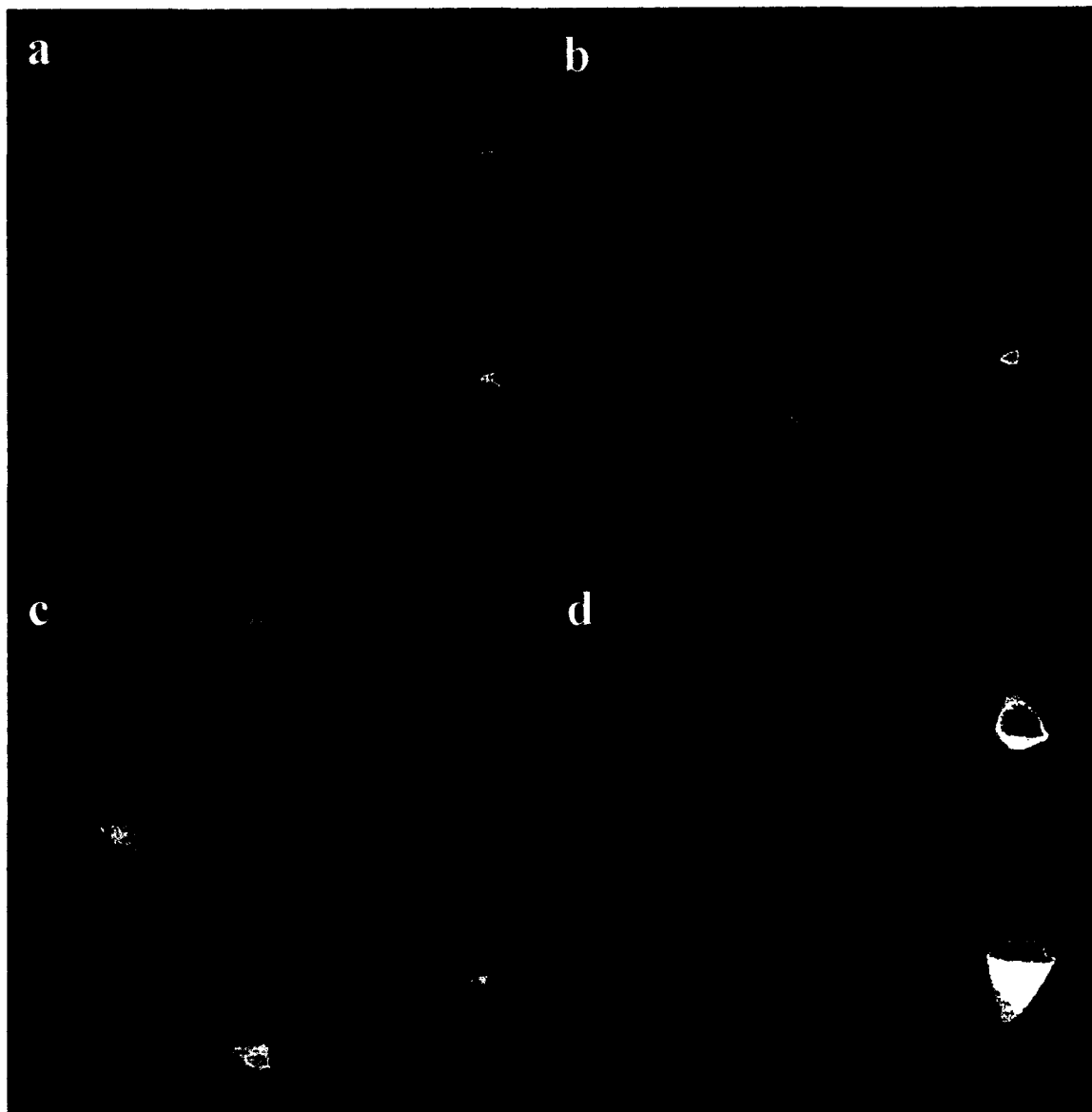


Figure 5.3 The five beacons viewed by the 61" experiment optics. The details of the images are given in the text.

altitude portion of the beacons being within the temporal and spatial field of view of the saturated window. This image is the best example of the pierced mirror's shadow.

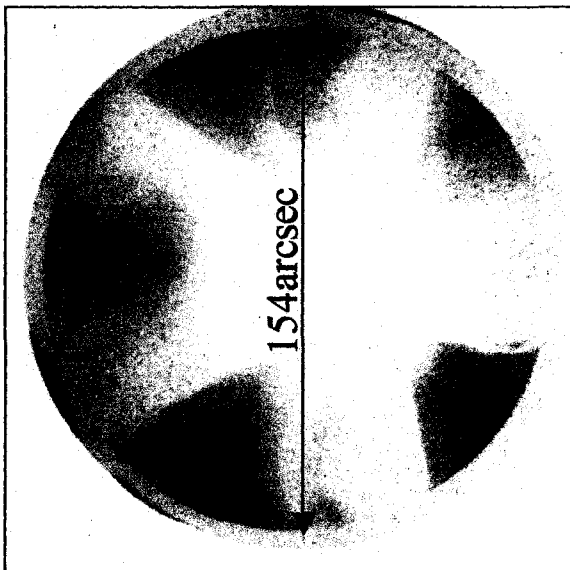
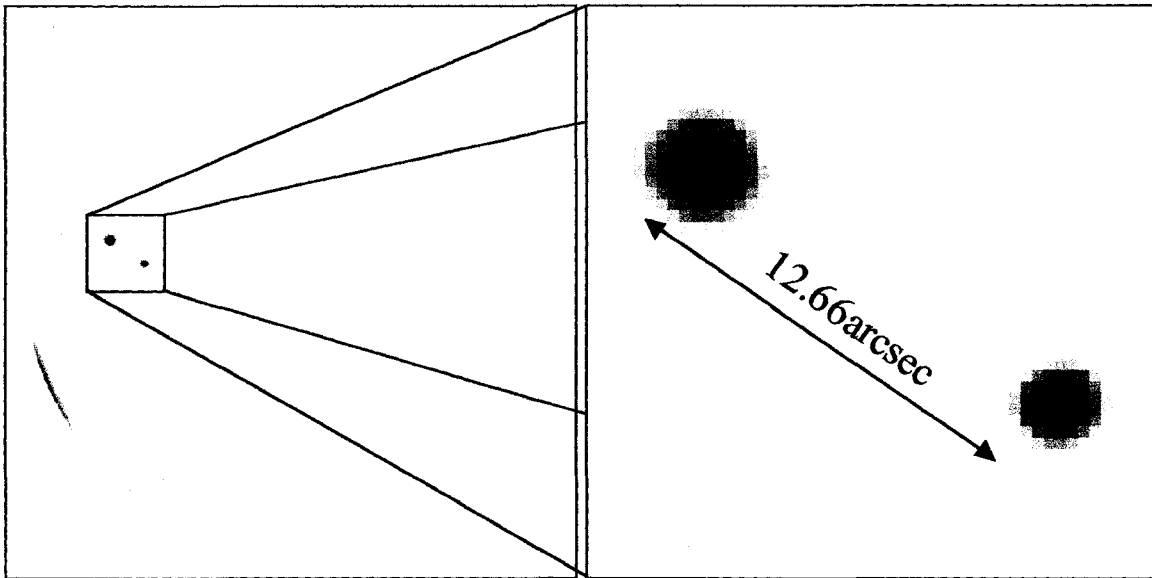
In a qualitative manner, this serves to describe what the telescope setup looked like and what was viewed through it without the DR active. The next section will discuss the DR results

5.2 DYNAMIC REFOCUS RESULTS

This section will outline the results of the 61" field test of the MMT DR system. These results are primarily from the October 13-19, 2003 DR run, mainly because this run was the most refined. Earlier DR results are reported and give a good history of the subject up to this point [Lloyd-Hart, et al., 2001; Georges, et al., 2002 & Georges, et al., 2003].

5.2.1 PLATE SCALE

The previous section showed the beacons on the sky. In order to calibrate the plate scale a binary pair was imaged (BD 36-1388). Sixty 0.2second exposures were taken and then added together to reduce noise and give a strong estimate of the stars' centroids (figure 5.4). The star catalog reported their separation at 12.66arcsec. The stars' centroid positions were measured with the image processing feature of the Maxim software



Star catalog (BD 36-1388):

$\Delta\text{Ra}: 0.6\text{secs}=9\text{arcsec}$

$\Delta\text{Dec}: 8.9\text{arcsec}$

Therefore,

separation= 12.66arcsec

Centroid

separation= 37.48pix

Therefore,

platescale= 0.338arcsec/pix

Figure 5.4 The image of a binary used to calibrate the experiment's plate scale. The lower image shows the plate scale of the DR field lens' clear aperture.

giving a measured separation of 37.48pixels. This yields a plate scale of 0.338arcsec/pixel. To calibrate other images, mainly the video data presented in section 5.3, the clear aperture of the DR field lens was measure to be 456 pixels or 154arcsecs. It is possible to use this as a calibration source in other data because the optics preceding the DR field lens where not changed over the investigated period.

5.2.2 DYNAMIC REFOCUS GUI

As described in section 4.6 the DR experiment was governed by using a PC running LabVIEW and the image acquisition software. The LabVIEW graphical user interface, GUI, (figure 5.5) would display the current ringer resonance frequency and the sinusoidal peak-to-peak amplitude. The laser fire time and range gate would be shown with respect to the resonator amplitude. The GUI allows user inputs for commanded amplitude [μm], amplitude limit [μm], laser start delay [μs], range gate start height [km] and range gate end height [km]. It allows the user to enter a frequency [Hz] that the program begins when seeking the phase locked frequency. The start voltage input is the voltage that initially fed to the function generator. The other main features of use are an indicator that states whether the LabVIEW program is phased locked or not (it states “unlocked in the figure”) as well as the on (“dynamic refocus”) and off (“stop”) buttons.

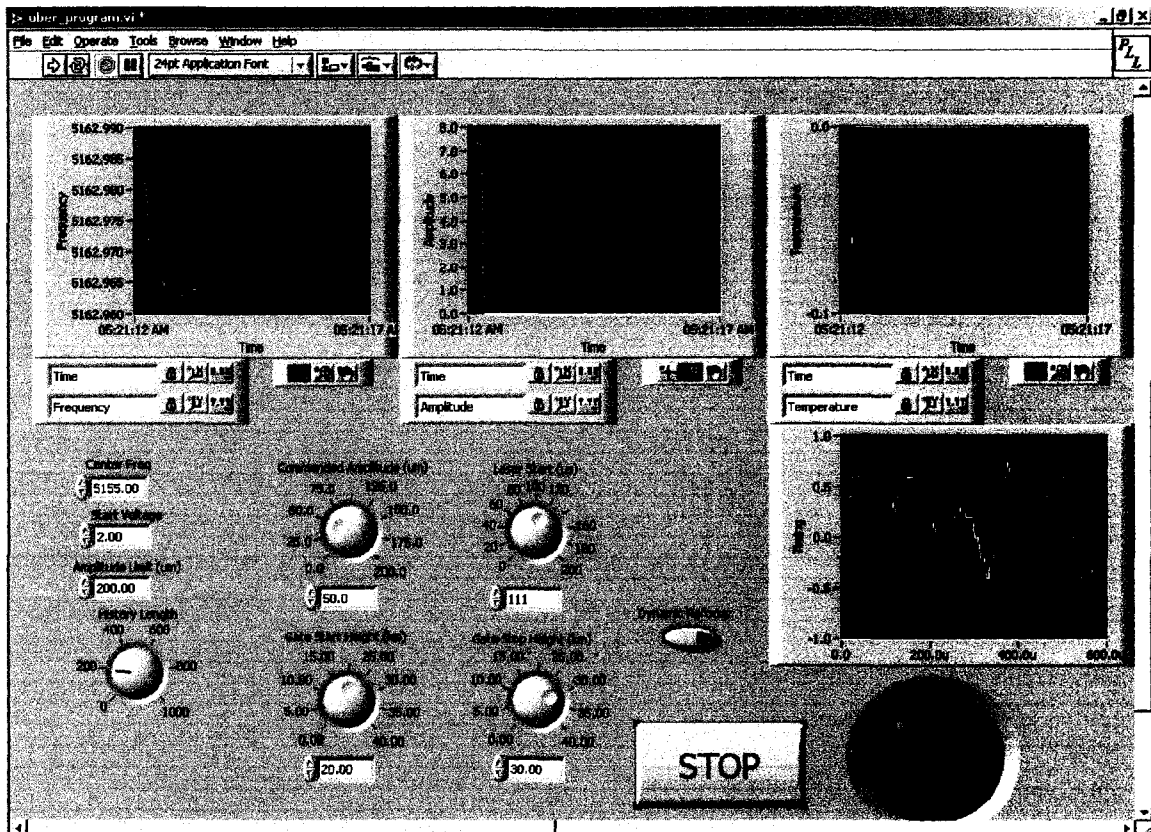


Figure 5.5 The LabVIEW GUI. Detailed explanation of the GUI is given in the text. It should be noted that the values shown in the figure are not necessarily representative of the values used or acquired during the experiment.

For the October experiments when DR was operational for 20-30km the usual values where approximately:

- Center Frequency = 5160Hz
- Commanded Amplitude = 100 μ m
- Laser Start = 111 μ s

The discrepancy of the commanded amplitude that was inputted and the value we expected (160 μ m) is most likely a function of how the distance measuring device, DMD, was viewing the prism. Secondary effects may include the calibration of the DMD, the distance the prism was from the mirror (motion decreases as this distance is increased) as well as the atmospheric seeing. The above values are only representative to images that the atmosphere allows us to discern.

5.2.3 DYNAMIC REFOCUS RESULTS

Using the GUI values of the last section and the set-up described in chapter 4 and section 5.1, three good nights of DR data where taken, October 15th, 18th and 19th, 2003. The nights of the 16th and 17th where spent examining a small amount of astigmatism present in the telescope and atmospheric seeing. Over the course of these few days, seeing seemed to be between 1.5 and 2arcsecs.

From these three nights, a few examples have been selected to show the effect of dynamic refocus on a Rayleigh Beacon 20 to 30km above the telescope (which is at an elevation of 2,510m). The first two examples (figures 5.6&5.7 and 5.9&5.10) show some of the best results that we received, corresponding to 2.7arcsec FWHM DR spots. The last example (figures 5.11&5.12) corresponds to a composite set of data that when averaged has a larger FWHM (3arcsec) but because of lower noise in the composite image matches the model outlined in chapter 2 extremely well.

5.2.3.1 RESULTS: 18 OCTOBER 2003, 4:27AM

Figures 5.6 and 5.7 show data taken on 18 October 2003 at 4:27am. In figure 5.6, the full 173arcsec “off” and “on” fields are shown as the lower left and right images respectively. The upper 33.8arcsec images show the detail of one of the spots. These detailed images are placed on the same color scale. For all of the images the range gate is 20-30km and the exposure time was 0.5sec. The vertical FWHM for the “off” case is 2.7arcsec and the horizontal FWHM is 7.0arcsec. The FWHM for the “on” case is 2.7arcsec.

Figure 5.7 compares the same spots detailed in the previous figure with a result of the model discussed in chapter 2. The model uses a 2.7arcsec FWHM Gaussian kernel. For the pictorial comparison in the upper left of the figure, the data and model have nearly identical color stretches.

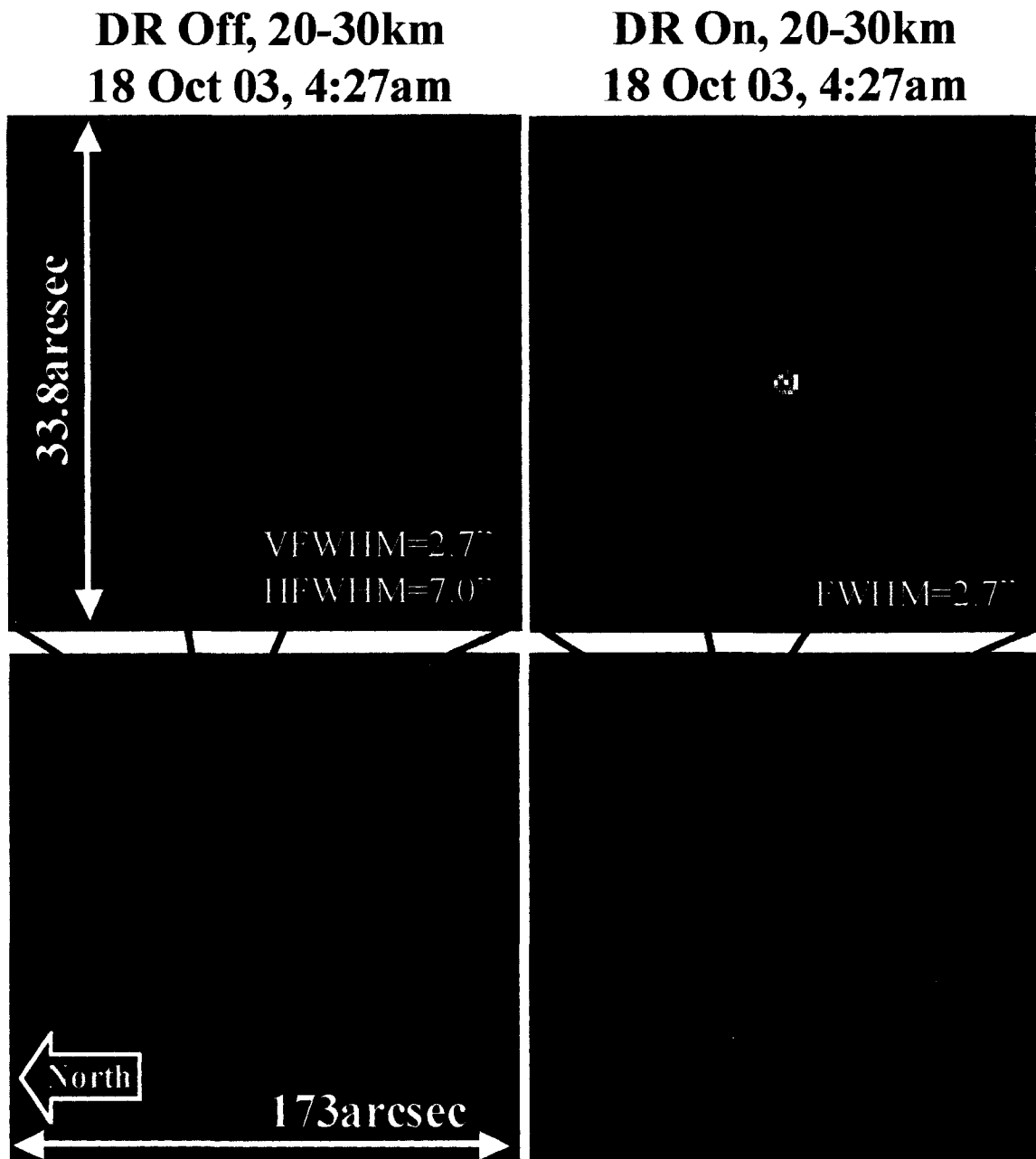


Figure 5.6 DR off and on results from 18 October 2003 at 4:27am.

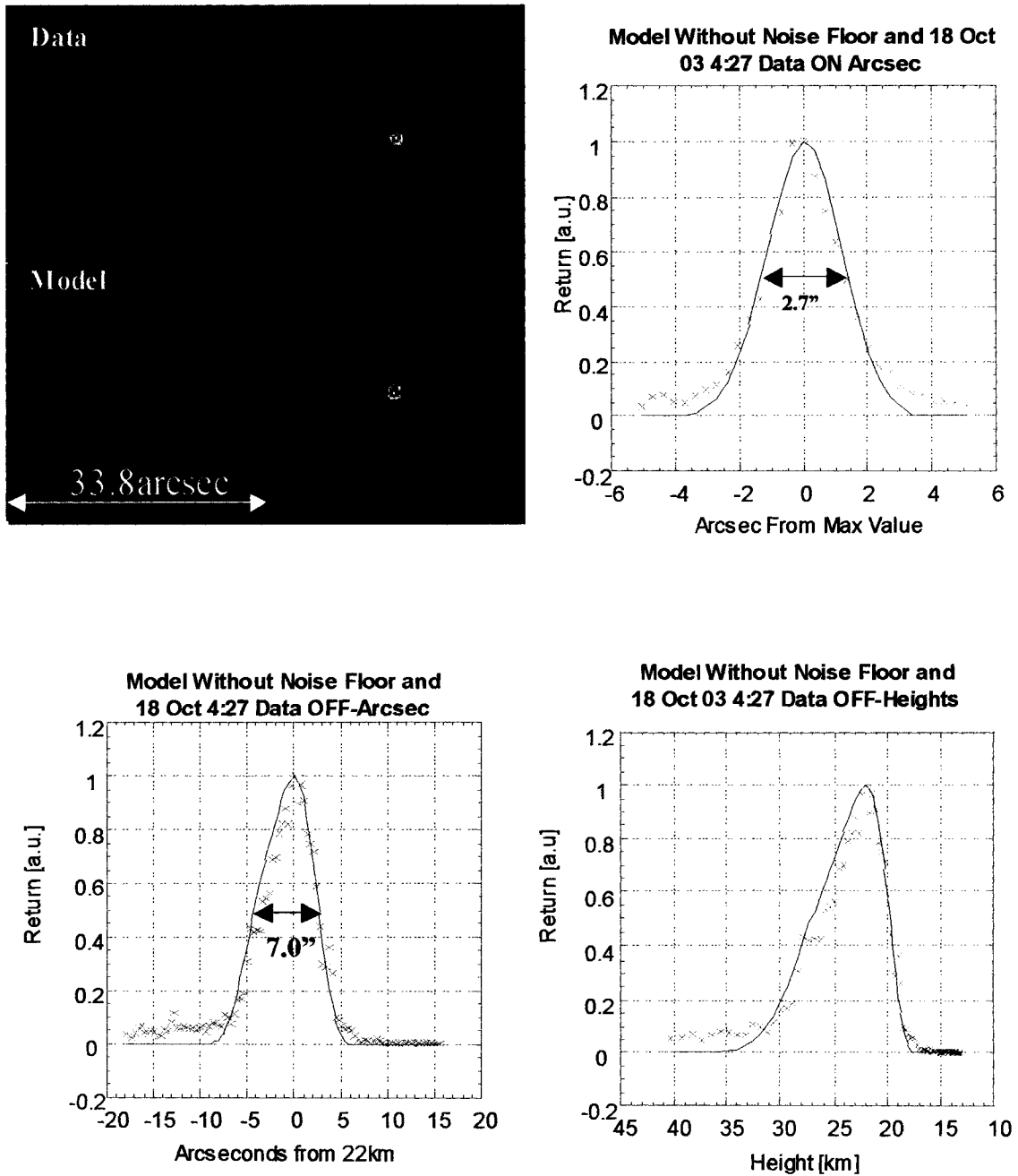


Figure 5.7 Comparison of the model with 2.7arcsec FWHM blur and the 18 October 2003, 4:27am data. The upper left cluster of images qualitatively make the comparison using the same color stretch. The graphs compare horizontal slices across the data and the model. The lower right graph stretches the “off” data in terms of height.

The graphs in figure 5.7 correspond to a horizontal slice taken through the center of the information in the images. In the upper right graph corresponding to the DR “on” case, a noise floor was added to the model while the maximum was kept at a value of one arbitrary unit (a.u.). The data (red x’s) was placed to best fit the model (solid blue line). With the 2.7arcsec FWHM assumption there is good agreement between the data and the model.

The lower graphs are both horizontal slices through the “off” case. The graph on the lower left shows the model and the data graphed versus arcseconds from the maximum value. The model states that the maximum value of the slice occurs at almost exactly 22km. The lower right graph stretches the “off” case as a function of height. This graph has the higher heights on the left to correspond to the images in the upper left and in the previous figure. The height graph shows two strong features of the data, the sharp turn-on at 20km that is due to the range-gate and the exponential decay at the higher heights that is due to the lessening Rayleigh backscatter.

Figure 5.8 shows the DR “on” result of the previous two figures compared to an image of unresolved star that taken about a half-hour prior. The star image was taken through a 3nm wide filter centered at 532nm and a red blocking filter in order to reduce chromatic aberration. The star image has a much longer exposure than the DR image as such it is assumed that the PSF due to the intensifier is averaged out, thus giving a reasonable value

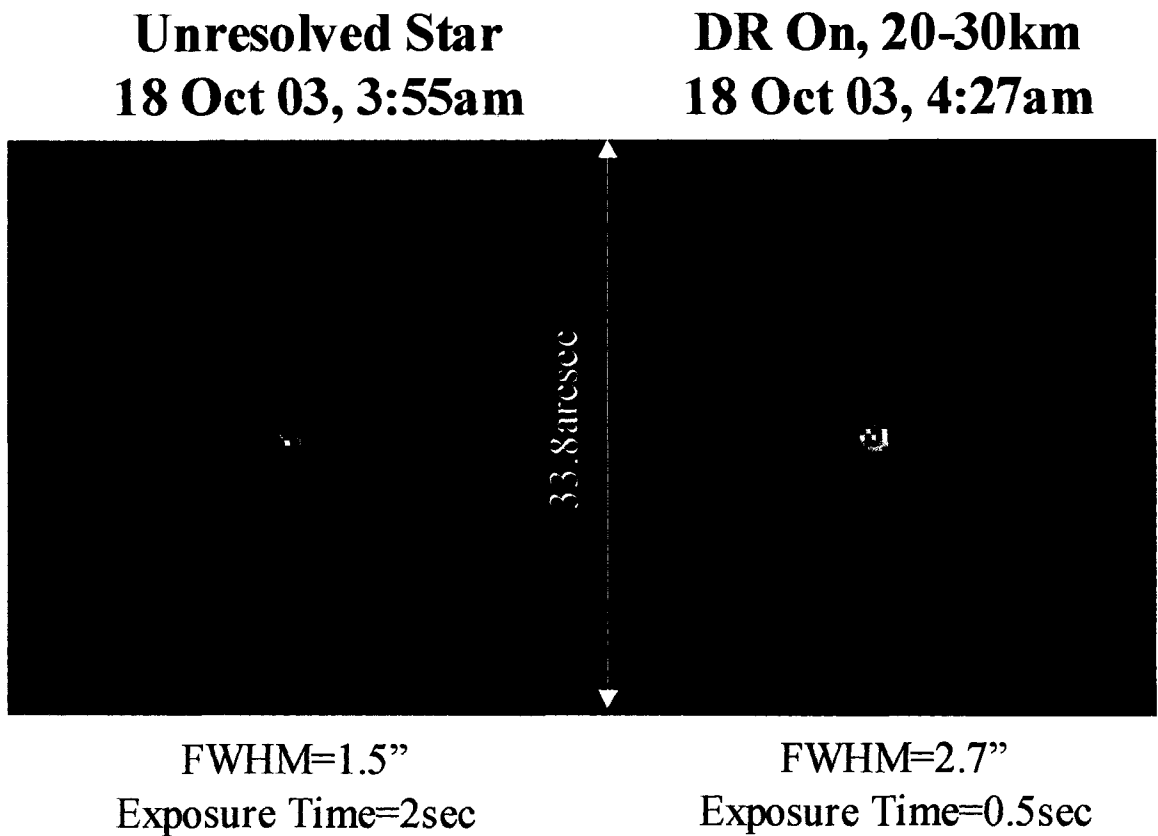


Figure 5.8 Comparison of a long star exposure to the shorter exposure DR "on" case for 18 October 2003 at 4:27am. The star image was taken on the same day about a half hour prior.

for the seeing. This being the case, there is agreement within 10% with table 4.1. The discrepancy may easily be explained by the temporal difference between when the images were taken.

5.2.3.2 RESULTS: 15 OCTOBER 2003, 2:46AM

Analogous to figures 5.6 and 5.7 are figures 5.9 and 5.10. The data in the latter figures was taken on 15 October 2003 at 2:46am and has an “on” FWHM of 2.7arcsec. The data was imaged with an exposure time of 0.5sec.

5.2.3.3 RESULTS: 18 OCTOBER 2003, 4:13-4:30AM

Figures 5.11 and 5.12 are again analogous to figures 5.6 and 5.7 as well as 5.9 and 5.10. The data in figures 5.11 and 5.12 is different from the previous data sets. It represents the composite of a result of a series of four exposures taken between 4:13-4:30am on 18 October 2003 and added together. The result is an image that is more blurred than those in figures 5.6 and 5.7, which is a member of the set. However, the noise is averaged out and there is greater agreement with the model.

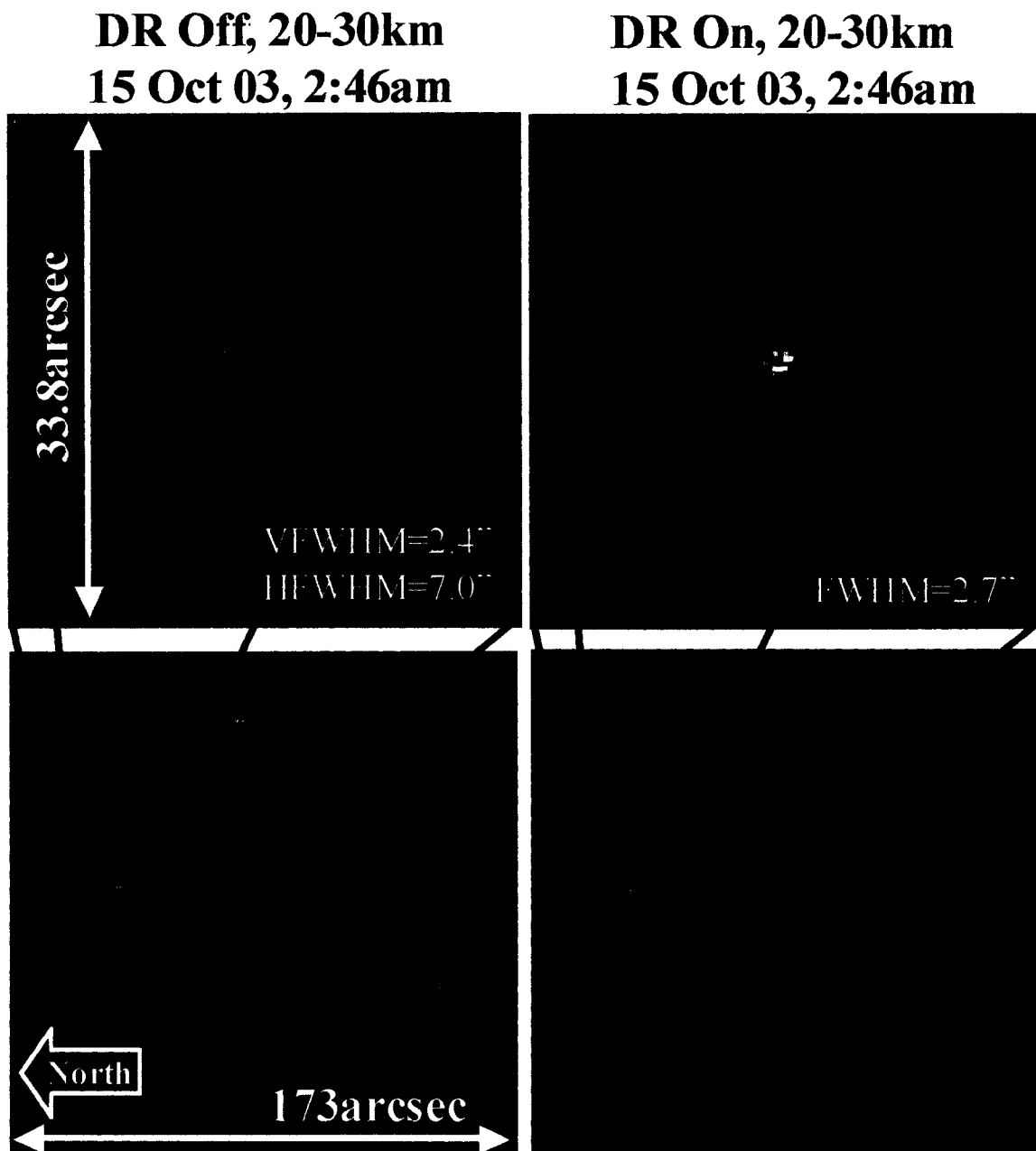


Figure 5.9 15 October 2003, 2:46am data. This above is analogous to figure 5.6.

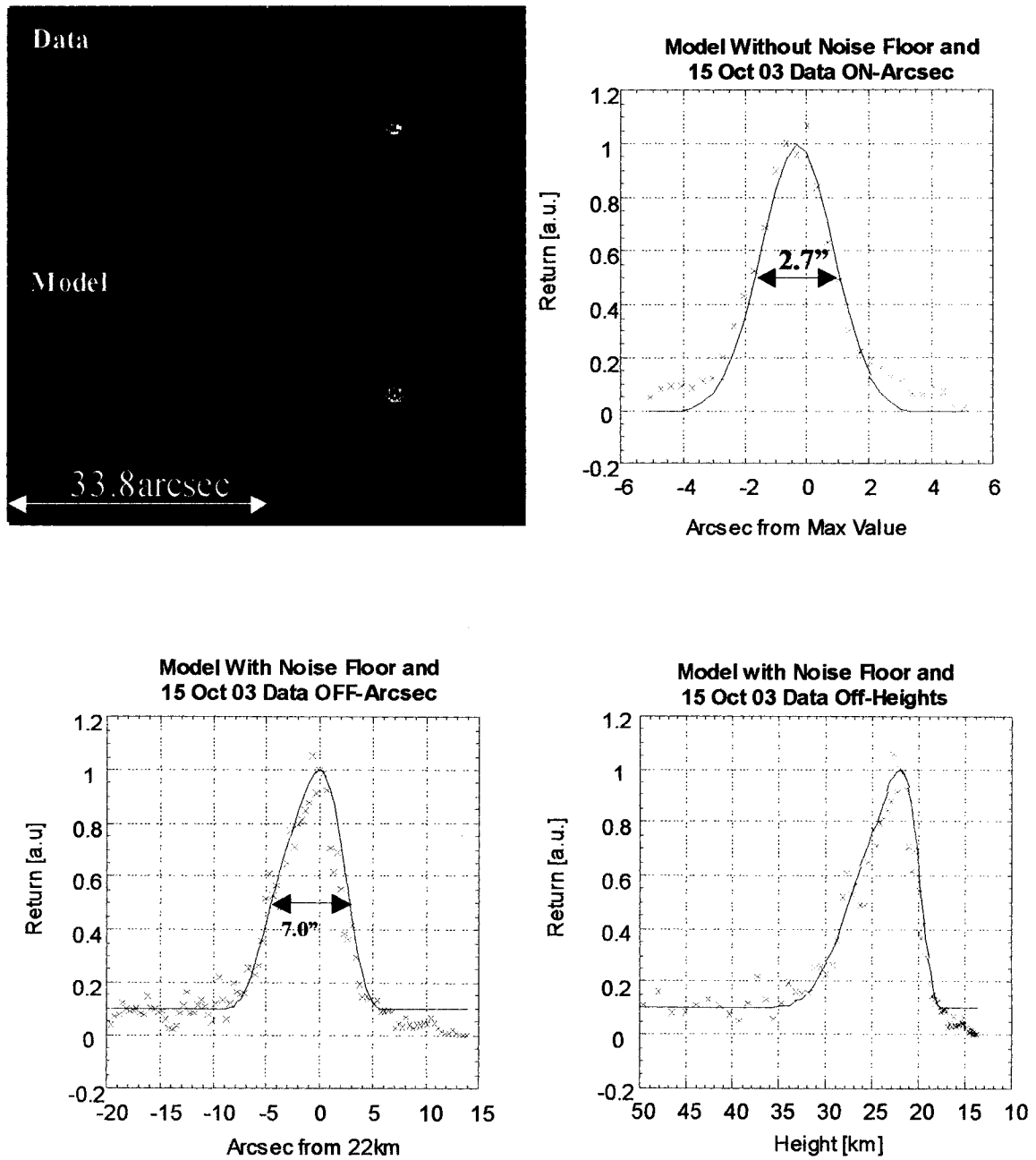


Figure 5.10 15 October 2003, 2:46am data. This above is analogous to figure 5.7.

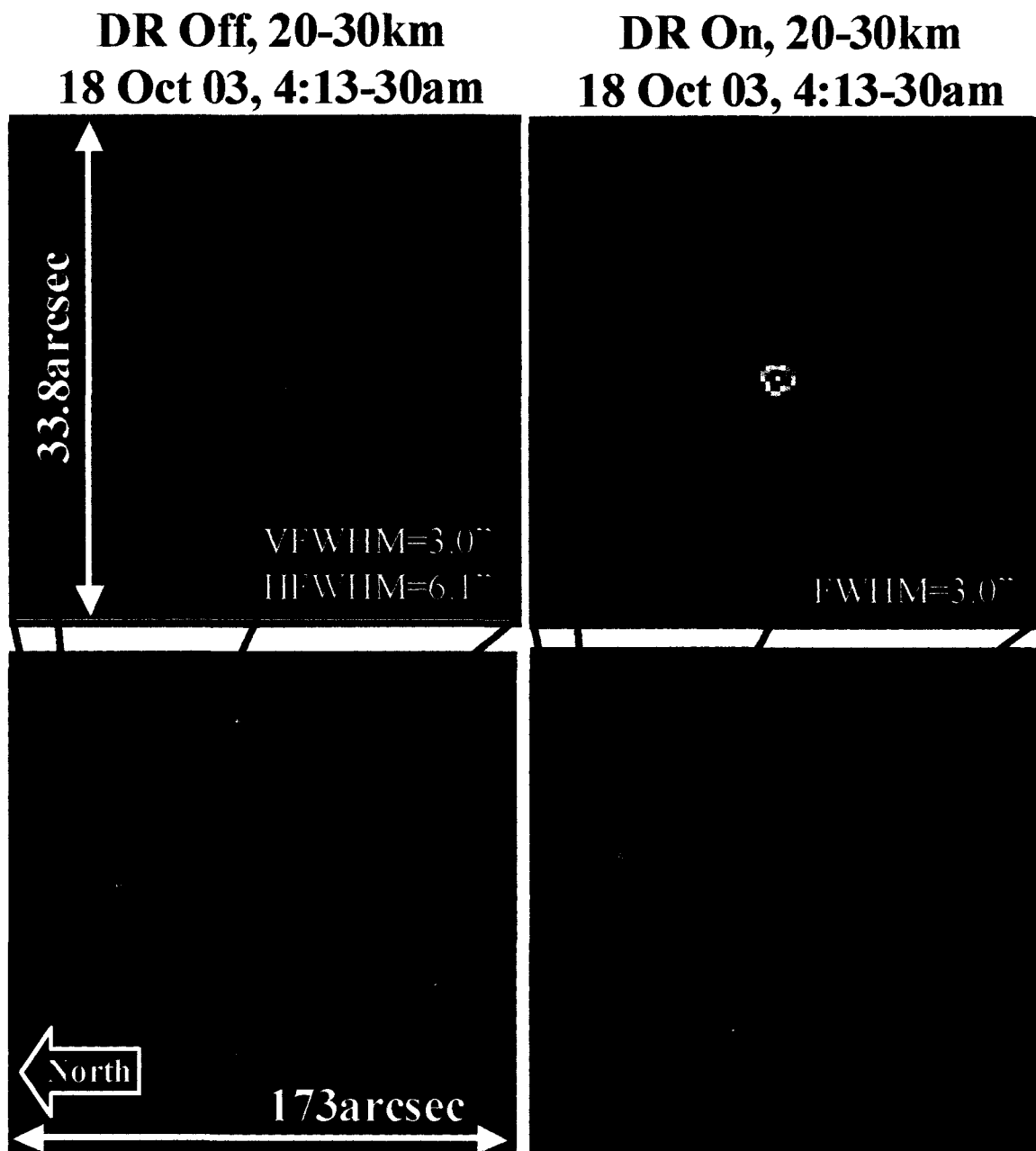


Figure 5.11 18 October 2003, 4:13-4:30am composite data. This above is analogous to figure 5.6.

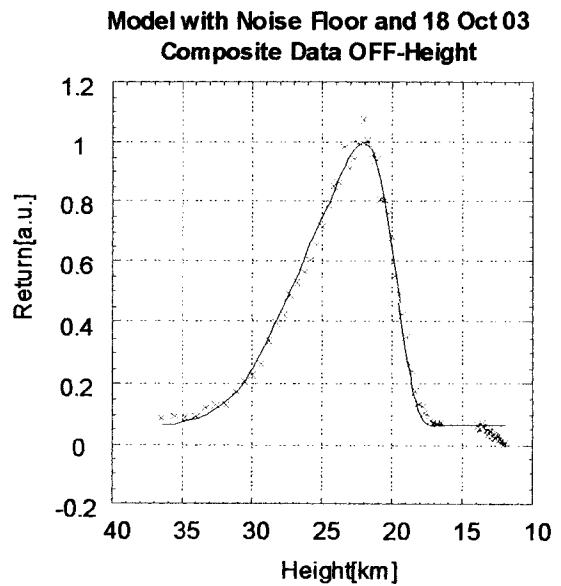
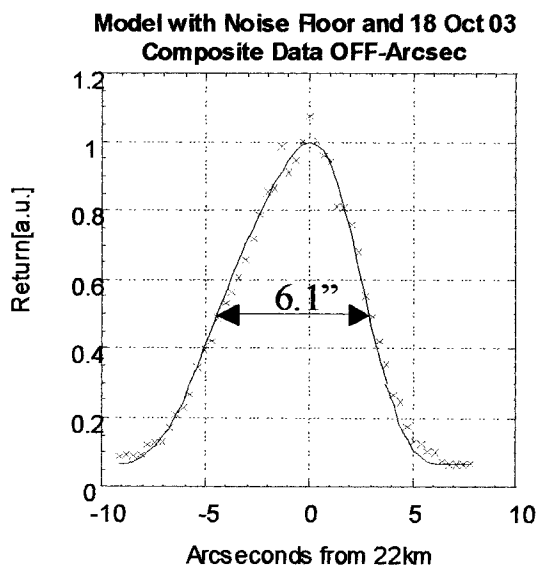
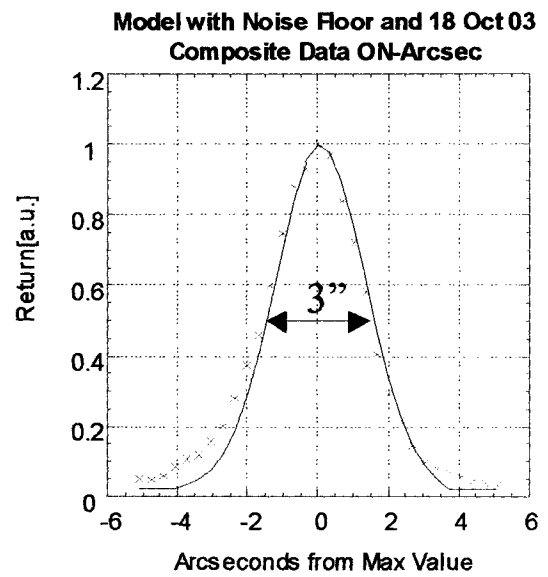
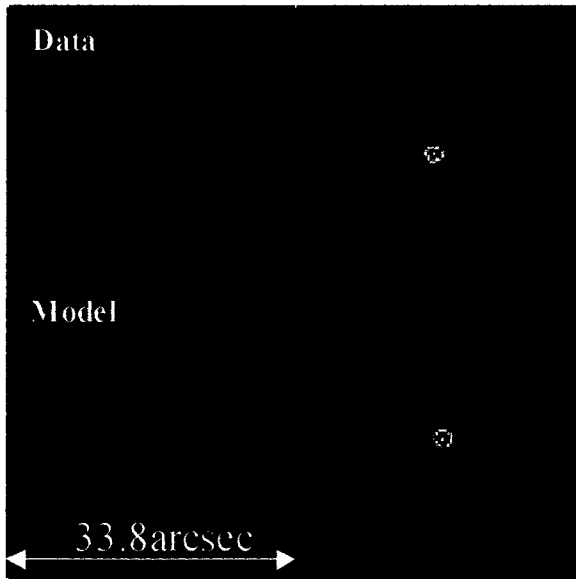


Figure 5.12 18 October 2003, 4:13-4:30am composite data. This above is analogous to figure 5.7.

5.3 ATMOSPHERIC MEASUREMENTS

The ultimate goal of the beacon constellation is to measure, across a large telescope aperture, wavefront aberrations contributed by different layers of the atmosphere. This is not possible with the present experiments, since only one sub-aperture is measured.

Nevertheless, the average motion and differential motion of the five beacons can be used to distinguish atmospheric turbulence arising near the ground from that at higher altitude.

5.3.1 TOTAL SEEING MEASURED BY BEACON IMAGE MOTION

Individual beacon images jitter because the up and down paths through the atmosphere are separated, by 2.5 m at the ground. While the geometry has not been modeled specifically, it is similar to that worked out by Martin [1987] and Tokovinin [2002] for differential motion of images of the same star formed by a telescope masked by two separated apertures. Such an arrangement, called a DIMM, is commonly used to measure Fried's length and atmospheric seeing. For a geometry with two apertures of diameter D , the FWHM of the atmospheric seeing, ε_0 , is related to the standard deviation, σ , of the radial image motion as,

$$\varepsilon_0 = 0.98 \left(\frac{D}{\lambda} \right)^{0.2} \left(\frac{\sigma^2}{K} \right)^{0.6} \quad (5.1)$$

where D is the subaperture diameter, λ is the wavelength and K is given by

$$K = 0.358(1 - 0.675b^{-1/3}) \quad (5.2)$$

where b is the ratio (subaperture separation)/(subaperture diameter).

For our set-up the apertures are of unequal size, 1.5 and ~ 0.15 m (when Gaussian beam size is taken into account). When the average of $D=50$ cm is adopted the factor $K \sim 0.22$ for the separation of 2.5m.

On the last night of data collection, 19 October 2003, the SBIG integration CCD was replaced with a CCD capable of recording at video rate of 60Hz (Astrovid Stellcam EX). This was used to measure the motion the of the five dynamically refocused beacons (20-30km) constellation. The analog video signal was captured and digitized through a National Instruments IMAQ board. We recorded 10second stretches of continuous data. Seven of these (made at 2:45, 2:49, 3:48, 3:50, 4:01, 4:02 and 4:03am) viewed and delivered good data. The centroid positions of all of the spots in each frame were measured.

An example of the total x (North-South) and y (East-West) motion of all the spots is shown in figure 5.13. The standard deviations of the total motions for all spots over all times is $\sigma_x=0.51\text{arcsec}$ and $\sigma_y=0.45\text{arcsec}$. These motions are combined in a scatter plot of radial motion (bottom figure 5.13) and yield a radial motion of rms amplitude $\sigma=0.68\text{arcsec}$.

Using the above results and equation (5.1) this yields a seeing FWHM of $\epsilon_o=1.8\text{arcsec}$. This is consistent with the measured FWHM of star images of 1.5arcsec and the seeing that we encountered over the entire run.

To measure the power spectrum of the image motion, the signal/noise ratio is improved by averaging the motion of the five spots for each time interval of data. An average power spectrum for the seven data sets was calculated separately for the x and y directions; this is shown in the log-log plots of figure 5.14. The measured slope of -1.2 is somewhat shallower than projected value of -1.67 for pure Kolmogorov turbulence.

5.3.2 DIFFERENTIAL MOTION

Because the five beacons are coincident as they leave the projector, and as they arrive back at the receiving telescope, turbulence near the telescope cannot cause differential motion. The differential motion was determined by subtracting the actual motion of each

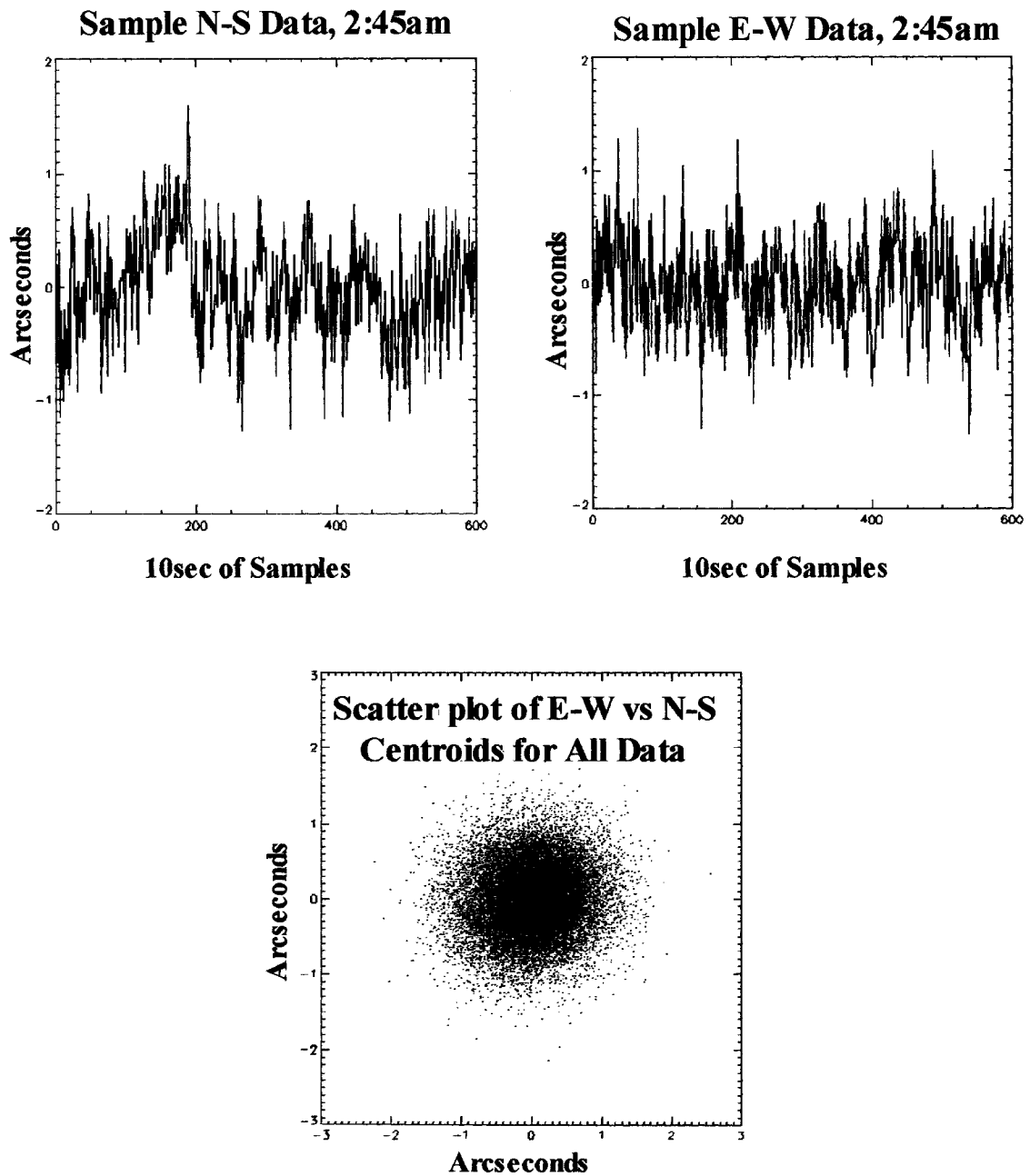


Figure 5.13 The top two graphs are an example of the raw North-South and East-West centroid data. The lower graph is a scatter plot of all of the East-West centroid data vs. the North-South data.

spot per time interval from the average motion of all five spots for that time interval. The signal/noise ratio is low, with a strong component of photon noise and ion events in the image tube. Since this noise is expected to be white, while real motion will be stronger at low frequencies, we can try to distinguish a real signal by taking the power spectrum of each spot's differential motion. The average power spectrum for the differential motion in the x and y directions is shown in (figure 5.2). Further exploration of this effect needs to be conducted to draw any significant conclusion regarding the differential motion especially in regard to warnings made by Martin [1987]. However, these examples show that atmospheric data can be measured with multiple laser beacons. Furthermore, the method of examining the common and differential motion will allow for height discrimination of atmospheric turbulence.

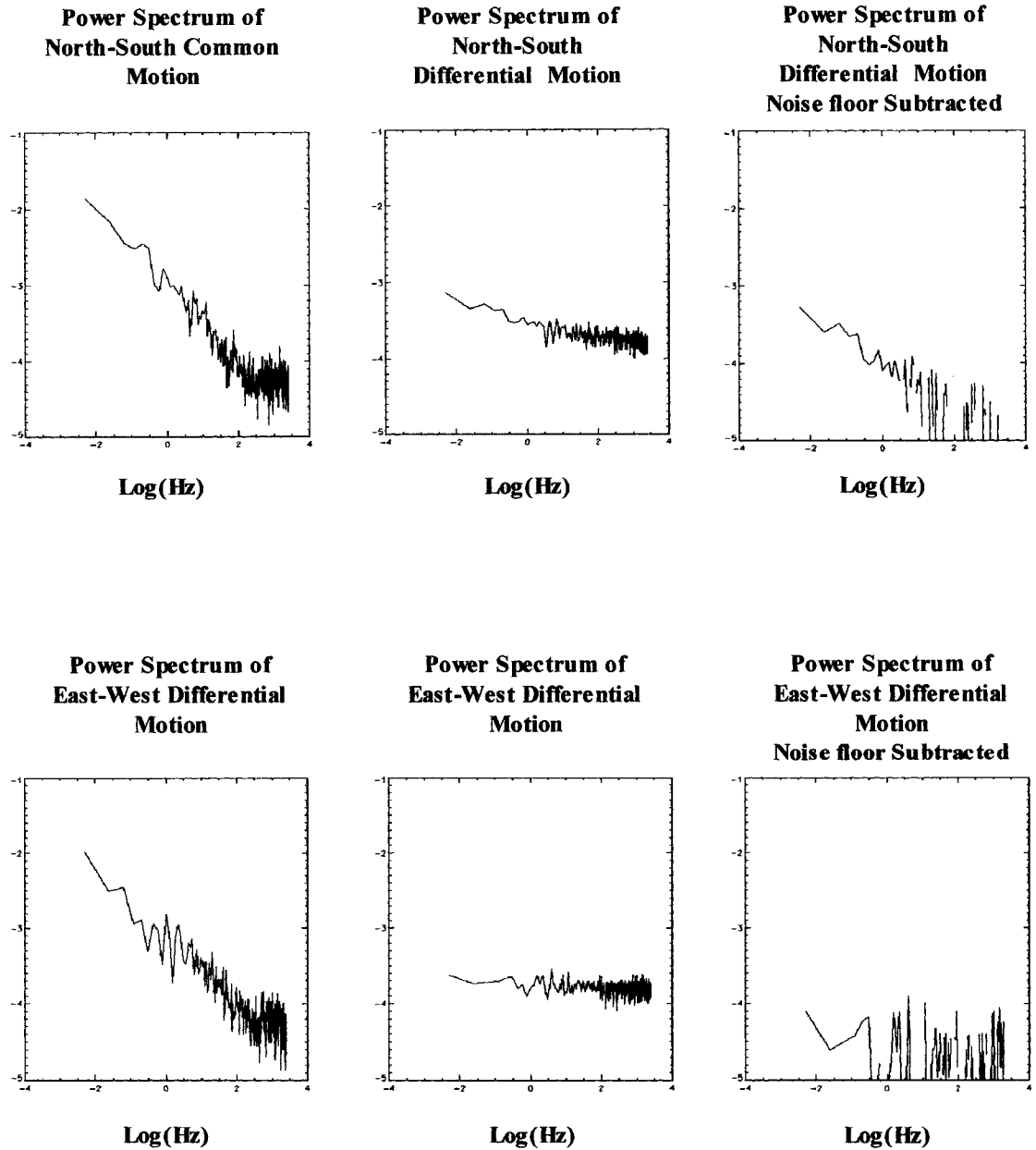


Figure 5.14 Log-log plots of the North-South (top row) and East-West (bottom row) power spectra. The first column shows the common motion, the second and third the differential.

5.4 SUMMARY

My goal for this dissertation was to understand and prove Roger Angel's idea of dynamic refocus. The results of that effort have been shown in this chapter. However, to bring this dissertation to a more complete conclusion it is instructive to recall the current state of AO LGS's presented in chapter 1. The next few paragraphs will review some of the difficulties associated with LGS's that were presented and how the work in this dissertation is an attempt to solve those problems

Laser

Currently sodium laser hold favor with a lot of the AO community and for good reason. A viable sodium beacon would allow for all the advantages of LGS's while producing the artificial guide star high in the atmosphere minimizing the cone effect. The current problem with such a laser is that they are expensive and difficult. One may only look to the scarcity of operational sodium AO efforts to come to that conclusion.

The disfavor of Rayleigh beacons has been that they have previously been explored low in the atmosphere near or in the turbulent layers [Fugate et al., 1994]. The low altitude was necessary because of poor photon return. DR solves that problem by allowing for photon return over a much larger range-gate. The higher photon rate allows one to use the Rayleigh beacon higher in the atmosphere. This dissertation has shown visual return from above 30km (5.3d).

Laser Quality and Beam Projector

As the AO community was looking for viable sodium beacons, commercial industry has developed high power, high quality and relatively cheap off-the-shelf laser systems. The implication of such lasers is that a modest amount of laser power may be put on the sky for few dollars. The lasers being of diffraction-limited quality allow for the use of an auxiliary beam projector, eliminating the problems of full aperture sharing. Again, this dissertation demonstrated the use of an auxiliary beam projector with a commercially available laser.

Dynamic Refocus

The major benefit of dynamic refocus is the collection of more photons by increasing the range-gate term in the Lidar equation. DR allows this while maintaining a beacon image that is limited only by atmospheric seeing. These two attributes keep the wavefront error associated with a SHWFS minimal, equations (1.25a&b). The ability to do this with an auxiliary beam projector and multiple low cost, high quality lasers allows for benefits given in the next two paragraphs.

Cone Effect

The MMT DR system was designed and tested in this dissertation for multiple beacons. Such an arrangement allows for tomographic reconstruction of the atmosphere that not only mitigates the cone effect but also allows for MCAO.

MCAO

While single sodium beacons continue to develop, dynamically refocused Rayleigh beacons are a first step toward MCAO on the MMT. In looking forward to MCAO on future 30m telescopes where image elongation in the sodium layer becomes problematic, the MMT DR Rayleigh beacon geometry scales almost exactly. This allows the lessons learned on the MMT to be applied to the sodium beacons on 30m telescopes.

Future Work

The next step, already in preparation, is to accomplish DR on the MMT and recover atmospheric phase information. The continued success of the technology will hopefully lead to the first LGS MCAO system in short time.

REFERENCES

- Angel, J.R.P., (2000). Dynamic refocus for Rayleigh beacons. *Science with the LBT, Proceedings of a workshop held at Ringberg Castle, Bavaria*, 21-25.
- Bolanti, S., Di Lazzaro, P. and Murra, D. (1997). How many times is a laser beam diffraction limited? *Optics Communications*, **134**, 503-513.
- Clark, P., Bissonauth, N., O'Byrne, J., Dunlop, C.N., Gregory, T., Morris, T.J., Myers, R.M., Saunter, C.D. and Wilson, R.W., (2003). Rayleigh guide star AO demonstrator for the 4.2m William Herschel Telescope. *Proc. of SPIE*, **4839**, 516-523.
- Fowles, G.R. and Cassiday, G.L. (1997). *Analytical Mechanics*. HBJ College and School Division.
- Fried, D.L. (1965). Statistics of a geometrical representation of wave-front distortion. *J. Opt. Soc. Am.*, **55**, 1427-1435.
- Fried, D.L. (1966). Optical resolution through a randomly inhomogeneous medium for very long and very short exposures. *J. Opt. Soc. Am.*, **56**, 1372-1379.
- Fried, D.L. (1982). Anisoplanatism in adaptive optics. *J. Opt. Soc. Am.*, **72**, 52-61.
- Fugate, R.Q., Ellerbroek, C.H., Higgins, C.H., Jelonek, M.P., Lange, W.J., Slavin, A.C., Wild, W.J., Winker, D.M., Wynia, J.M., Spinhirne, J.M., Boeke, B.R., Ruane, R.E., Moroney, J.F., Olikier, M.D., Swindle, D.W., Clies, R.A. (1994). Two generations of laser guide-star adaptive-optics experiments at the Starfire Optical Range. *J. Opt. Soc. Am. A.*, **11**, 310-324.

- Georges III, J.A., Mallik, P., Stalcup, T., Angel, J.R.P. and Sarlot, R. (2002). Design and testing of a dynamic refocus system for Rayleigh laser beacons. *Proc. SPIE*, **4839**, 473-483.
- Georges III, J.A., Stalcup, T., Angel, J.R.P. and Mallik, P. (2003). Field tests of dynamic refocus of Rayleigh laser beacons. *Proc. SPIE*, **5169**, In press.
- Gardner, C.S., Voelz, D.G., Sechrist Jr., C.F. and Segal, A.C. (1986). Lidar studies of nighttime sodium layer over Urbana, Illinois: 1. Seasonal and nocturnal variations. *J. Geophys. Res.*, **91**, 13659-13673.
- Gardner, C.S., Welsh, B.M. and Thompson, L.A. (1990). Design and performance analysis of adaptive optical telescopes using laser guide stars. *Proc. of the IEEE*, **78**, 1721-1743.
- Happer, W., MacDonald, G.J., Max, C.E., Dyson, F.J., (1994). Atmospheric compensation by resonant optical backscattering from the sodium layer in the upper atmosphere. *J. Opt. Soc. Am. A*, **11**, 263-276.
- Hardy, J.W. (1998). *Adaptive optics for astronomical telescopes*. New York : Oxford University Press.
- Hayano, Y., Takami, H., Takato, N., Kanzawa, T., Kamata, Y., Nakashima, K., Iye, M. and Oya, S. (2000). Preliminary experiments of prototype laser guide star system for Subaru telescope. *Proc. SPIE*, **4007**, 149-154.
- Hippler, S., Kasper, M., Feldt, M., Weiß, R., Looze, D.P., Montoya, L., Aceituno, A., Ott, T. and Davies, R., (2000). ALFA: Three years of experience in adaptive optics with a laser guide star. *Proc SPIE*, **4007**, 41-49.
- Humphreys, R.A., Primmerman, C.A., Bradley, L.C. and Herrmann, J., (1991)

Atmospheric-turbulence measurements using a synthetic beacon in the mesospheric sodium layer. *Optics Letters*, **16**, 1367-1369

Hynes, R. (2003). *Magnitude to flux calculator*. Retrieved December 12, 2003, from the Astronomy group at the University of Southampton Web site:
<http://www.astro.soton.ac.uk/~rih/applets/MagCalc.html>

Keck observatory reaches major milestone on road to expand adaptive optics. (2003). W.M. Keck Observatory. Retrieved November 13, 2003, from
http://www2.keck.hawaii.edu/news/LGS_AO.html

Lloyd-Hart, M., Angel, J.R.P., Jacobsen, B., Wittman, D., Dekany, R., McCarthy, D., Kibblewhite, E., Wild, W., Carter, B. and Beletic, J., (1995) Adaptive optics experiments using sodium laser guide stars. *The Astroph. Jour.*, **439**, 455-473.

Lloyd-Hart, M., Georges III, J.A., Angel, J.R.P., Brusa, G., Young, P. (2001). Dynamically refocused Rayleigh laser beacons for atmospheric tomography. *Proc. of SPIE*, **4494**, 259-270.

Lloyd-Hart, M. and Milton, N.M., (2002). Multi-conjugate adaptive optics for a new generation of giant telescopes. *Proc. of SPIE*, **4840**, 18-26.

Mallik, P (2004). Photon return as a function of altitude from a Rayleigh beacon.
In preparation

Martin, H.M. (1987). Image motion as a measure of seeing quality. *Pub. of the Ast. Soc. of the Pac.*, **99**, 1360-1370.

Max, C.E., Olivier, S.S., Friedman, H.W., An, J. Avicola, K., Beeman, B.V., Bissinger, H.D., Brase, J.M., Erbert, G.V., Gavel, D.T., Kanz, K., Liu, M.C., Macintosh, B., Neeb, K.P., Patience, J. and Waltjen, K.E., (1997). Image improvement from a

sodium-layer guide star adaptive optics system. *Science*, **277**, 1649-1652.

Miller, J.L. and Friedman, E. (1996). *Photonics rules of thumb*. New York: McGraw-Hill

Noll, R.J., (1976). Zernike polynomials and atmospheric turbulence. *J. Opt. Soc. Am.*, **66**, 207-211.

Rabien, S., Danies, R., Ott, T. and Butler, D., (2000). ALFA laser guide star: Present status and future developments. *Proc. SPIE*, **4007**, 50-56

Roddier, F. (1999). Imaging through the atmosphere & Theoretical aspects.
In F. Roddier (Ed.), *Adaptive optics in Astronomy* (pp.9-22 & 25-56). Cambridge, United Kingdom: Cambridge University Press.

Shack, R. (2001). [Optical Sciences 518, Introduction to Aberrations]. Unpublished class notes.

Schubert, G., Walterscheid, R.L. (2000) Earth. In A.N. Cox (Ed.), *Allen's astrophysical quantities, 4th edition* (pp. 239-292). New York: AIP Press.

Sandler, D.G. (1999). Overview of adaptive optics with laser beacons & The design of laser beacon AO systems. In F. Roddier (Ed.), *Adaptive optics in Astronomy* (pp.255-270 & 271-330). Cambridge, United Kingdom: Cambridge University Press.

Sandler, D.G., Stahl, S., Angel, J.R.P., Lloyd-Hart, M., McCarthy, D. (1994), Adaptive optics for diffraction-limited imaging with 8-m telescopes. *J. Opt. Soc. Am. A.*, **11**, 925-945.

Shi, F. (2001), Sodium laser guide star experiment with a sum-frequency laser for adaptive optics. *Pub. of the Ast. Soc. of the Pac.*, **113**, 366-378.

- Siegman, A. E., (1986). *Lasers*. Mill Valley, California: University Science Books
- Tatarski, V.I., (1961). *Wave propagation in a turbulent medium*. New York: McGraw Hill.
- Tokovinin, A. (2002). From Differential image motion to seeing. *Pub. of the Ast. Soc. of the Pac.*, **114**, 1156-1166.
- Thompson, L.A. and Gardner, C.S. (1987). Experiments on Mauna Kea observatory for adaptive imaging in astronomy. *Nature*, **328**, 229-231.
- Thompson, L.A., Castle, R.M., (1992). Experimental demonstration of a Rayleigh-scattered laser guide star at 351nm. *Optics Letters*, **17**, 1485-1487.
- Thompson, L.A., Teare, S.W., (2002). Rayleigh laser guide star systems: Application to the University of Illinois seeing improvement system. *Pub. of the Ast. Soc. of the Pac.*, **114**, 1029-1042.
- Tyler, G.S., Fried, D.L. (1982). Image-position error associated with a quadrant detector. *J. Opt. Soc. Am.*, **72**, 805-808.